MODELLING MICROSTRUCTURE EVOLUTION IN MATERIALS SCIENCE

PHASE-FIELD-CRYSTAL MODELS

FOR MICROSTRUCTURAL EVOLUTION AND PHASE SELECTION

IN MATERIALS SCIENCE

By

NANA OFORI-OPOKU

B.Eng Materials Science and Engineering, McMaster University
M.A.Sc Materials Science and Engineering, McMaster University

A Thesis
Submitted to the School of Graduate Studies
in Partial Fulfilment of the Requirements
for the Degree
Doctor of Philosophy

McMaster University

DOCTOR OF PHILOSOPHY (2013)　　　　McMaster University
(Material Science and Engineering)　　　Hamilton, Ontario

TITLE:　　　　　　　　　　　　　　　Phase-Field-Crystal Models For
　　　　　　　　　　　　　　　　　　Microstructural Evolution and Phase Selection
　　　　　　　　　　　　　　　　　　in Materials Science

AUTHOR:　　　　　　　　　　　　　Nana Ofori-Opoku,
　　　　　　　　　　　　　　　　　　B.Eng. (McMaster University),
　　　　　　　　　　　　　　　　　　M.A.Sc. (McMaster University)

SUPERVISOR:　　　　　　　　　　　Nikolas Provatas

NUMBER OF PAGES:　　　　　　　　xiii,110

i

ABSTRACT

Continuum atomistic and mesoscopic models are developed and utilized in the context of studying microstructural evolution and phase selection in materials systems. Numerous phenomena are examined, ranging from defect-solute interaction in solid state systems to microstructural evolution under external driving conditions. Emphasis is placed on the derivation and development of models capable of self consistently describing the intricate mechanisms at work in the systems undergoing these phenomena.

Namely, grain growth dynamics are studied in nanocrystalline systems under external driving conditions using a newly developed phase-field-crystal model, which couples an additional free energy source term to the standard phase-field-crystal model. Such external driving can be attributed to incident energetic particles. The nanocrystalline system is found to be susceptible to enhanced grain growth as a function of the intensity/flux associated with the external driving and the energy of driving. Static kinetic phase diagram calculations also seem to confirm that systems under external driving conditions can be forced into long metastable states.

Early stage solute clustering and precipitation in Al alloys is also examined with a variant of the phase-field-crystal method, so-called structural phase-field-crystal models for multi-component alloys developed as part of this thesis. We find that clustering is aided by quenched-in defects (dislocations), whereby the nucleation barrier is reduced and at times eliminated, a mechanism proposed by Cahn for a single dislocation for spinodal systems. In a three-component system, we predict a multi-step mechanism for clustering, where the nature and amount of the third species plays an important role in relieving stresses caused by the quenched-in dislocations before clustering, i.e., segregation as predicted by the equilibrium phase diagram, can occur.

Finally, we present a new coarse-graining procedure for generating complex amplitude models, i.e., complex order-parameter phase-field models, derived from phase-field-crystal models. They retain many salient atomistic features and behaviours of the original phase-field-crystal model, however is now capable of describing mesoscopic length scales like the phase-field model. We demonstrate the scheme by generating an amplitude model of the two-dimensional structural phase-field-crystal model, which allows multiple crystal structures to be stable in equilibrium, a crucial aspect of proper multi-scale modelling of materials systems. The dynamics are demonstrated by examining solidification and coarsening, peritectic growth, along with grain growth and the emergence of secondary phases.

ACKNOWLEDGEMENTS

Contents

List of Figures

List of Symbols

α_{obs} Interaction strength between multiple order parameters

ΔF_{exc} Excess free energy

ΔF_{ext} External potential energy

ΔF_{id} Ideal free energy

$\epsilon(\phi)$ Phase-field interpolated internal energy function

η, χ Ideal energy coefficients for XPFC models

$\mathcal{F}$ Free energy functional

Γ Frequency of forced atomic exchanges due to external driving

γ Reduced forcing frequency

λ Phase-field constant proportional to the inverse of the nucleation barrier

$\mathbf{J}$ Mass flux

$\mathbf{n}$ Normal vector to the interface

$\mathbf{q}_j$ Set of reciprocal lattice vectors

μ Chemical potential

ϕ Phase-field order-parameter

ψ Dimensionless concentration

ρ Unscaled atomic number density

ρ^{ℓ} Reference liquid density

ρ_i^{ℓ} Reference liquid density for component i

ρ_i Unscaled atomic number density for component i

$\tau(\mathbf{n})$ Anisotropic atomic attachment time, scales with the inverse of the atomic mobility

τ_{ϕ} Isotropic multi-order parameter time constant

τ_o Isotropic atomic attachment time, scales with the inverse of the mobility

φ_{eq} Equilibrium amplitude

$a(\mathbf{n})$ Interfacial width anisotropic function

a_1	Constant from matched asymptotic analysis, 0.8839
a_2	Constant from matched asymptotic analysis, 0.6267
A_j	Fourier coefficients, i.e., complex amplitudes, for first mode
a_t	Phase-field anti-trapping coefficient
$b(\mathbf{n})$	Atomic attachment time anisotropic function
B^ℓ	PFC dimensionless liquid isothermal compressibility
B^x	PFC dimensionless solid isothermal compressibility
c	Concentration field
$c.c.$	Denotes the complex conjugate
C_2	Direct two-point correlation function
C_2^{ij}	General direct two-point correlation function
c_l^o	Equilibrium liquidus composition at a reference temperature T_o
c_p	Specific heat capacity at constant pressure
D	Thermal diffusion coefficient
E	Effective energy functional
$f(\phi)$	Phase-field double well potential energy
f^A	Gibbs free energy of component A at T_m
f_c	Phase-field chemical free energy density
$g(\phi)$	Phase-field interpolation function
k	Partition coefficient
k_B	Boltzmann's constant
L	Latent heat of fusion
M	Mobility coefficient
M_i	Mobility coefficient for field i
n	Dimensionless atomic number density
n_o	Dimensionless average density
q	Wavenumber describing periodicity or wavelength of a particular structure
$q(\phi)$	Phase-field diffusion interpolation function
q_{eq}	Equilibrium wavenumber for structure
$s(\phi)$	Phase-field interpolated entropy function
T	Local temperature

T_m Melting temperature of a pure material

U Phase-field dimensionless temperature field

u Dimensionless relative chemical potential

v_o Molar volume

W Phase-field diffuse interface thickness

$w_{\mathcal{R}}$ Normalized weight distribution function for atomic exchanges

W_ϕ Isotropic multi-order parameter interfacial width

W_o Isotropic diffuse interfacial width

$\mathcal{R}$ Average distribution distance of atomic exchanges

List of Contributions

1. Harith Humadi, Nana Ofori-Opoku, Nikolas Provatas and Jeffrey J.Hoyt. Multi-scale Modeling of Modern Solidification Processes. *In Press JOM*, 2013.

2. Vahid Fallah, Andreas Korinek, Nana Ofori-Opoku, Nikolas Provatas, and Shahrzad Esmaeili. Atomistic investigation of clustering phenomenon in the Al-Cu system: three-dimensional Phase Field Crystal simulation and HRTEM-HRSTEM characterization. *Accepted Acta materialia* , 2013.

3. Nana Ofori-Opoku, Jonathan Stolle, Zhi-Feng Huang, and Nikolas Provatas. Amplitude models for structural transformations derived from structural phase-field-crystal models. *Under Review Phys. Rev. B.*, 2013.

4. Nana Ofori-Opoku, Vahid Fallah, Michael Greenwood, Shahrzad Esmaeili, and Nikolas Provatas. A multi-component phase field crystal model for structural transformations in metal alloys. *Phys. Rev. B.*, 87:134105, 2013.

5. Vahid Fallah, Nana Ofori-Opoku, Jonathan Stolle, Nikolas Provatas, and Shahrzad Esmaeili. Simulation of early-stage clustering in ternary metal alloys using the phase field crystal method. *Acta materialia*, 61:3653-3666, 2013.

6. Nana Ofori-Opoku, Jeffrey J. Hoyt, and Nikolas Provatas. Phase-field-crystal model of phase and microstructural stability in driven nanocrystalline systems. *Phys. Rev. E*, 86:066706, 2012.

7. Vahid Fallah, Jonathan Stolle, Nana Ofori-Opoku, Shahrzad Esmaeili, and Nikolas Provatas. Phase-field crystal modeling of early stage clustering and precipitation in metal alloys. *Phy. Rev. B*, 86:134112, 2012.

8. Michael Greenwood, Nana Ofori-Opoku, Jörg Rottler, and Nikolas Provatas. Modeling structural transformations in binary alloys with phase field crystals. *Phys. Rev. B*, 84:064104, 2011.

Author's Contribution

I have made notable contributions to all the phases of the work described in this dissertation. Particularly, I have written the first drafts of publications/contributions 3 (amplitude models), 4 (multicomponent structural phase-field-crystal models), and 6 (phase-field crystal models in driven systems), and in conjunction with the first author, contributed in writing the first drafts of publications 1 (multi-scale modelling in solidification), 5 (clustering in ternary Al alloys) and 8 (structural phase-field-crystal models in binary alloys).

Specifically, I performed the majority of the work, through derivations, calculations and simulations and their interpretations, for the works in contributions 3 (amplitude models), 4(multicomponent structural phase-field-crystal models), and 6 (phase-field crystal models in driven systems). I split with the first author the majority of work for contribution 8 in the development of the model and its applications. For contributions 2, 5 and 7 (clustering in binary and ternary Al alloys), I provided intellectual guidance and an enabling tool, through the models I developed and refined for these applications, e.g. see contributions 4 (multi-component structural phase-field-crystal models) and 8 (structural phase-field-crystal models in binary alloys). Contribution 1 (multi-scale modelling in solidification) is an invited review article (JOM), where models developed in contributions 8(structural phase-field-crystal models in binary alloys) and 4 (multi-component structural phase-field-crystal models), and extensions of them are presented in the context of solidification across multiple scales.

Chapter 1

Introduction

One of the basic tenants of materials science/physics and engineering is that the properties exhibited by materials depend on the underlying microstructure and alloying elements. It is worth noting that, often the richness and diversity exhibited by these microstructures are a direct result of the metastable equilibrium state the system happens to find itself.

It is no surprise then, that the physical, chemical and mechanical properties of materials can be directly linked to non-equilibrium defects, established during the processing of these systems. For most large scale industrial practices, these processes can be separated into, but not limited to, two main stages: (1) casting and (2) downstream operations. At the heart of the casting stage is the solidification process which involves phenomena such as, nucleation, free growth and subsequent merger of multiple crystallites. The second stage involves operations, such as thermomechanical processing or heat treatment cycles, designed to achieve certain specifications. This may require rectifying issues with the initial as cast structure or induce certain phase transformations as to engineer the desired set of properties for the given material. These processes can include the precipitation of additional phases, dissolutions of some unwanted primary or metastable phases or the removal of chemical inhomogeneities.

To understand the properties of engineering alloys and how they are intimately connected to the pattern of their microstructure and the phase selection process, a fundamental understanding of the various microstructural processes and mechanisms involved is necessary. Traditionally, an understanding of these fundamental processes and mechanisms has been gained, largely, due to empirical methods. Partly, this is due to the fact that the underlying phenomena involved are difficult, if not impossible to observe, let alone quantify *in situ*. The reason for this difficulty can be understood when one considers the multiple length and time scales on which these processes and mechanisms occur, not to mention the complex interactions involved, such as defect-solute interactions. For instance, in the casting process, we have nucleation which operates on atomistic length and time scales, i.e., *nanoscopic*. While at the other spectrum, thermomechanical processing and thermal treatments operate mostly on diffusive length and time scales, i.e., *mesoscopic* to *macroscopic* scales. Moreover, to a large extent, some of the basic theoretical mechanisms underlying these processes are poorly understood.

Advances in the predictive modelling of microstructure has seen great advances over the decades, particularly due to techniques capable of describing interfacial evolution in the presence of heat and mass transport kinetics. These techniques range from the atomistic to the mesoscopic/macroscopic. At the forefront of these theoretical techniques are notably, *molecular dynamics* (MD) and the *phase-field* (PF) method, and more recently the *phase-field-crystal* (PFC) method.

The purpose of this dissertation is the further development of modelling techniques, and their applications, to the study of microstructure and phase selection on multiple length and time scales. The relevant scales explored with the developed models intrinsically range from nanoscopic to meso-

scopic, and with the aid of novel adaptive mesh algorithms, models operating on the latter scales can be extended closer to macroscopic scales. The theoretical approaches discussed and used in the development of techniques presented here are the phase-field method and phase-field-crystal method [2], and the complex amplitude formalism derived from phase-field-crystal models. With the latter approach, the notion of multi-scale modelling becomes apt, as one of the aims in this thesis is to drive towards a multi-scale modelling platform for microstructural evolution in materials.

1.1   Theoretical Approaches

The phase-field method, a phenomenological theory, has its origins in Ginzburg-Landau [3] and Cahn-Hilliard [4, 5] theories. At its core, the PF method couples a set of uniform order parameters to one or more diffusion fields (i.e., temperature or solute fields), where dynamics follow dissipative minimization of some postulated free energy functional with dependence on some effective parameters. The formalism has been successfully applied to the study of solidification. It has gone far beyond its initial origins, and is now capable –through the use of auxiliary fields– of describing a plethora of phenomena such as multiple crystal orientations [6, 7, 8], multiple components and phases [9, 10, 11], defect-solute interactions [12], elasticity [13, 14] and plasticity [15].

The phase-field-crystal methodology is an atomistic scale modelling formalism [16, 17, 18, 19, 20]. It operates on atomistic length scales and diffusive time scales. Unlike their traditional PF counterparts, PFC free energy functionals are minimized by periodic fields. This allows the self-consistent incorporation of elasto-plastic effects, multiple crystal orientations, grain boundaries and dislocations, all evolving over mesoscopic time scales. The methodology has also been shown to be derivable [18, 21] from the more microscopic and fundamental classical density functional theory (CDFT) [22, 23, 24].

Derived from coarse-graining PFC/CDFT functionals, complex amplitude models bear a striking resemblance to PF models. As such, PFC models can also be used to derive the appropriate forms of traditional PF models from a more fundamental theory, through coarse-graining procedures. These complex amplitude* models now operate on mesoscopic length and time scales, and remarkably retain many of the rich atomistic level phenomena of their more microscopic PFC/CDFT counterparts. This characteristic of the amplitude models make them prime candidates –when coupled with appropriate algorithms– as efficient modelling platforms for investigating microstructure evolution and phase selection across scales.

As alluded to earlier, our current understanding of some of the fundamental mechanisms at work in materials systems is incomplete. The proposed suite of models derived in this work can be exploited to gain a more fundamental understanding of the physical processes and mechanisms at work in microstructural evolution and the phase selection processes. In sequence of how the work is presented in this dissertation, the areas are the stability of nanocrystalline systems under external driving and solute clustering leading to precipitation. Another aim of this work is to understand the feasibility in developing more complex, yet simple, models from more microscopic theories and examine their validity and usefulness. At the least, the means by which we go about developing said models, may present an appropriate or more informed mapping of parameters required in the modelling of microstructure at the mesoscopic and macroscopic level.

1.2   Thesis Outline

Next we outline, briefly and generally, the topics that will be covered in the chapters to follow (Chapters 2-7).

---

*That is, complex-order parameters, going back to the original work on superconductivity of Ginzburg and Landau

Chapter 2: Phase-field Methods and Theory

The goal of this chapter is to introduce the reader to phase-field theory and methods, i.e., the PF and PFC method. Particularly, we discuss the phase-field method because it has been the benchmark and standard in the modelling of microstructure evolution. By no means is the introduction exhaustive, as there are several books and review articles in the literature. Our aim is to present the main features and important developments that have been made. Specifically, we focus on the developed *thin-interface* asymptotic analysis [25, 26, 27] approach in allowing for quantitative simulation of solidification processes.

For the PFC method, we introduce and review the standard energy functional of the method, which has its origins in the Swift-Hohenberg [28] equation, used to study convective instabilities. In the last decade, the method has seen tremendous changes and improvements. One of which is deriving its fundamental origins in classical density functional theory. Priority is given to the recent development of a variant of PFC models, the so-called structural PFC (XPFC) [19, 20], a model which allows several[†] crystal phases to coexist with each other and with a liquid phase.

Chapter 3: Microstructural and Phase Stability in Driven Nanocrystalline Systems

The phase-field method is a powerful technique. However, when the details of interfacial structure and elasticity become important in the phenomena being studied, a more microscopic theory is needed. Chapter 3 revisits the microscopic PFC model and its use in studying the evolution and stability of nanocrystalline materials, which are being developed as viable replacements in industries ranging from microelectronics to core components in nuclear reactors.

A phase-field-crystal model is developed to study the long time stability of these systems under forced external conditions, such as, for example, irradiation. Static calculations, through phase diagram calculations, and dynamic simulations suggest that nanocrystalline materials do not actually stay nanocrystalline as a function of the forcing conditions.

Much of the work presented in this chapter is published in *Physical Review E* [29].

Chapter 4: Structural Transformations in Multi-Component Alloys Using Phase-Field-Crystal Models

Engineering alloys rely heavily on multi-component alloying in order to achieve desired properties. Here we extend the XPFC paradigm to the general case of N-component alloy systems. The model is developed starting from CDFT, where each component has as input a correlation kernel like that in the original XPFC work. Interactions between different components are modelled by interpolating single-component correlation kernels as a function of the local composition. The model is derived, and is then simplified into a more tractable form, and finally its dynamic properties are presented.

The derivation presented here has been published as parts of manuscripts in *Physical Review B* [30] for binary alloys and [31] for N-component alloys.

Chapter 5: Specialization of the Multi-Component Model to Binary Systems and Application to Ageing in Binary Alloys

The structural phase-field-crystal method, for the first time, allowed the stabilization of several multiple crystal structures and more realistic phase diagrams (alloys) to be considered. This chapter considers the binary alloy limit of the multi-component model of the previous chapter. After stating the free energy functional of the binary model, we demonstrate and showcase some of the important features and behaviour of the model through calculation of several binary phase diagrams and some sample simulations.

Following the development of the model, it is then used to study solute clustering mechanisms in a model Al-Cu system. There has long been conjecture in the literature on the nature of the clustering mechanism leading to Guinier-Preston Zones and ultimately precipitation in these alloy

---

[†]In two-dimensions (2D) square and triangular lattices and in three-dimensions (3D) FCC, BCC, HCP and SC.

systems. Through simulations and calculation of system energetics, we conclude that clustering in these systems can be dislocation-aided, whereby energy barriers to solute clustering in the system are reduced and even removed entirely. A concept long discussed in the literature, but revealed kinetically for the first time through XPFC simulations.

Much of the work presented in this chapter is published in *Physical Review B* [30, 32].

Chapter 6: Specialization of the Multi-Component Model to Ternary Systems and Application to Ageing in Ternary Alloys

Next we simplify the multi-component model of Chapter 4 to three-component alloy systems. An additional component over the binary model, it offers a variety of complex interactions that can be studied. The free energy functional is presented, following which equilibrium phase diagrams are calculated. The model is then demonstrated kinetically via dendritic and eutectic solidification.

The simple three-component model is then used to study solute clustering in a model Al-Cu-Mg system. The addition of a third component to the system has wide ranging consequences on the system evolution and energetics. Our analysis indicates a multi-stage clustering mechanism due to the presence of an additional atomic species. A mechanism which cannot be captured with conventional approaches.

Much of the work presented in this chapter is published in *Physical Review B* [31] and *Acta Materialia* [33].

Chapter 7: Multi-Scale Modelling: Amplitude Expansions of Phase-Field-Crystal Models

Chapter 7 completes the research portion of the thesis by shifting focus from atomistic length scales to mesoscopic scales. The variants of PFC models, particularly the XPFC suite of models present a promising modelling formalism for studying atomistic scale effects, such as elasto-plasticity, defects, multiple crystal orientations, multiple phases, etc., on diffusive time scales. However, from a computational view point, it is limited to the nanocrystalline length scales, even with sophisticated computational algorithms.

This chapter attempts to address this length scale weakness by presenting a general Fourier space formalism for generating a set of complex amplitude (complex order-parameter) models, for pure materials and alloys, which when coupled to sophisticated algorithms (e.g. adaptive mesh refinement), can operate on atomistic length scales to macroscopic length scales.

A general recipe is provided for generating amplitude models from PFC and PFC-type models, here applied to the XPFC model for a pure material in 2D. The method can easily be extended for 3D structures and for N-component alloy systems. Sample simulations are then conducted to showcase the validity and applicability of the model.

Portions of the work presented in this chapter at the time of writing this thesis is under review in *Physical Review B* [31].

Finally, in Chapter 8, we end with some concluding remarks and a discussion on the future outlook of some of the work presented in this dissertation.

Chapter 2

Phase-field Methods and Theory

This chapter will give an overview of the two main theoretical approaches used throughout this thesis. First, the phase-field (PF) method is reviewed in the context of its application to solidification of pure materials and alloys. We highlight the quantitative nature of the method and its development [34, 25, 26, 35].

The second part of this chapter will review the origins of the phase-field-crystal (PFC) method. It will outline the basic concepts and elements of PFC models. We introduce the standard functional for pure systems, later extended for alloys, and discuss it in context from its derivation from classical density functional theory (CDFT). For a more exhaustive review than what is presented here, the reader is referred to the primary Refs. [17, 18, 2]. We end by introducing the structural PFC (XPFC) model of Greenwood *et al.* [19, 20], which introduces a self-consistent method of stabilizing multiple crystal structures in pure materials, which will be extended and applied in this thesis to multi-component alloys.

2.1 Phenomenology of Phase-Field

2.1.1 General Concepts

To review the general concepts of the PF method, we will be examining it in the context of the well documented case of solidification in pure materials and binary alloys. Generally, the methodology begins by construction, phenomenologically, of some free energy functional, $\mathcal{F}$. This free energy functional is expressed in terms of, considering solidification of a pure material, the temperature and polynomial terms of an order-parameter ϕ^*, where the scalar order-parameter, i.e., the phase-field, is a place holder for the two equilibrium phases. It takes on the values $\phi = 1$ and $\phi = -1$ in the solid and liquid, respectively. The order-parameter field then interpolates between these two equilibrium values across a diffuse thin interface of thickness, W, which defines the level set of points described by $-1 < \phi < 1$. For a pure material, such a functional can be written (in dimensionless units) as [34, 36],

$$\mathcal{F}[\phi, U] = \int d\mathbf{r} \left(\frac{1}{2} |W(\mathbf{n})\nabla\phi|^2 + f(\phi) + \lambda \, U(T) g(\phi) \right), \qquad (2.1)$$

where the gradient term, $|W(\mathbf{n})\nabla\phi|^2|$, controls the surface energy and is made anisotropic through the functional form $W(\mathbf{n}) = W_o a(\mathbf{n})$ [37, 38]. W_o is the isotropic interfacial width, $a(\mathbf{n})$ is the

---

*The expression of the free energy in polynomials of an order-parameter dates back to van Der Waals, made popular by the work of Ginzburg-Landau [3]. Particularly Landau in his mean field work on critical phenomena.

anisotropic function for the interface width and $\mathbf{n}$ is the normal vector to the interface. A typical form for the anisotropy function is

$$a(\mathbf{n}) = (1 - 3\epsilon_4)\left(1 + \frac{4\epsilon_4}{1 - 3\epsilon_4}\left(n_x + n_y + n_z\right)\right). \tag{2.2}$$

The function, $f(\phi)$, is the PF *double well* free energy which sets the equilibrium states of the solid and liquid, respectively. A convenient form which satisfies the equilibrium values for the solid and liquid values given above is $f(\phi) = -\frac{\phi^2}{2} + \frac{\phi^4}{4}$. λ formally is a constant that is proportional to the inverse of the nucleation barrier between solid and liquid. However, when the actual process of nucleation is ignored, for kinetic purposes, λ can be treated as a free convergence parameter. $U(T) = (T - T_m)/(L/c_p)$ is the dimensionless temperature, with T the temperature and T_m is the melting temperature, c_p is the specific heat capacity and L is the latent heat of fusion. Finally, $g(\phi)$ is a monotonously increasing interpolation function which satisfies $g(\pm1) = 1$ and $g'(\pm1) = 0$. An appropriate choice which satisfies these conditions has the form $g(\phi) = \frac{15}{8}(\frac{\phi^5}{5} + 2\frac{\phi^3}{3} - \phi)$. The term $\lambda U g(\phi)$ provides a driving force capable of tilting the double well energy to favour a particular equilibrium state. Clearly, the tilting behaviour is directly related to the temperature, T, of the system. In Fig. 2.1, we plot the behaviour of the energy density, i.e., $f(\phi) + \lambda U g(\phi)$, as a function of the order-parameter for several temperatures.
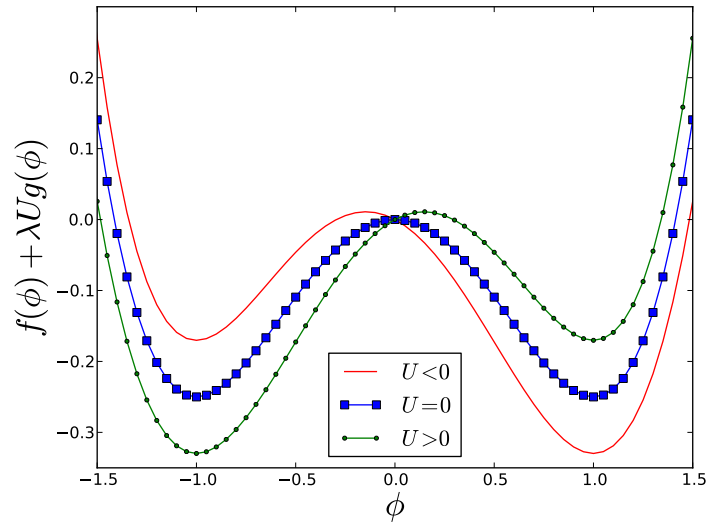
Figure 2.1: The energy density term, $f(\phi) + \lambda U g(\phi)$, from the free energy functional for the phase-field model of Eq. (2.1). Clearly evident is the tilting behaviour as a function of temperature. High temperatures favour a system were liquid has minimum energy, while low temperatures favour solid minimization.

The time evolution of the fields proceed by dissipative minimization of the free energy functional above. For the phase-field, ϕ, minimization leads to the time-dependent Allen-Cahn [39, 40, 41]/Ginzburg-Landau equation following nonconserved dynamics[†], also known as *Model A* dynamics in the Halperin and Hohenberg [42] classification scheme. The dynamic equation for ϕ is expressed as

---

[†]Non-conserved dynamics implies that the ϕ field is not a conserved quantity and so the dynamics (when fluctuations are included) will eventually evolve the system into its lowest free energy state.

$$\tau(\mathbf{n})\frac{\partial \phi}{\partial t} = -\frac{\delta \mathcal{F}}{\delta \phi}$$

$$= \nabla \cdot \left(W^2(\mathbf{n})\nabla^2\phi\right) + \nabla \cdot \left(W(\mathbf{n})|\nabla\phi|^2 \frac{\partial a(\mathbf{n})}{\partial(\nabla\phi)}\right)$$

$$+ \phi - \phi^3 - \lambda U(1-\phi^2)^2, \tag{2.3}$$

where $\tau(\mathbf{n}) = \tau_o b(\mathbf{n})$ is the anisotropic atomic attachment kinetic time, τ_o is the isotropic attach-ment time which scales with the inverse of the atomic mobility, and $b(\mathbf{n})$ is the atomic attachment anisotropic function. The first line of Eq. (2.3) introduces the concept of a variatonal/functional derivative[‡]. Equation (2.3) for ϕ is coupled to a modified heat equation for the dimensionless tem-perature field, U, following *Model B* dynamics[§] of the form,

$$\frac{\partial U}{\partial t} = \nabla \cdot \left(\bar{D}\nabla U\right) + \frac{1}{2}\frac{\partial \phi}{\partial t}, \tag{2.4}$$

where $\bar{D}$ is the dimensionless thermal diffusion coefficient. The second term in Eq. (2.4), is a source term representing the release of latent heat at the interface of a growing front. Combined, Eqs. (2.3) and (2.4) constitute *Model C* dynamics of the Halperin and Hohenberg classification, which couples a Model A equation with a Model B equation. Note that, as written Eq. (2.4) is postulated. However, if one were to use an entropy functional formalism, instead of a free energy formalism, Eq. (2.4) would also follow from variational of the entropy with temperature.

Next we use the general concepts just discussed, to illustrate how the phase-field model can be made quantitative, i.e., emulate the correct sharp interface behaviour in the limit of vanishing interface thickness, for pure materials and alloys. This limit is important as it is used to describe most experimental conditions in materials processing.

2.1.2   Quantitative Phase-Field Model Modelling

2.1.3   Pure Materials

The phase-field model can be made to recover the correct sharp interface kinetics with appropriate choice of parameters. To understand how this can be achieved, it is beneficial to explicitly recall the dimensionless rescaling of the Model C set of equations in the previous section. The dimensionless set of equations were attained by rescaling space, $\mathbf{r} \to \mathbf{r}/W_o$, and time, as $t \to t/\tau_o$. Without loss of generality, we let $\tau_o = W_o = 1$, while $\bar{D} \to D\tau_o/W_o^2$ in Eq. (2.4), where D is the dimensional thermal diffusivity.

Classically, this so-called *sharp interface limit* of phase-field models, was achieved by letting $W \to 0$ and $\lambda \to 0$, while employing a projection procedure to the set of reduced Model C equa-tions. This leads to the capillary length being defined as $d_o \propto W_o/\lambda$ and the kinetic coefficient (from the Gibbs-Thomson equation) defined as $\beta = \tau_o/(W_o\lambda)$ [43, 44]. For the general case of negligible interfacial kinetics, i.e., $\beta = 0$, which is the case for most conventional casting prac-tices, this would require that τ_o be excessively small. With the interface width being on the order of 10^{-9}m, this would prevent the large scale simulation of dendritic solidification processes over reasonable periods of time.

Karma and Rappel [34, 37, 36], in a seminal work, addressed this shortcoming of the classical mapping to the sharp interface set of kinetic equations. Performing a matched asymptotic analysis to second order, the so-called *thin interface limit*, their work showed that the following relationships,

---

[‡]Similar to a normal derivative, a variational derivative determines how a functional varies with the changes of its dependent function, in this case ϕ.

[§]Model B is generic dynamics associated with conservative fields, such as energy and mass.

Eqs. (2.5) and (2.6)[¶] guarantees the correct recovery of the sharp interface model, and still provides computational freedom for large scale simulations.

$$d_o = a_1 \frac{W_o}{\lambda}, \tag{2.5}$$

$$\beta = \frac{a_1 \tau_o}{W_o \lambda} \left(1 - a_2 \frac{W_o^2 \lambda}{D \tau_o} \right), \tag{2.6}$$

where $a_1 = 0.8839$ and $a_2 = 0.6267$ are constants from the asymptotic analysis that depend on the choice of double well potential and interpolation function in Eq. (2.1). Note that in these new set of sharp interface relationships, the kinetic coefficient (β), can be made identically zero without τ_o being made excessively small.

2.1.4 Dilute Binary Alloy

One can easily write down a free energy functional for alloy solidification as well. Where a mapping can also be developed to appropriately recover the right sharp interface kinetic equation. To describe a binary alloy, we can write a functional such as

$$\mathcal{F}[\phi, c] = \int d\mathbf{r} \left(\frac{1}{2} |W(\mathbf{n}) \nabla \phi|^2 + f(\phi) + f_c(\phi, T, c) \right), \tag{2.7}$$

where c is the concentration field. The new term, $f_c(\phi, T, c)$, is the chemical free energy density, whose form around the minima (in terms of c) of the equilibrium states can be deduced from thermodynamic databases. For isothermal solidification, we can readily write the corresponding Model C set of evolution equations for a system described by this functional. The phase-field follows Model A dynamics of the form,

$$\tau(\mathbf{n}) \frac{\partial \phi}{\partial t} = -\frac{\delta \mathcal{F}[\phi, c]}{\delta \phi}, \tag{2.8}$$

while the concentration follows

$$\frac{\partial c}{\partial t} = \nabla \cdot \left(M(\phi, c) \nabla \frac{\delta \mathcal{F}[\phi, c]}{\delta c} \right), \tag{2.9}$$

which is a conservation of mass equation, since it can be rewritten as

$$\frac{\partial c}{\partial t} + \nabla \cdot \mathbf{J} = 0, \tag{2.10}$$

where

$$\mathbf{J} = -M(\phi, c) \nabla \mu. \tag{2.11}$$

It is apparent then that $\mu \equiv \frac{\delta \mathcal{F}[\phi, c]}{\delta c}$, the chemical potential. $M(\phi, c)$ is the solute mobility and is proportional to the diffusion coefficient.

In order for practical simulations of any alloy phase-field model described by a functional of the form of Eq. (2.7), one needs to artificially "stretch" the interface. However, artificial stretching of the interface enhances effects –at all cooling rates– of a non-equilibrium nature, that scale like the width of the interface. Effects such as solute trapping. While these effects are all physical, they are expected only to be valid at rapid cooling rates. The stretching of the interface effectively forces the model to depart from the expected sharp interface model, even at low cooling rates. These non-equilibrium effects have been documented precisely as being; (a) chemical potential jump at the interface and a modification of the mass conservation at the interface, (b) stretching of the interface

---

[¶]Provided both the interface and attachment time kinetics have the same anisotropic form.

because of curvature differences on the solid and liquid sides of the interface respectively, when the interface is non-zero and (c) diffusion tangentially through the interface.

Karma and co-workers found a remedy –at least for dilute binary alloys– for all three spurious kinetic effects. The work of Karma [25], demonstrated all kinetic effects can be made to vanish simultaneously while still allowing one to exploit the benefits of a diffuse interface. Later, a more rigorous derivation and matched asymptotic analysis followed [26, 45]. For an ideal dilute system, the chemical free energy density used in these works is written as,

$$f_c(\phi, T, c) = f^A(T_m) - \Delta T s(\phi) + \frac{RT_m}{v_o} \left(c \ln c - c\right) + \epsilon(\phi)c \tag{2.12}$$

where $f^A(T_m)$ is the free energy of component A at the melting temperature, $s(\phi)$ is the phase-field interpolated entropy, R is the gas constant, v_o is the molar volume of the solid and $\epsilon(\phi)$ is the phase-field interpolated internal energy. To correct for the spurious effects, the method forgoes the variational formalism that lead to Eqs. (2.8) and (2.9). Rather, the following changes were made: (i) change of the interpolation function for the chemical potential from the original one inherited from the free energy functional, (ii) introduction of a phenomenological flux, so-called *anti-trapping flux*, term to the concentration dynamics and (iii) choose the specific interpolation function governing diffusion through the interface. Together, these corrections provided the necessary degrees of freedom to allow complete elimination of the spurious effects. The evolution equations for this model, then read,

$$\tau(\mathbf{n}) \frac{\partial \phi}{\partial t} = \nabla \cdot \left(W^2(\mathbf{n})\nabla^2\phi\right) + \nabla \cdot \left(W(\mathbf{n})|\nabla\phi|^2 \frac{\partial a(\mathbf{n})}{\partial(\nabla\phi)}\right)$$
$$+ \phi - \phi^3 - \frac{\lambda}{1-k} \left(e^u - 1\right)(1-\phi^2)^2 \tag{2.13}$$

$$\frac{\partial c}{\partial t} = \nabla \cdot \left(D_L c q(\phi)\nabla u - a_t W_o c_l^o (1-k)e^u \frac{\partial \phi}{\partial t} \frac{\nabla\phi}{|\nabla\phi|}\right). \tag{2.14}$$

$u = \ln\left(\frac{2c}{c_l^o[1+k-(1-k)\phi]}\right)$ is the dimensionless relative chemical potential, k is the partitioning coefficient for the alloy and c_l^o is the equilibrium liquidus composition at a reference temperature. $q(\phi) = \frac{1-\phi}{1+k-(1-k)\phi}$ is the diffusion interpolation function, while a_t is the anti-trapping coefficient, which is a constant dependent on the choice of $q(\phi)$. It turns out that a matched asymptotic boundary layer analysis on Eqs. (2.13) and (2.14) yields a sharp interface limit that continues to enjoy (by construction) the parametric relations in Eqs. (2.5) and (2.6) for matching model parameters to the capillary length and kinetic coefficient. Here, $D \to D_L$, the solute liquid diffusion coefficient.

The phase-field paradigm has been extended to include the effect of multiple alloy components and phases [46, 47, 48, 49]. To date most such models are plagued by their inability to perform efficient large scale simulations on experimentally relevant length scales and process parameters and lacking a thin-interface analysis. The work of Kim [50] and Nestler *et al.* [11] are exceptions, which in recent approaches, corrections such as an addition of an anti-trapping flux term has been included. However, to our knowledge, the first of these works is based only on single-phase (or single crystal) solidification, while the second work has not demonstrated the operation of the anti-trapping quantitatively.

The dilute model of Karma and co-workers has been used in a variety of works. Greenwood *et al.* [51] utilized it in the study of spacing selection in directional dendritic growth in 2D, then Provatas *et al.* [52] extended this study in 3D and Folch and Plapp [53] specialized it to three phase systems to examine eutectic and peritectic systems. Later Tong *et al.* [27] extended the work to address non-dilute, non-ideal binary alloys, i.e., nonlinear phase boundaries. In their work, Tong *et al.* proposed a paradigm whereby one can approximate the Gibbs free energy of a general alloy, using as a fitting function for the free energy the mathematical form of the ideal dilute alloy, modified

however with effective temperature parameters. That is to say that, in their work, the following modifications were made; $\tau(\mathbf{n}) \rightarrow \tau(T, \mathbf{n})$, $W(\mathbf{n}) \rightarrow W(T, \mathbf{n})$ $k \rightarrow k(T)$ and $D \rightarrow D(T)$.

Recently, Ofori-Opoku and Provatas [35], generalizing the work of Karma and co-workers and Tong *et al.*, presented a novel approach to study single phase polycrystalline solidification in ideal and non-ideal alloys. Their work introduces a multi-order parameter state vector, $\vec{\phi}$, to represent N crystalline orientations. A method, which can easily be extended to include multiple phases and multiple components. By construction of the model, during the free growth process, each order-parameter (which represents a single phase crystal) is demonstrated to follow exactly the formulation of Karma and co-workers. On merger of multiple crystals, where interface motion is negligible, the model reduces to the regular multi-order phase-field models which have been shown to recover the correct Allen-Cahn [39, 40, 41] behaviour for such phenomena as grain growth in the solid state.

The multi-order phase-field model of Ofori-Opoku and Provatas has the following evolution equations, shown here for an isotropic, dilute system

$$\tau_\phi \frac{\partial \phi_i}{\partial t} = W_\phi^2 \nabla^2 \phi_i + \phi_i - \phi_i^3 - \alpha_{obs} \phi_i \sum_{\{\phi_{j \neq i}\}} \phi_j^2$$

$$- \frac{\lambda}{1-k} \left(e^u - 1 \right) \left(1 - \phi_i^2 \right)^2 \tag{2.15}$$

$$\frac{\partial c}{\partial t} = \nabla \cdot \left(D_L c q(\vec{\phi}) \nabla u - a_t W_o c_l^o (1-k) e^u \sum_i \frac{\partial \phi_i}{\partial t} \frac{\nabla \phi_i}{|\nabla \phi_i|} \right). \tag{2.16}$$

The index i counts over the number of crystals, each tracked by the function (field) ϕ_i, and c is the concentration field. τ_ϕ is the isotropic time constant for all crystals and W_ϕ is the isotropic interface width. The last term on the first line of Eq. (2.15) constitutes the interaction or double obstacle potential, which determines the interaction between multiple crystals, with α_{obs} setting the strength of the interaction.

2.2 Phase-Field-Crystal Modelling

2.2.1 Standard Model: Pure Materials

The standard PFC free energy functional for a single component can be written as

$$\mathcal{F}[n] = \int d\mathbf{r} \left\{ \frac{n}{2} \left[r + \left(1 + \nabla^2 \right)^2 \right] n + \frac{n^4}{4} \right\}. \tag{2.17}$$

n is the dimensionless coarse-grained (ensemble- or time- averaged) periodic atomic number density field and $r \sim (T - T_m)$ is the reduced temperature. As written, Eq. (2.17), has been used in the study of liquid crystals, colloids and most notably Rayleigh-Bénard convection where it has been coined the Swift-Hohenberg [28] model[||]. Elder and co-workers [16, 17] proposed Eq. (2.17) as an efficient modelling formalism that is capable of describing equilibrium and non-equilibrium phenomena on mesoscopic time scales for metallic systems. Being minimized by periodic fields, the model also naturally gives rise to elastic and plastic effects as well as atomic scale interfaces and topological defects.

Even at such a simplistic level, the PFC model of Eq. (2.17) is a powerful modelling technique. In 1D the functional is minimized by a striped phase, triangular structure in 2D and body-centered cubic (BCC) structure in 3D[**]. To examine the equilibrium phase space, a minimization procedure

---

[||]After appropriate parameter rescaling.

[**]Since its original introduction, it has been found to also support FCC and HCP [54] in deep quench regions of the phase

is applied to the energy functional. To do so, we insert into the functional, an *Ansatz* for the density in the form of a mode expansion. A general, single-mode, expansion for the density can take the form

$$n = n_o(\mathbf{r}) + \sum_{\{\mathbf{q}_j, j \neq 0\}} A_j(\mathbf{r}) \, e^{i\mathbf{q}_j \cdot \mathbf{r}} + c.c. \tag{2.18}$$

$n_o(\mathbf{r})$ is the dimensionless average density of the system, A_j are the Fourier coefficients, i.e., complex amplitudes, of the reciprocal lattice vectors, $\{\mathbf{q}_j\}$ is the minimum set of reciprocal lattice vectors and $c.c.$ denotes the complex conjugate.

For the purposes of building a phase diagram, the complex amplitudes are assumed real and constant for all reciprocal lattice vectors, i.e., $A_j \equiv \varphi$ for all j. Similarly, the average density is set to a constant. For 1D and 2D cases of striped and triangular phases, the mode approximations can be simplified to,

$$n_{str} = n_o + \varphi \sin(qx), \tag{2.19}$$

$$n_{tri} = n_o + \varphi \left[\cos(qx) \cos\left(\frac{qy}{\sqrt{3}}\right) - \frac{1}{2} \cos\left(\frac{2qy}{\sqrt{3}}\right) \right], \tag{2.20}$$

respectively, where $q = |\mathbf{q}_j|$ is the wavenumber for the given structure, which is inversely proportional to the periodicity or lattice spacing. Following standard minimization techniques, we substitute these mode approximations into the free energy functional, integrate over a single-mode unit cell for the respective structure, and minimize for the unconstrained parameters φ and q. Minimization will yield the equilibrium, i.e., selected, values for each respective variable. Namely, we have

$$\varphi_{eq} \equiv \frac{\delta \mathcal{F}}{\delta \varphi} = 0 \tag{2.21}$$

$$q_{eq} \equiv \frac{\delta \mathcal{F}}{\delta q} = 0. \tag{2.22}$$

For example, the equilibrium wavenumbers are $q_{eq} = 1$ and $q_{eq} = \sqrt{3}/2$ for the striped and triangular phases respectively. The equilibrium values are then substituted back into the integrated free energy functional, where the resulting energy is only a function of the dimensionless average density, n_o, and the reduced temperature r. To calculate the phase diagram, we next minimize the free energy with respect to the constrained variable, n_o. Specifically, standard application of the so-called *common tangent*[††] or the equivalent Maxwell equal area construction leads to Fig. 2.2 for a 2D system[‡‡]. The liquid free energy used in the common tangent construction has trivially been calculated by inserting $\varphi_{eq} = 0$ and $q_{eq} = 0$ in the integrated free energy functional. The reader is referred to Appendix B or Refs. [2, 17] for greater detail on phase diagram calculation procedures in PFC models.

2.2.2 Derivation From Classical Density Functional Theory

As stated, the standard PFC model is phenomenological. It was not until the work of Jin and Khatchaturyan [21] and Elder *et al.* [18] in the context of binary alloys, which showed that it was formally possible to derive PFC models from the microscopic classical density functional theory of freezing.

Classical density functional theory has been used extensively in the study of solid-liquid systems in studying the static energetic properties of such systems and also the dynamic properties through,

---

diagram of this model.

[††]Porter and Easterling [55] provides a good source for the common tangent construction.

[‡‡]Note, the realized equilibrium states are a consequence of the mode approximations used. Other mode approximations may give rise to additional metastable or stable phases supported by this PFC free energy functional.
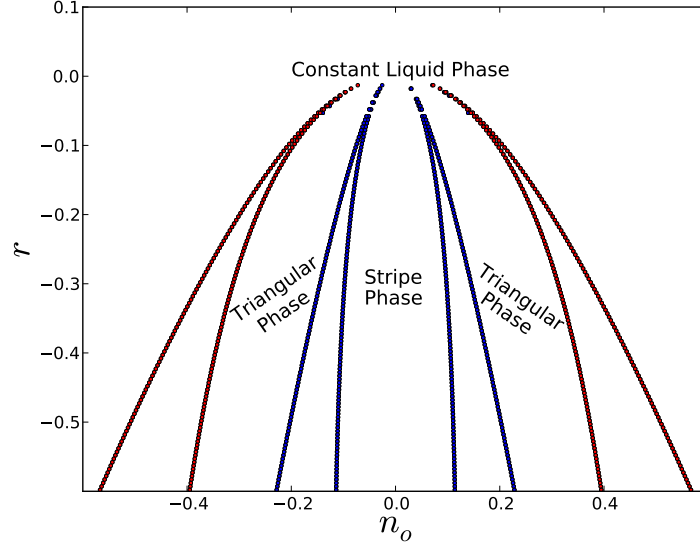
Figure 2.2: Phase diagram produced with the standard PFC free energy functional of Elder and co-workers for pure materials, for a 2D system showing both stripe and triangular phases.

so-called, dynamical density functional theory. CDFT energy functionals, using a Helmholtz formalism, can usually be written in terms of three separate contributions, expanded around the liquid state

$$\Delta \mathcal{F}[\rho] = \int d\mathbf{r} \left\{ \Delta F_{id} + \Delta F_{exc} + \Delta F_{ext} \right\}, \qquad (2.23)$$

where $\Delta \mathcal{F} = \mathcal{F} - \mathcal{F}^\ell$, with $\mathcal{F}^\ell$ being the liquid free energy functional, ΔF_{id} is the entropic, ideal gas or exact one-body component of the free energy of the system, ΔF_{exc} is excess energy, which accounts for all higher order interactions between particles and ΔF_{ext} is the effective energy cost of interacting with external fields acting on the system. ΔF_{id} and ΔF_{ext} in the CDFT free energy can be written

$$\Delta F_{id} = k_B T \left[\rho \ln \left(\frac{\rho}{\rho^\ell} \right) - \delta \rho \right], \qquad (2.24)$$

$$\Delta F_{ext} = k_B T \, V_{ext} \delta \rho, \qquad (2.25)$$

where k_B is the Boltzmann constant, T is the temperature, ρ is the unscaled atomic number density, ρ^ℓ is the reference liquid density, V_{ext} is the external potential strength and $\delta \rho = \rho - \rho^\ell$. However, an exact form for the excess term cannot be derived for most realistic systems. How this excess term is dealt with is what differentiates between various classical density functional theories. Of interest, and what has become the standard in PFC modelling, is the functional Taylor series expansion of Ramakrishnan and Yussouff [22] around $\delta \rho$. Namely

$$\Delta F_{exc} = -\frac{1}{2} k_B T \delta \rho \int d\mathbf{r}' C_2(\mathbf{r}, \mathbf{r}') \delta \rho(\mathbf{r}') + \cdots, \qquad (2.26)$$

where $C_2(\mathbf{r}, \mathbf{r}')$ is the two-point direct correlation function of a fluid (around the reference density ρ^ℓ), assumed isotropic, i.e., $C_2(\mathbf{r}, \mathbf{r}') \equiv C_2(|\mathbf{r} - \mathbf{r}'|)$. The Fourier transform of the correlation

function, $\hat{C}_2(q)$, can be related to the structure factor. The expansion can be carried out to all orders, however it is usually truncated at the two-particle interaction. As will be done throughout the remainder of the thesis.

To recover the PFC model, we set the external potential to zero and make two approximations. Before this, however, we define a reduced number density, $n = \rho/\rho^\ell - 1$, and substitute it into the CDFT energy. The first of the approximations is to take a series expansion of the ideal term to fourth order[§§]. This yields,

$$\Delta F_{id} = k_B T \rho^\ell \left[\frac{n^2}{2} - t\frac{n^3}{6} + v\frac{n^4}{12} \right], \tag{2.27}$$

where t and v are constants which formally should be set to one, however, higher order correlation interactions have been shown to contribute polynomial terms that can modify the coefficients. They can also be motivated from thermodynamics, as fitting parameters to the full ideal energy or bulk energy. The second approximation expands $\hat{C}_2(q)$ in powers of q^2 to fourth order. This amounts to taking a gradient expansion in real space. Specifically,

$$\hat{C}_2(q) = c_0 + c_2 q^2 + c_4 q^4 \tag{2.28}$$

where the Fourier constants c_0, c_2 and c_4, are chosen in such a manner as to smoothly fit and describe the two-point correlation function isotropically by a single peak around $q = q_{eq}$. For the standard PFC model, they are chosen to be negative, positive and negative, respectively. By describing the isotropic two-point correlation by a single peaked function, the PFC model yields density waves of a sinusoidal nature, as short wavelength terms, i.e., high q-modes, are penalized by the approximation. In real space, the expanded correlation and hence excess free energy density takes the form,

$$\Delta F_{exc} = -\frac{1}{2} k_B \rho^\ell T \, n \left(\rho^\ell c_0 - \rho^\ell c_2 \nabla^2 + \rho^\ell c_4 \nabla^4 \right) n. \tag{2.29}$$

Scaling the final free energy functional, i.e., $\Delta\mathcal{F} \to \Delta\mathcal{F}/(k_b T \rho^\ell)$, setting $t = 0$ and $v = 3$, and relating the Fourier coefficients of the direct two-point correlation function to the isothermal compressibilities and atomic radius of the material[¶¶], it can easily be seem that we attain the standard PFC model for a single component that was motivated from the Swift-Hohenberg model.

2.2.3 PFC Binary Alloy Models From CDFT

The standard PFC model, has also been extended to binary alloys. Motivated from CDFT, a binary alloy model was derived as was done previously with the pure material. For a binary mixture of A and B atoms, one can write a corresponding CDFT scaled free energy functional, neglecting any external source terms, truncated at the two-particle correlations, as

$$\begin{aligned}
\frac{\Delta\mathcal{F}}{k_B T} = \int d\mathbf{r} \Bigg\{ &\rho_A \ln\left(\frac{\rho_A}{\rho_A^\ell}\right) - \delta\rho_A + \rho_B \ln\left(\frac{\rho_B}{\rho_B^\ell}\right) - \delta\rho_B \\
&- \frac{1}{2}\delta\rho_A \int d\mathbf{r}' C_2^{AA}(\mathbf{r}, \mathbf{r}')\delta\rho_A(\mathbf{r}') - \frac{1}{2}\delta\rho_A \int d\mathbf{r}' C_2^{BB}(\mathbf{r}, \mathbf{r}')\delta\rho_B(\mathbf{r}') \\
&- \delta\rho_A \int d\mathbf{r}' C_2^{AB}(\mathbf{r}, \mathbf{r}')\delta\rho_B(\mathbf{r}') \Bigg\}
\end{aligned} \tag{2.30}$$

[§§]Analogous to typical approaches in expanding many phase-field type free energy functionals in polynomial series.

[¶¶]The reader is referred to Refs. [18, 2] for details about the parameter rescaling.

where ρ_i $(i = A, B)$ is the unscaled atomic number density of A and B atoms respectively, $\delta\rho_A = \rho_A - \rho_A^\ell$ and $\delta\rho_B = \rho_B - \rho_B^\ell$, ρ_A^ℓ and ρ_B^ℓ are the reference liquid density for A and B respectively, $C_2^{ij}(i, j = A, B)$ represents all two-particle interactions, here also assumed isotropic, for the binary mixture, where it is implicitly assumed that $C_2^{AB} \equiv C_2^{BA}$. It is preferable to rewrite the energy in terms of a single density field and a corresponding concentration field. To do so, we substitute into Eq. (2.30), the total atomic number density, $\rho = \rho_A + \rho_B$, and the fractional density or local solute concentration, $c = \rho_A/\rho$. The energy functional is now written as,

$$
\begin{aligned}
\frac{\Delta\mathcal{F}}{k_B T} = \int d\mathbf{r} \Bigg\{ & \rho \ln\left(\frac{\rho}{\rho^\ell}\right) - \delta\rho + \rho\left[c\ln c + (1-c)\ln(1-c)\right] \\
& - \frac{\rho}{2}\int d\mathbf{r}' \Big[c(\mathbf{r}')C_2^{AA}(\mathbf{r},\mathbf{r}')c(\mathbf{r}') + (1-c(\mathbf{r}'))C_2^{BB}(\mathbf{r},\mathbf{r}')(1-c(\mathbf{r}')) \\
& + 2c(\mathbf{r}')C_2^{AB}(\mathbf{r},\mathbf{r}')(1-c(\mathbf{r}'))\Big]\rho(\mathbf{r}') + \rho\, c\int d\mathbf{r}'\Big[\left(C_2^{AA}(\mathbf{r},\mathbf{r}') - C_2^{AB}(\mathbf{r},\mathbf{r}')\right)\rho_A^\ell \\
& + \left(C_2^{AB}(\mathbf{r},\mathbf{r}') - C_2^{BB}(\mathbf{r},\mathbf{r}')\right)\rho_B^\ell + \ln\left(\frac{\rho_B^\ell}{\rho_A^\ell}\right)\Big]\Bigg\}.
\end{aligned} \tag{2.31}
$$

Equation (2.31) yields an interesting result. When a binary mixture of A and B atoms is reduced to a total density and concentration field, we recover the ideal part of the original CDFT functional for a single component in terms of the unscaled atomic number density. Moreover, we also recover an ideal entropy of mixing term of statistical thermodynamics in terms of the fractional density, i.e., concentration c. The collection of correlation-containing excess terms is then reminiscent of an enthalpy type mixing term.

The Fourier transform of each direct correlation function is expanded, like in the pure material, to fourth order in q. Rewriting the energy functional in a more traditional form, like those found in PF methods, the following steps are taken: (1) redefine the energy functional in terms of the dimensionless variables, $\psi = 2c - 1$, concentration, and density, $n = \rho/\rho^\ell - 1$, (2) the resulting energy functional is expanded in a series to fourth order in ψ and n, (3) following expansion to fourth order, neglect all terms of order n, and assuming the long wavelength variation of ψ compared to n, terms of order $n\psi$ are also dropped from the energy. The simplified binary alloy PFC energy functional becomes,

$$
\begin{aligned}
\frac{\Delta\mathcal{F}}{k_B T \rho^\ell R^d} = \int d\mathbf{r} \Bigg\{ & \frac{B^\ell}{2}n^2 + B^x\frac{n}{2}\left(2\nabla^2 + \nabla^4\right)n - \frac{t}{3}n^3 + \frac{\nu}{4}n^4 \\
& + \gamma\psi + \frac{\omega}{2}\psi^2 + \frac{u}{4}\psi^4 + \frac{K}{2}|\nabla\psi|^2 \Bigg\}.
\end{aligned} \tag{2.32}
$$

B^ℓ and B^x are the liquid and solid state compressibilities respectively, and R the average atomic radius (i.e., wavelength of periodic density variation) , with d being the dimensionality. All other coefficients are functions of the coefficients of the correlation function. For proper definitions of all constants please refer to Ref. [18, 2]. Inspecting the simplified energy, we recognize a Cahn-Hilliard type model in ψ [4, 5], which has been used to describe phase separation and a ϕ-fourth or Ginzburg-Landau type energy in n, which has been used to study order-disorder and other phase transition phenomena.
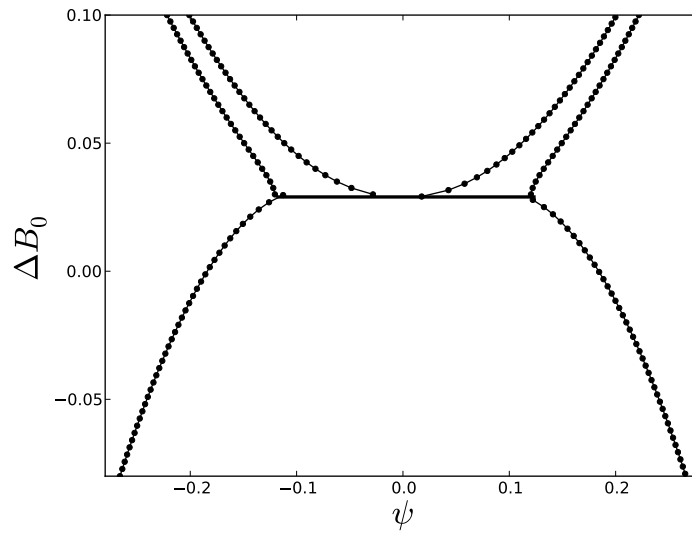
(a)
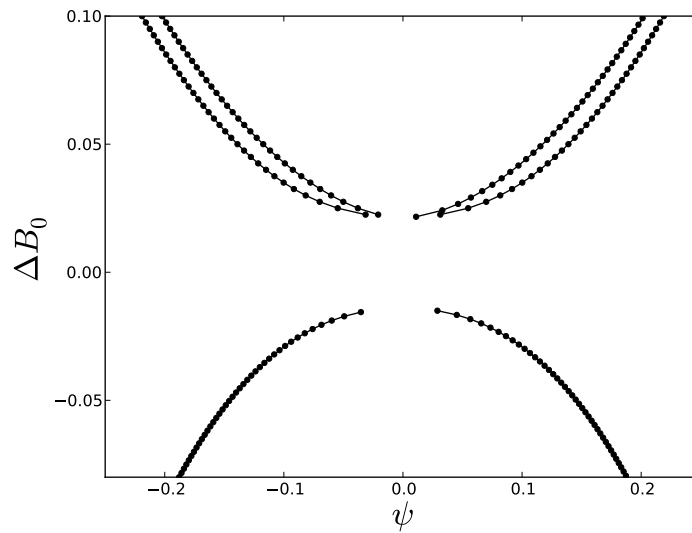
(b)

Figure 2.3: Binary alloy phase diagrams produced with the simplified PFC free energy functional of Eq. (2.32). (a) Eutectic phase diagram calculated with $\omega = 0.008$. (b) Spinodal phase diagram calculated with $\omega = 0.088$. All other parameters can be found in the text.

Equilibrium Properties

Like the pure material, we can examine the phase space of stable states admitted by this binary alloy model. In 2D, the simplified PFC energy functional yields spinodal and eutectic type phase diagrams. Here we consider the expansion of the moduli where $B_\ell = B_0^\ell + B_2^\ell \psi^2$ and $B^x = B_0^x$, where then $\Delta B_0 = B_0^\ell - B^x$ sets the energy scale, i.e., temperature scale, for the system. A spinodal and a eutectic alloy are differentiated, in this PFC model, by choice of the parameter ω, which being the coefficient of the quadratic term in the Cahn-Hilliard portion of the energy scales the critical transition temperature. We set $B_2^\ell = -1.8$, $B_0^x = 1$, $t = 0.6$, $\gamma = 0$, $\nu = 1$, $u = 4$ and assume we are at the reference density and set $n_o = 0$ in the single-mode approximation for our triangular structure. We then minimize the energy for the equilibrium wavenumber, q, and amplitude, φ. Substitution of the equilibrium parameters back into the free energy, and a common tangent or the equivalent Maxwell equal area construction yields Fig 2.3.

2.2.4   PFC Dynamics

In this section we discuss the dynamics of the standard PFC models in the context of the simplified binary alloy model. Since it couples the dimensionless density and concentration fields, respectively, it will naturally give rise to equations of both. We present here the general set of dynamics that can be applied to this free energy.

The density and concentration fields are both conserved quantities. It follows then that, the evolution of the concentration and density fields will be driven by fluxes derived from variations of the free energy in Eq. (2.32). Since both n and ψ represent conserved fields, we can write down a set of Model B equations for each respective field. They are,

$$\frac{\partial n}{\partial t} = \nabla \cdot \left(M_n \nabla \frac{\delta F}{\delta n} \right), \tag{2.33}$$

$$\frac{\partial \psi}{\partial t} = \nabla \cdot \left(M_\psi \nabla \frac{\delta F}{\delta \psi} \right), \tag{2.34}$$

where $F = \Delta \mathcal{F} / (k_B T \rho^\ell R^d)$ and M_i are the mobilities of n or ψ respectively. However, having derived the functional from CDFT in terms of two densities, A and B, we can also formally derive the dissipative dynamics from the free energy density of the original free energy written in terms of ρ_A and ρ_B. The dynamics will be shown to be approximately equivalent, under an equal mobility assumption between densities A and B, to the ones just derived above.

Individually, both densities A and B, are conserved quantities. If the combined mixture of both is assumed to be driven to energy minimization through conserved dissipative dynamics, then we have the following,

$$\frac{\partial \rho_A}{\partial t} = \nabla \cdot \left(M_A \nabla \frac{\delta F}{\delta \rho_A} \right)$$
$$\frac{\partial \rho_B}{\partial t} = \nabla \cdot \left(M_B \nabla \frac{\delta F}{\delta \rho_B} \right) \tag{2.35}$$

where M_A and M_B are the mobilities of A or B respectively, and in general are temperature and density dependent. In the limit of small n, we make the following approximation for the concentration field,

$$\psi \approx \frac{\rho_A - \rho_B}{\rho^\ell}. \tag{2.36}$$

This allows us to re-write the variational derivatives using chain rule as,

$$\frac{\delta F}{\delta \rho_A} = \frac{1}{\rho^\ell} \frac{\delta F}{\delta n} + \frac{1}{\rho^\ell} \frac{\delta F}{\delta \psi},$$
$$\frac{\delta F}{\delta \rho_B} = \frac{1}{\rho^\ell} \frac{\delta F}{\delta n} - \frac{1}{\rho^\ell} \frac{\delta F}{\delta \psi}, \tag{2.37}$$

thus allowing the equations of motion to be cast in terms of the dimensionless field variables,

$$\frac{\partial n}{\partial t} = \nabla \cdot \left(\frac{(M_A + M_B)}{(\rho^\ell)^2} \nabla \frac{\delta \mathcal{F}}{\delta n} \right) + \nabla \cdot \left(\frac{(M_A - M_B)}{(\rho^\ell)^2} \nabla \frac{\delta F}{\delta \psi} \right)$$
$$\frac{\partial \psi}{\partial t} = \nabla \cdot \left(\frac{(M_A - M_B)}{(\rho^\ell)^2} \nabla \frac{\delta F}{\delta n} \right) + \nabla \cdot \left(\frac{(M_A + M_B)}{(\rho^\ell)^2} \nabla \frac{\delta F}{\delta \psi} \right), \tag{2.38}$$

where

$$\frac{\delta F}{\delta n} = B^\ell n + B^x \left(2\nabla^2 + \nabla^4 \right) n - tn^2 + \nu n^3,$$
$$\frac{\delta F}{\delta \psi} = \frac{\partial B^\ell}{\partial \psi} \frac{n^2}{2} + \omega \psi + u\psi^3 - K\nabla^2 \psi. \tag{2.39}$$

When substitutional alloys are of interest, $M_A = M_B$, thus simplifying the dynamical equations to

$$\frac{\partial n}{\partial t} = \nabla \cdot \left(M\nabla \frac{\delta \mathcal{F}}{\delta n} \right)$$
$$\frac{\partial \psi}{\partial t} = \nabla \cdot \left(M\nabla \frac{\delta F}{\delta \psi} \right), \tag{2.40}$$

similar to the set of equations derived above, where $M = (M_A + M_B)/(\rho^\ell)^2$.

For a simple model with a limited number of parameters, the standard PFC models have been used to investigate a number diverse of phenomena. It has been found that these phenomena are well described by PFC models. Some of the phenomena include; dendritic and eutectic solidification [18, 56], crystal nucleation [57, 56, 58, 59], surface tensions and interfacial energies [60, 61, 62], spinodal decomposition in the presence of dislocations [18], Kirkendall effect in binary alloys [63], grain boundary melting and premelting [64, 65] and plasticity and dislocation dynamics [66, 65].

However successful the method has been, two outstanding features have been distinctly missing from the standard formalism. The first being the ability to generate a range of stable crystal structures self-consistently and the second is the modelling of realistic material phase diagrams. Greenwood *et al.* [19, 20] have recently introduced a new PFC formalism which rectifies this shortcoming of the standard model. We review their contribution next.

2.2.5 Structural Transformations with Phase-Field-Crystals

Despite the tremendous success of the initial PFC model, and its variants, the inability to support a wide range of crystal structures and generate realistic phase diagrams presented a major weakness. Recently, Greenwood *et al.* [19, 20] have introduced a new PFC formalism, so-called structural PFC (XPFC), that begins with the free energy functional of CDFT. The entropic contribution of the free energy functional is expanded around the reference liquid density to quartic order, while particle interactions forgo the gradient expansion of the standard PFC models and instead are encoded in a two-point direct correlation function in reciprocal space. The method is briefly reviewed here.

The free energy functional for the pure XPFC model is derived from the CDFT of Ramakrishnan and Yussouff [22], made up of two contributions. The first is the one-body, ideal energy which

drives the system to constant homogenous fields, i.e., liquid. While the second contribution, is an excess term in particle interactions, truncated at the two-particle interaction that drives the system to be minimized by periodic fields, i.e., solid. In reduced density form, the resulting XPFC energy functional can be written as [19, 20]

$$\frac{\Delta \mathcal{F}}{k_B T \rho^\ell} = \int d\mathbf{r} \left\{ \frac{\Delta F_{id}}{k_B T \rho^\ell} + \frac{\Delta F_{exc}}{k_B T \rho^\ell} \right\}, \tag{2.41}$$

where,

$$\frac{\Delta F_{id}}{k_B T \rho^\ell} = \frac{n^2}{2} - \eta \frac{n^3}{6} + \chi \frac{n^4}{12}$$

$$\frac{\Delta F_{exc}}{k_B T \rho^\ell} = -\frac{n}{2} \int d\mathbf{r}' C_2(|\mathbf{r} - \mathbf{r}'|)\, n(\mathbf{r}'). \tag{2.42}$$

ΔF_{id} comprises the ideal energy term which drives the system to uniform states, while ΔF_{exc} is the excess energy term which drives the system to periodic states. n is the dimensionless number density, k_B is the Boltzmann constant, T is the temperature and ρ^ℓ is the reference liquid density of the system. η and χ are constants, strictly equal to unity, however as discussed in the Ref. [20] deviations from unity allow for better tuning to the full ideal energy and can also aid in mapping to thermodynamic parameters and can physically be motivated from the lowest-order component of higher-order particle correlation functions [67]. Finally, $C_2(|\mathbf{r} - \mathbf{r}'|)$ is the isotropic, direct two-point correlation function at the reference density, ρ^ℓ. The construction of this latter expression is what differentiates the XPFC from other PFC models. We discuss the nature of this kernel in the following.

Correlation Function, $C_2(|\mathbf{r} - \mathbf{r}'|)$

The correlation kernel for the XPFC model is constructed in Fourier space, since real space convolutions are simply multiplicative in Fourier space. This also makes the XPFC formalism better equipped for simulation in Fourier space. The correlation function $C_2(|\mathbf{r} - \mathbf{r}'|)$ is thus constructed directly in Fourier space, at the reference density ρ^ℓ, denoted as $\hat{C}_2(q)$. A reciprocal space peak of $\hat{C}_2(q)$ [20], for a given mode, j, i.e., a peak corresponding to a *family* of planes, for the desired crystal structure is denoted by

$$\hat{C}_{2j} = e^{-\frac{\sigma^2 q_j^2}{\rho_j \beta_j}} e^{-\frac{(q - q_j)^2}{2\alpha_j^2}}. \tag{2.43}$$

Including only those peaks of the most dominant family of planes, the total correlation function for the crystal structure of interest, $\hat{C}_2$, is then defined by the *numerical envelope* of all peaks $\hat{C}_{2j}$. The first exponential in Eq. (2.43) sets the temperature scale via a Debye-Waller like prefactor that employs an effective temperature parameter, σ, which can be related to the vibrational amplitude of atoms in the unit cell. ρ_j and β_j represent the planar and atomic densities, respectively, associated with the family of planes corresponding to mode j. These parameters are formally properties of the crystal structure, but can be exploited as constants for convenience and fitting purposes. The second exponential sets the spectral peak position at q_j, where q_j is the inverse of the interplanar spacing for the jth family of planes in the unit cell of the crystal structure. Unlike spectral Bragg peaks resulting from diffraction experiments for single crystals or structure factor calculations, here, each peak is represented by a Gaussian function, with α_j being the width of the peak, j. The width parameter, α_j, has been shown in Ref. [20] to set the elastic and surface energies, as well as their anisotropic properties.

Finally a comment about the $q = 0$ mode of the correlation function. This mode is the infinite wavelength mode and sets the bulk compressibilities of the system. For simplicity, in Refs. [19, 20], the value of the $q = 0$ mode was set to zero. A nonzero amplitude at $q = 0$, however, merely shifts

the local free energy at densities away from the reference density, thereby causing a compression of the phase diagram about the reference density [20]. This, however, does not alter the stability of the equilibrium crystal structure, since the correlation kernel is constructed about the reference density.

Equilibrium Properties

The free energy of Eqs. (2.41)-(2.43), can be shown to admit coexistence of varying crystal structures in equilibrium with liquid [19, 20]. In 2D, square-liquid and triangle-liquid. In three-dimensions (3D), face-centered cubic (FCC) and liquid, Hexagonal-close packed (HCP) and liquid and BCC and liquid. However, the free energy of Eqs. (2.41)-(2.43) can also yield peritectic systems in both 2D and 3D where multiple solid phases and liquid can coexist. These peritectic systems are comprised of square-triangle-liquid and FCC-BCC-liquid in 2D and 3D respectively.

Before proceeding to construct the peritectic phase diagrams, a word concerning the mode approximation for the density. We calculate the respective energies by considering single-mode approximations for the BCC and triangular phases and two-mode approximations for the FCC and square phases. The periodic phases (square, triangle, FCC and BCC) are then approximated by the sum of these density modes as defined by,

$$n_i(\mathbf{r}) = n_o + \sum_j \varphi_j \sum_l e^{\frac{2\pi}{a_i}(i\mathbf{q}_l \cdot \mathbf{r})},$$

(2.44)

where the subscript i denotes a particular solid phase, i.e., $i = FCC$ represents an FCC phase with lattice spacing a_{FCC}, j is the index over the included modes of the i-phase, φ_j*** is the amplitude of mode j and l is the index over the collection of reciprocal space peaks corresponding to mode j. Accordingly, $\mathbf{q}_l$ is the reciprocal lattice vector normalized to a lattice spacing of 1, corresponding to each index l.

Following similar minimization procedures already established for the standard PFC models, and detailed in Appendix B, Fig. 2.4 results for the standard XPFC free energy in 2D and 3D. The phase diagrams, has as input, a correlation kernel of a square crystal lattice for the 2D system, and a kernel for an FCC crystal lattice for the 3D system. As an example, to stabilize a square crystal structure, the correlation function requires two peaks, q_{10} and q_{11}, corresponding to the first two primary family of planes for a square crystal structure. We choose, $q_{10} = 2\pi$ and $q_{11} = 2\pi\sqrt{2}$ and set, $\rho_{10} = 1$, $\beta_{10} = 1$, $\alpha_{10} = 1$ and $\rho_{11} = 4$, $\beta_{11} = 4$, $\alpha_{11} = 1$. To stabilize the triangular structure, only a single primary peak is necessary. We re-scale the position of that peak to be commensurate with the q_{10} peak of the square. In doing so, the square correlation kernel can simultaneously permit square and triangular structures, where the structure with the minimum energy can be parameterized by the average density, n_o, and temperature, σ. After re-scaling, the emergent crystal structures will have dimensionless lattice spacings of $a_{sq} = 1$ and $a_{tri} = 2/\sqrt{3}$, respectively. A similar approach is used in the construction of the 3D FCC-BCC-liquid system.

This improvement on the standard PFC methodology brings to the fold a very useful modelling formalism derived from atomistics and capable of describing relevant material crystal structures and realistic phase diagrams. Part of the aim of this thesis is to extend this formalism to more complex systems and scales. Presented in Chapters 4-7, are extensions of the XPFC method to N-component, binary and ternary alloys, and a corresponding complex amplitude model to exploit larger scales.

Having gone through the background of the techniques which we will build upon throughout this thesis, we are ready to move on to their application to microstructural evolution in material systems. The following chapter will begin the research portion of this thesis, where we start by examining microstructural evolution in nanocrystalline systems under external driving conditions.

***For multi-mode structures, the amplitudes for different modes are not independent in constructing phase diagrams. In principle, we should conduct a multi-variable minimization. This will lead to lengthy and intractable expressions. Based on empirical observation, we use their ratio, e.g., $\varphi_2 = f\varphi_1$, evaluated at $\sigma = 0$, for all temperatures.
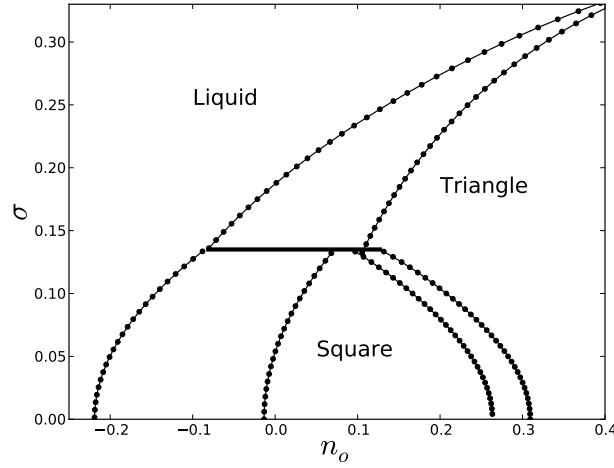
(a)
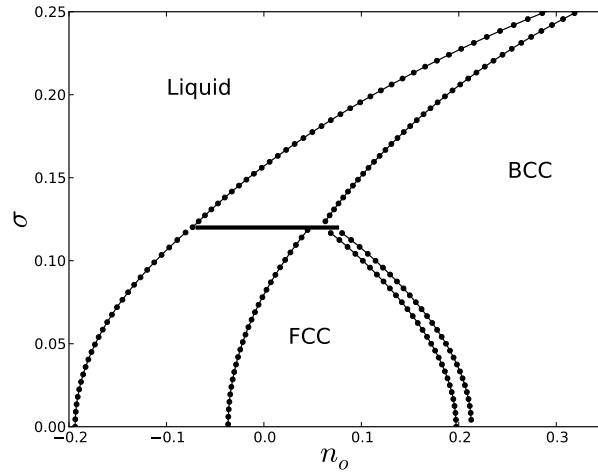
(b)

Figure 2.4: Sample phase diagrams resulting from the minimization of the XPFC free energy functional of Eq. (2.41). (a) We have a peritectic phase diagram for 2D structures. Parameters were chosen to be: $q_{10} = 2\pi$ and $q_{11} = 2\pi\sqrt{2}$, and $\rho_{10} = 1$, $\beta_{10} = 4$, $\alpha_{10} = 1$ and $\rho_{11} = 1/\sqrt{2}$, $\beta_{11} = 4$, $\alpha_{11} = 1$. The emergent square and triangle structures have dimensionless lattice spacings of $a_{sq} = 1$ and $a_{tri} = 2/\sqrt{3}$ respectively. (b) 3D peritectic phase diagram. Parameters were chosen to be: $q_{111} = 2\sqrt{3}\pi$ and $q_{200} = 4\pi\sqrt{2}$, and $\rho_{111} = 1$, $\beta_{111} = 4$, $\alpha_{111} = 1$ and $\rho_{200} = 1/\sqrt{2}$, $\beta_{200} = 3$, $\alpha_{200} = 1$. The emergent FCC and BCC structures have dimensionless lattice spacings of $a_{FCC} = 1$ and $a_{BCC} = \sqrt{2/3}$ respectively. The glitch in the phase diagrams around the peritectic temperature is due to the accuracy of the mode approximation and numerical solution.

Chapter 3

Microstructural and Phase Stability in Driven Nanocrystalline Systems

The previous chapter explored the origins and differences between the phase-field (PF) and phase-field-crystal (PFC) approaches. The PF method has seen great success, particular in the modelling of solidification. Microstructure and phase evolution however, is not limited to systems undergoing solidification. Over the past few decades, there has been a rise in the exploration of nanocrystalline (NC) materials as practical replacements for components and parts in varying industries. Owing to their nano-scale features and susceptibility in having a high density of grain boundaries and phase boundaries, the mechanical, chemical, electrical and optical properties of NC materials often differ drastically from polycrystalline materials. The aim of this chapter is to examine the stability and microstructural evolution of a class of NC materials in environments where they are exposed to external driving forces. This chapter will utilize the standard PFC method, in its ability to incorporate atomic-scale elastic and plastic effects and the structure of grain boundaries, to study NC materials under forced external conditions.

3.1 Motivation

Whether for tuning nanostructure size features in components during their fabrication (microelectronics) or as full size components in nuclear reactors, the microstructural and phase stability of these components, when exposed to external driving, is paramount. These external processes may be attributed to neutron or electron irradiation (in nuclear systems), ion-beam mixing (in fabrication of microelectronics) or continued plastic deformation (leading to cyclic fatigue, e.g. high energy milling) [68]. Of importance in these systems is the structural integrity of components. The system is driven out of equilibrium (as described by thermally activated processes, i.e., thermodynamic equilibrium), and in the thermodynamic limit, a system may exhibit chemical or structural modifications manifested in microstructural and phase alterations. The resulting long-time configurations of these systems are then dependent on the conditions responsible for external driving.

For conventional, polycrystalline materials, there are several exhaustive reviews and no shortage of literature on materials under external driving conditions, particularly when the forcing condition is a flux of energetic particles (such as electrons, ions or neutrons) [68, 69, 70]. Several interesting and unique phenomena can occur in these materials. Examples include precipitation in under-saturated solid solutions [71, 72, 73], the lowering of the critical point in second order-disorder transitions [74, 68], the patterning of dislocations [75] and the amorphization of crystalline materials [76, 68]. External driving is also usually accompanied by the production of excess point defects, which among other things enhance thermal diffusion. The common denominator in all driven sys-

tems, is that they achieve an altered dynamical state, where the configuration of said state is a function of the material properties and forcing conditions [68]. The resulting state can be rationalized as being caused by the long-time effect of two parallel yet competing mechanisms: thermally activated atomic jumps and the forced (athermal ballistic) atomic jumps arising from external forcing. Current research trends suggest that a method to alleviate the effects of these athermal ballistic effects is the use of NC materials, which feature a very high density of potential point defect sinks such as grain boundaries or interphase boundaries. Recently, Bai *et al.* [77] have outlined a theoretical explanation for the apparent resistance/tolerance of NC materials (in pure Cu) to ballistic conditions. This resistance to ballistic effects has also been observed experimentally by Rose and coworkers [78, 79] on NC Pd and ZrO_2 materials, Hochbauer *et al.* [80] on Cu-Nb multilayers and in various atomistic simulations [81, 82, 83]. Unfortunately, most existing atomistic models are not capable of capturing the long-time scales relevant for studying sustained ballistic effects. While techniques have been developed to accelerate atomistic simulations [77], it is not clear if these methods can be extended to a time scale appropriate for the solid state diffusion mechanisms controlling the microstructural and phase stability of NC materials.

Here we integrate the continuum mesoscopic model of ballistic effects in driven systems, proposed by Enrique and Bellon [1], into the atomistic scale PFC and XPFC modelling formalism. The aim is to create a theoretical framework capable of describing the long-time microstructural evolution and phase stability, incorporating density and compositional variations, of materials under ballistic conditions.

This chapter is organized as follows. Firstly, in Section 3.2, we briefly review the model of Enrique and Bellon [1] and highlight what we feel are the most important results from their initial introduction and application of the model. Next, in Section 3.3, we describe how to incorporate the ballistic model of Enrique and Bellon into the atomistic PFC and XPFC models. Following that, in Section 3.4, we discuss the equilibrium properties of the resulting effective free energy functionals. We then report on the long-time evolution of a pure polycrystalline NC material under ballistic condition in Section 3.5. We end the chapter with some conclusions and some future directions of this work.

3.2   Constructing a Free Energy for a Driven System

Enrique and Bellon [1, 84] recently developed a continuum description of alloys subjected to external driving via ballistic events. The underlying theme of their model is the competing dynamics between two dynamical mechanisms: one which is thermally driven to bring the system to thermodynamic equilibrium; and the other is athermal particle exchanges driving the system out of equilibrium, an idea which dates back to Martin [85]. This is accomplished through an effective free energy functional of the Cahn-Hilliard form, whereby they forgo the explicit description of discrete interactions and supersaturation of excess point defects and instead make use of effective interactions to account for the long-time effects of ballistic contributions. We review their model briefly.

Wanting to examine the role of external ballistic driving on compositional patterning, Enrique and Bellon start of by describing the time evolution of the compositional (dimensionless) field. The time evolution of the compositional field has two contributions, the thermal and athermal/ballistic contribution, respectively. We have,

$$\frac{\partial \Psi}{\partial t} = \frac{\partial \Psi^{\text{th}}}{\partial t} + \frac{\partial \Psi^{\text{bal}}}{\partial t} \qquad (3.1)$$

where Ψ is the compositional difference around some reference state. The thermal contribution to

the dynamics is attained from conserved dissipative dynamics of some free energy, $\mathcal{F}$. That is,

$$\frac{\partial \Psi^{\text{th}}}{\partial t} = M\nabla^2 \frac{\delta \mathcal{F}}{\delta \Psi}, \tag{3.2}$$

where M is the mobility, and $\mathcal{F}$ is the equilibrium free energy functional. For the ballistic contribution, they introduce a term describing the rate of composition change due to ballistic exchanges. They define this as,

$$\frac{\partial \Psi^{\text{bal}}}{\partial t} = -\Gamma(\Psi - \langle \Psi \rangle_{\mathcal{R}}), \tag{3.3}$$

where Γ is the frequency of forced atomic exchanges, proportional to the flux of incident particles. $\langle \Psi \rangle_{\mathcal{R}}$ is the spatially weighted average of composition variations due to forced atomic exchanges, with an average distribution distance $\mathcal{R}$. The weighted average is well described by the convolution,

$$\langle \Psi \rangle_{\mathcal{R}} = \int d\mathbf{r}' w_{\mathcal{R}}(\mathbf{r} - \mathbf{r}')\Psi(\mathbf{r}'), \tag{3.4}$$

leading to the total dynamics described by,

$$\frac{\partial \Psi}{\partial t} = M\nabla^2 \frac{\delta \mathcal{F}}{\delta \Psi} - \Gamma(\Psi - \langle \Psi \rangle_{\mathcal{R}}), \tag{3.5}$$

where $w_{\mathcal{R}}$ is a normalized weight function which describes the distribution distances of ballistic exchanges. An effective energy functional can then be deduced that gives rise to the kinetics described by Eq. (3.5). This effective functional has the form,

$$E = \mathcal{F} + \gamma G \tag{3.6}$$

where $\gamma = \Gamma/M$ is the reduced forcing frequency or flux of incident particles. G is an effective external energy term due to ballistic effects. It is described by a self interaction of the form

$$G = \frac{1}{2} \int d\mathbf{r}\, d\mathbf{r}' \Psi(\mathbf{r}) g\left(\mathbf{r} - \mathbf{r}'\right) \Psi(\mathbf{r}'), \tag{3.7}$$

where g is a kernel that obeys $\nabla^2 g(\mathbf{r} - \mathbf{r}') = -[\delta(\mathbf{r} - \mathbf{r}') - w_R(\mathbf{r} - \mathbf{r}')]$. The equilibrium free energy functional of the Cahn-Hilliard form is chosen as it describes compositional patterning through phase separation well. It is

$$\mathcal{F} = \int d\mathbf{r} \left(-A\Psi^2 + B\Psi^4 + C|\nabla\Psi|^2\right), \tag{3.8}$$

where $A, B,$ and C are constants determined to fit material properties. The effective energy E, modifies the equilibrium free energy $\mathcal{F}$, due to ballistic events. Driving the system towards the equilibrium of the functional E, the dynamics can then be defined by

$$\frac{\partial \Psi}{\partial t} = M\nabla^2 \frac{\delta E}{\delta \Psi}. \tag{3.9}$$

The main findings of interest in the initial work of Enrique and Bellon were the stability analysis performed on their kinetic equations. These main findings are represented graphically in Figs. 3.1 and 3.2. Figure 3.1 plots the growth rate as a function of perturbations of the wavenumber k. It was attained by doing a linear stability analysis by insertion of a perturbation of the form $\Psi = \Psi_{eq} + \delta\Psi$, where $\delta\Psi = e^{\omega t + \mathbf{ikr}}$, into the composition in the dynamic equation, where $\Psi_{eq} = 0$ is the equilibrium solution. Of note is that in the absence of ballistic exchanges, i.e., $\gamma < \gamma_1$, one recovers the usually dispersion relation associated with spinodal decomposition. However, for a given range of reduced frequency, i.e, $\gamma_1 < \gamma < \gamma_2$, we find that there exists both an upper and

lower bound of the allowed wavenumbers that the system can select, suggesting that there is a local instability for the allowed window of k values. For critical values of the reduced frequency, i.e., $\gamma = \gamma_2$ the homogenous solution becomes stable.
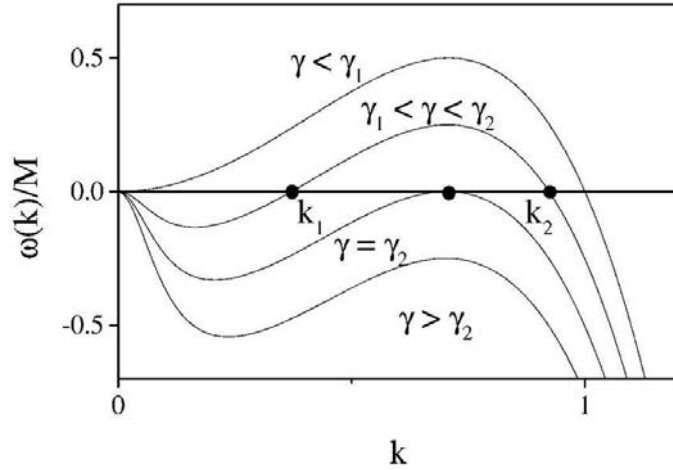
Figure 3.1: Growth rate for perturbations of wavenumber k [1].
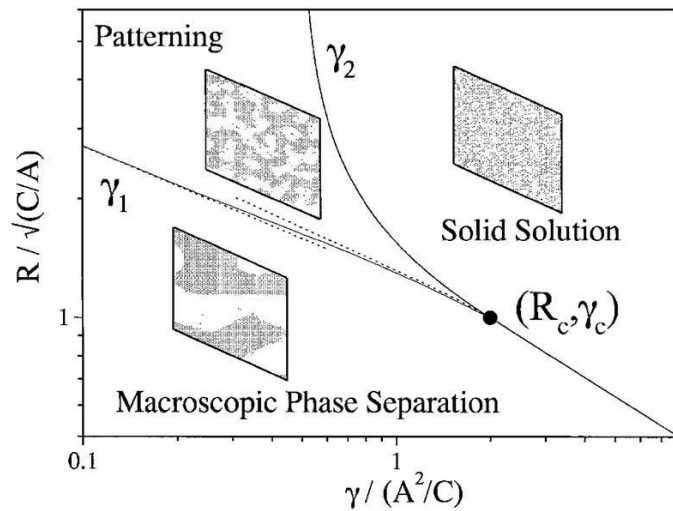
Figure 3.2: Kinetic steady state regimes as a function of energy of incident particles, $\mathcal{R}$ and reduced flux or frequency of incident particles γ [1].

Figure 3.2 plots the steady state phase space as a function of distribution distance/energy, $\mathcal{R}$, versus flux/reduced forcing frequency, γ. Worth noting is that at low energy and low flux, the system exhibits normal macroscopic phase separation of spinodal decomposition. For higher energy and high flux, the system reaches a dynamical state of a solid solution. There exists a range of energy and forcing frequency for which the system exhibits patterning, where certain length scales are stabilized. Indeed, one can wonder what this would mean for a polycrystalline system with some distribution of grain sizes. What would such a system, subjected to ballistic conditions exhibit?

The work of Enrique and Bellon provides a means to bring a traditionally atomistic description of atomic exchanges due to ballistic conditions to an effective continuum formulation. Their model

has been used to study compositional patterning in alloys driven by irradiation [1, 86], phase stability of alloys under irradiation [84], non-equilibrium fluctuations in alloys under irradiation [87] and irradiation-induced spinodal decomposition in the presence of dislocations [88]. The model can capture the appropriate long-time scales needed in examining sustained ballistic effects, unfortunately it does not incorporate different crystalline orientations, grain boundaries, defects or elasto-plastic effects. These are important features in the microstructural evolution and phase stability of NC materials under sustained external forcing. Below we extend the work of Enrique and Bellon to incorporate these effects, and attempt to elucidate in this chapter the consequences of sustained external forcing on NC materials.

3.3   Effective PFC Energy Functionals for Ballistic Mixing

In this section, we derive effective PFC energy functionals for ballistic mixing using the standard PFC model for binary alloys and the XPFC model for pure materials.

3.3.1   Standard Binary PFC Model

We begin by recalling the standard binary alloy PFC energy functional in scaled form [18],

$$\mathcal{F}_{pfc} = \int d\mathbf{r} \left\{ \frac{n}{2} \left[B^\ell + B^x \left(2\nabla^2 + \nabla^4 \right) \right] n - \frac{t}{3} n^3 + \frac{\nu}{4} n^4 + \frac{\omega}{2} \psi^2 + \frac{u}{4} \psi^4 + \frac{K}{2} |\vec{\nabla}\psi|^2 \right\} \quad (3.10)$$

where the energy is scaled by $k_B T \rho_\ell R^d$. n is the dimensionless local atomic number density, ψ the dimensionless concentration, k_B is the Boltzmann constant, T the temperature, ρ_ℓ the reference liquid density, and R the average atomic radius, with d being the dimensionality of space. B^ℓ and B^x are the dimensionless bulk moduli of the liquid and solid, respectively, setting the energy scale of the system. Following Ref. [18] and Section 2.2, we consider the expansion of the moduli where $B_\ell = B_0^\ell + B_2^\ell \psi^2$ and $B^x = B_0^x$. The remaining parameters are constants, which in principle are functions of the direct two point correlation functions, and can be calculated from first principles or fit to phenomenological databases or theories of materials properties, e.g. surface energy [60, 61, 62].

As discussed previously, n and ψ follow dissipative dynamics that minimize $\mathcal{F}_{pfc}$. To include external forced ballistic effects, the dynamics are augmented by two Enrique and Bellon like source terms in the density and concentration equations. They are written as

$$\frac{\partial n}{\partial t} = M\nabla^2 \frac{\delta \mathcal{F}_{pfc}}{\delta n} - \Gamma \left(n - \langle n \rangle_\mathcal{R} \right), \quad (3.11)$$

$$\frac{\partial \psi}{\partial t} = M\nabla^2 \frac{\delta \mathcal{F}_{pfc}}{\delta \psi} - \Gamma \left(\psi - \langle \psi \rangle_\mathcal{R} \right), \quad (3.12)$$

with M the mobility and Γ the frequency of forced atomic exchanges, proportional to the flux of incident particles. Note that Eqs. (3.11) and (3.12) are deterministic, however to incorporate the short time fluctuations of the system, in Section 3.5 when we report on numerical simulations, we append to these equations two stochastic variables, ζ and ξ, having a Gaussian distribution with zero mean and amplitudes A_ζ and A_ξ for the density and concentration fields, respectively. $\langle \psi \rangle_\mathcal{R}$ and $\langle n \rangle_\mathcal{R}$ denote the corresponding weighted spatial averages of the concentration and density differences respectively, in response to forced atomic exchanges within an average distribution distance $\mathcal{R}$. The weighted averages are defined by,

$$\langle \psi \rangle_\mathcal{R} = \int d\mathbf{r}' w_\mathcal{R}(\mathbf{r} - \mathbf{r}') \psi(\mathbf{r}') \quad (3.13)$$

and

$$\langle n \rangle_{\mathcal{R}} = \int d\mathbf{r}' w_{\mathcal{R}}(\mathbf{r}-\mathbf{r}')n(\mathbf{r}'). \tag{3.14}$$

The function $w_{\mathcal{R}}$ is a weight function describing the long-time spatial extent of ballistic exchanges in crystalline materials. A Yukawa potential was chosen as a form for the weight function in Ref.[1], which we described in Section 3.2, for the case of exchanges driven by irradiation. However, here, we adopt the 2D analog;

$$w_{\mathcal{R}}(r) = \frac{1}{2\pi\mathcal{R}^2} K_0\left(\frac{r}{\mathcal{R}}\right), \tag{3.15}$$

where K_0 is a modified Bessel function of the second kind. As stated above, $\mathcal{R}$ describes the average spatial extent of ballistic events, which can also be related to the energy of the ballistic driving force. We note that the above is the lowest order description of ballistic events in driven systems that can be included for a binary alloy model that has coupling between density and composition variations. In general Γ can take on different values for the density and concentration field, Γ_n and Γ_ψ, respectively, and two separate functions $w_{\mathcal{R}}^n$ and $w_{\mathcal{R}}^\psi$ can be introduced for each respective field. The model presented here, like the model of Enrique and Bellon, has the underlying idea that a system exposed to external driving can be described by two mechanisms acting in parallel: thermal diffusion and athermal ballistic events. Note that when $\mathcal{R} = 0$, dynamics are driven only by the thermal, i.e., thermodynamic, portions of Eqs. (3.11) and (3.12).

Including only the lowest level of description, we can construct an effective PFC energy functional for ballistic events, which affords an opportunity to explore equilibrium properties under ballistic conditions. Following Enrique and Bellon, we write the effective functional as $E_{pfc} = \mathcal{F}_{pfc} + \gamma G_{pfc}$, where G_{pfc} is the external energy source representing effective interactions arising due to ballistic effects for density and compositional variations and $\gamma = \Gamma/M$ is the reduced forcing frequency. The effective interactions are described by a self interaction energy written as

$$G_{pfc} = \frac{1}{2} \int d\mathbf{r}\, d\mathbf{r}' \left\{ n(\mathbf{r})g(\mathbf{r}-\mathbf{r}')n(\mathbf{r}') + \psi(\mathbf{r})g(\mathbf{r}-\mathbf{r}')\psi(\mathbf{r}') \right\}, \tag{3.16}$$

where the kernel for ballistic exchanges g satisfies the equation,

$$\nabla^2 g(\mathbf{r}-\mathbf{r}') = -\left[\delta(\mathbf{r}-\mathbf{r}') - w_{\mathcal{R}}(\mathbf{r}-\mathbf{r}') \right]. \tag{3.17}$$

Which is to say, the kernel satisfies the Poisson solution to a point source perturbed by a weight function.

3.3.2   XPFC Model

Having discussed, in detail, the steps in arriving at an effective energy functional for the standard binary PFC model, generating an effective functional for the pure XPFC model can readily be derived. Starting with the scaled energy functional for the XPFC model for a single component [19, 20], Section 2.2.5, we have

$$\mathcal{F}_{xpfc} = \int d\mathbf{r} \left\{ \frac{n^2}{2} - \eta \frac{n^3}{6} + \chi \frac{n^4}{12} - \frac{n}{2} \int d\mathbf{r}' C_2(|\mathbf{r} - \mathbf{r}'|)\, n(\mathbf{r}') \right\}, \tag{3.18}$$

where the energy is scaled by $k_B T \rho^\ell$, n is the dimensionless local atomic number density, k_B is the Boltzmann constant, T the temperature and ρ^ℓ is the reference liquid density. η and χ are constants, formally equal to one, however they can be exploited for tuning and fitting purposes [20].

$C_2(|\mathbf{r} - \mathbf{r}'|)$ is the isotropic, direct two-point correlation function at the reference density, ρ^ℓ. It is constructed to yield desired crystal structures of interest in equilibrium.

The dimensionless density, n, follows conserved dissipative dynamics. Like the previous section, we add to the dynamics of the density an Enrique and Bellon like source term for long time ballistic effects in density. The dynamics become,

$$\frac{\partial n}{\partial t} = M\nabla^2 \frac{\delta \mathcal{F}_{xpfc}}{\delta n} - \Gamma\left(n - \langle n \rangle_\mathcal{R}\right), \tag{3.19}$$

where M is the mobility and Γ is the frequency of forced atomic exchanges, i.e., the ballistic frequency. $\langle n \rangle_\mathcal{R}$ denotes the corresponding weighted spatial average of the density field, in response to forced atomic exchanges with an average distribution distance $\mathcal{R}$. The weighted average can be defined by, Eq. (3.13).

Following a similar procedure as outline above, we construct an effective functional of the form $E_{xpfc} = \mathcal{F}_{xpfc} + \gamma G_{xpfc}$. G_{xpfc} is the external energy source representing effective interactions arising due to ballistic effects for density variations and $\gamma = \Gamma/M$ is the reduced forcing frequency. Considering just density variations, the effective interactions are described by a self interaction energy of the form,

$$G_{xpfc} = \frac{1}{2}\int d\mathbf{r}\, d\mathbf{r}'\, n(\mathbf{r})g(\mathbf{r} - \mathbf{r}')n(\mathbf{r}'), \tag{3.20}$$

where the kernel, g, satisfies Eqs. (3.17) and (3.15) for ballistic exchanges.

After deriving the effective functionals, we now examine the properties exhibited by these functionals.

3.4 Long Wavelength and Equilibrium Properties

We first interrogate the long wavelength (i.e., phase-field limit) limit of the proposed models. Secondly, we examine their bulk properties under forced driving, i.e., kinetic phase diagrams under ballistic conditions. To examine the long wavelength properties of the models, we perform an amplitude expansion of our effective PFC and XPFC free energies, E_{pfc} and E_{xpfc}. To perform the expansion, we will be substituting into the effective free energies a single-mode expansion for the density of triangular structures and a two-mode expansion for structures of square symmetry. The multi-mode approximation can be written generally as

$$n_i(\mathbf{r}) = n_o(\mathbf{r}) + \sum_l \sum_j \eta_j^l(\mathbf{r})e^{\frac{2\pi}{a_i}(i\mathbf{q}_{l,j}\cdot\mathbf{r})} + c.c. \tag{3.21}$$

$n_o(\mathbf{r})$ is the dimensionless average density of the system, a conserved quantity which is slowly varying spatially with respect to $\mathbf{q}_{l,j}$, the subscript i denotes a particular solid phase, i.e., $i = tri$ represents a triangular phase with lattice spacing a_{tri}, l is the index over the included modes of the i-phase, $\eta_j^l(\mathbf{r})$ are dimensionless spatially varying complex amplitudes which like the average density are slowing varying on atomic scales. l enumerates the mode of the expansion and j is the index over the collection of reciprocal lattice vectors corresponding to mode l. Accordingly, $\mathbf{q}_{l,j}$ represents the lowest set of reciprocal basis vectors necessary to describe the crystal structure of interest and $c.c.$ denotes the complex conjugate. The result is then *coarse-grained* using the volume averaging method of Refs. [61, 62].[Coarse-graining involves separating the scales between the atomically varying phase factors in Eq. (3.21) from the amplitudes and average density, which vary on long wavelengths.] This is followed by a procedure to integrate out the atomic scale effects, leaving behind a model defined solely in terms of the long wavelength variables, i.e., complex amplitudes

and average density. This is also described as the phase-field limit of a phase-field-crystal model[*].

3.4.1   Standard Binary PFC model

For a crystal of triangular symmetry in 2D, coarse-graining E_{pfc} gives, to lowest order in amplitudes, average density and ballistic terms;

$$
\begin{aligned}
\tilde{E}_{pfc} = \int d\mathbf{r} \Bigg\{ & \sum_{j=1}^{3} \left(\Delta B_0 + \gamma \hat{g}(|\mathbf{q}_j|, \mathcal{R}) + 3\nu n_o^2 - 2t n_o \right) |A_j|^2 \\
& + \sum_{j=1}^{3} \left[B_0^x |\mathcal{G}_j A_j|^2 + \frac{3\nu}{2} |A_j|^4 \right] + (6\nu n_o - 2t) \left(\prod_{j=1}^{3} A_j + \text{c.c.} \right) + 6\nu \sum_{j,k>j}^{3} |A_j|^2 |A_k|^2 \\
& + \left(\omega + 2B_2^\ell \sum_{j=1}^{3} |A_j|^2 \right) \frac{\psi^2}{2} + \frac{u}{4} \psi^4 + \frac{K}{2} |\vec{\nabla}\psi|^2 + \gamma \frac{\psi}{2} \int d\mathbf{r}' g(\mathbf{r}-\mathbf{r}')\psi(\mathbf{r}') \\
& + \left(\frac{\Delta B_0 + B_0^x}{2} + \frac{B_2^\ell \psi^2}{4} \right) n_o^2 - \frac{t}{3} n_o^3 + \frac{\nu}{4} n_o^4 + \gamma \frac{n_o}{2} \int d\mathbf{r}' \, g(\mathbf{r}-\mathbf{r}') n_o(\mathbf{r}') \Bigg\}, \quad (3.22)
\end{aligned}
$$

where $\Delta B_0 = B_0^\ell - B_0^x$ defines a temperature scale, the caret denotes the Fourier transform, with $\hat{g} = \mathcal{R}^2/(1 + |\mathbf{q}_j|^2 \mathcal{R}^2)$, $\mathcal{G}_j \equiv \nabla^2 + 2i\mathbf{q}_j \cdot \nabla$ and we have defined $A_j \equiv \eta_j^1$ for the single-mode triangular structure. The free energy functional of Eq. (3.22) describes a system with multiple crystal orientations, elasto-plastic effects through the complex nature of the amplitudes, as well as density changes through the field n_o. Moreover, as a coarse-grained model, it operates on scales much larger than the lattice constant of the solid. A noteworthy result of Eq. (3.22) is that the $\gamma \hat{g}(|\mathbf{q}_j|, \mathcal{R})$ term competes with the temperature (ΔB_0), as both are modulated by the magnitude of the amplitude squared, $|A_j|^2$. In other words forced external driving is manifested, partly, as a shift in the temperature scale leading to a new effective temperature. This is in agreement with previous theories of phase equilibria under driven conditions [85, 74]. Furthermore, the ballistic term in concentration, $\gamma \frac{\psi}{2} \int d\mathbf{r}' g(\mathbf{r} - \mathbf{r}')\psi(\mathbf{r}')$, will be shown to renormalize the coefficient of the ψ^2 in the Cahn-Hilliard portion of the energy in the thermodynamic limit, i.e., limit $\mathcal{R} \to \infty$. Namely, the model also predicts that ballistic effects cause alterations in the critical transition temperature as well. We also note that in the absence of density variations, defects and the elasto-plastic effects inherent in the complex nature of the amplitude formulation, i.e., all $|A_j| = \text{const.}$ and scale out of the problem, we recover the Cahn-Hilliard ballistic model of Enrique and Bellon [1]. The repercussions of these effects are explored below where we construct phase diagrams for this model.

Phase Diagram - Pure Material

The equilibrium phase diagram for a pure material follows standard minimization procedures analogous to Refs. [16, 18]. For a pure material, we assume a real and constant amplitude $A_j \equiv \varphi$ for all j and a constant wave vector, to describe the periodicity of the solid, ignore all terms in ψ and set $t = 0$ and $\nu = 1$. Making a long wavelength approximation, i.e., $q\mathcal{R} \gg 1$[†], we first begin by minimizing the energy for the equilibrium wave vector, $q_{\text{eq}} = |\mathbf{q}_j|$, which is substituted back into the energy. Next, the energy is minimized for the real amplitude φ. After substitution of the

---

[*]For the XPFC model particularly, part of the aim of this thesis is to derive its long wavelength form for the first time. The salient features of this derivation can be found in Chapter 7, while details on coarse-graining can be found in Appendix C. In this chapter, only the results of coarse-graining will be shown and the properties of the resulting models investigated.

[†]This means that the average distribution distance, $\mathcal{R}$, of atomic exchanges is relatively infinite compared to the atomic periodicity, q, of the underlying crystalline lattice.

minimized amplitude back into the energy, we have a resulting energy which is a function of the conserved quantity n_o, temperature (ΔB_0), and the reduced forcing frequency γ. A common tangent or the equivalent Maxwell equal area construction leads to Fig. 3.3, which plots a kinetic phase diagram in ΔB_0, n_o and γ space. We notice a trend of decreasing solid-liquid transition temperature with increasing γ. As previously discussed, we can attribute this behaviour to the competition between the temperature and ballistic term, where in the thermodynamic, constant amplitude limit, the competition term takes the form of $(\Delta B_0 + \gamma/q)\varphi^2$.
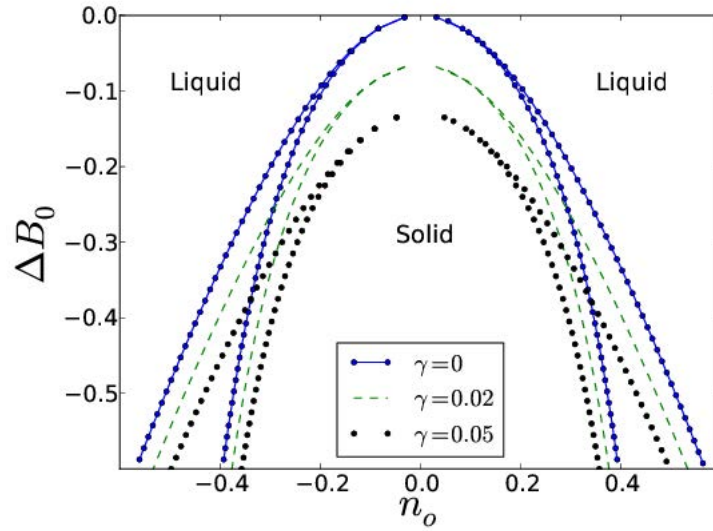
Figure 3.3: Kinetic phase diagram for a pure material exhibiting density variations in $\Delta B_0, n_o, \gamma$ space, shown here projected onto the $\Delta B_0, n_o$ space for choice values of the reduced forcing frequency γ. Phase diagram plots the dimensionless temperature (ΔB_0) versus dimensionless average number density (n_o). Squares with lines (blue) represent the standard PFC model, $\gamma = 0$, dashed lines (green) correspond to a ballistic case of $\gamma = 0.02$, while squares (black) correspond to a ballistic case of $\gamma = 0.05$.

Moving on to the binary alloy, we again assume real and constant amplitude $A_j \equiv \varphi$ for all j and a constant wave vector, q, to describe the periodicity of the solid. We set $B_2^\ell = -1.8$, $B_0^x = 1$, $t = 0.6$, $\nu = 1$, $u = 4$ and $n_o = 0$. A spinodal and a eutectic alloy are differentiated, in this PFC model, by choice of the parameter ω. After the parameters are set, we follow the same minimization steps as outlined for the pure material in the preceding section with respect to φ and q_{eq}. With the average density set to zero, the resulting minimized energy is a only a function of ψ, temperature (ΔB_0), reduced forcing frequency γ and ballistic distance $\mathcal{R}$. A common tangent construction or equivalent Maxwell equal area construction gives Fig. 3.4. In Fig. 3.4, we present the phase diagram of a eutectic alloy under ballistic effects in ΔB_0, ψ and γ phase space. In the figure, $a = 2\pi/q_{eq}$ is the lattice spacing associated with the triangular unit cell in 2D. There are several things to note. There is still a general shift of the solid-liquid transition temperature, additionally however, in Fig. 3.4 we also witness the alteration of the eutectic alloy into a spinodal alloy. Again, in the thermodynamic limit the coefficient of the amplitude square term becomes $(\Delta B_0 + \gamma/q)\varphi^2$, which from the pure material calculation above, was shown to affect the solid-liquid transition. This term is what primarily leads to the general shift in the solid-liquid transition. However, for the binary alloy, the coefficient multiplying the ψ^2 in the Cahn-Hilliard contribution becomes $\left(\omega + 12B_2^\ell\varphi^2 + \gamma\mathcal{R}^2\right)\psi^2$. The $\gamma\mathcal{R}^2$ (i.e. $q\mathcal{R} \gg 1$) contribution to this term

simultaneously accounts for the change from eutectic to spinodal, the ever increasing range of the solid solution region in both alloys, and contributes to the change in the solid-liquid transition lines in our model as well.

Phase Diagram - Eutectic Binary Alloy
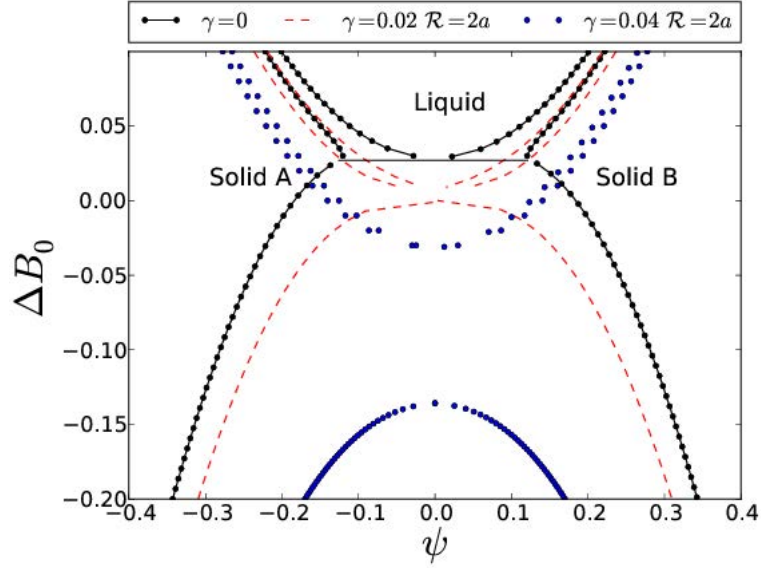
Figure 3.4: Binary eutectic, i.e., $\omega = 0.008$, phase diagrams under forced ballistic driving. The kinetic phase diagrams, here projected onto the $\Delta B_0, \psi$ phase space, plots the dimensionless temperature (ΔB_0) versus dimensionless concentration (ψ). Circles and lines (black) represent the standard binary PFC model, $\gamma = 0$, dashed lines (red) correspond to a ballistic case of $\gamma = 0.02$ and $\mathcal{R} = 2a$, while circles (blue) correspond to a ballistic case of $\gamma = 0.04$ and $\mathcal{R} = 2a$ with a being the lattice spacing [29].

3.4.2 XPFC model

For a system which supports both triangular and square crystal structures in 2D, coarse-graining E_{xpfc} gives, to lowest order in amplitudes, average density and ballistic terms;

$$\tilde{E}_{xpfc} =$$

$$\int d\mathbf{r} \Bigg\{ \frac{n_o^2}{2} - \eta \frac{n_o^3}{6} + \chi \frac{n_o^4}{12} - \frac{n_o}{2} \left[\left(\hat{\xi}_V(\mathbf{q}) \hat{C}_2(\mathbf{q}) - \gamma \hat{g} \right) \hat{n}_o(\mathbf{q}) \right]_{\mathbf{r}}$$

$$+ (1 - \eta n_o + \chi n_o^2) \left(\sum_j^4 |A_j|^2 + \sum_m^2 |B_m|^2 \right) - (\eta - 2\chi n_o) \left[A_1 A_2 A_3 + A_1^* A_4^* B_2^* + A_1 A_4^* B_1^* + \text{c.c} \right]$$

$$+ \frac{\chi}{2} \left[\sum_j^4 A_j^2 (A_j^*)^2 + \sum_m^2 B_m^2 (B_m^*)^2 + 4 \left(\sum_j^4 \sum_{m>j}^4 |A_j|^2 |A_m|^2 + \sum_j^4 \sum_m^2 |A_j|^2 |B_m|^2 + |B_1|^2 |B_2|^2 \right) \right]$$

$$+ \chi \left[2 A_2^* A_3^* A_4^* B_1^* + 2 A_2 A_3 A_4^* B_2^* + A_1^2 B_1^* B_2 + A_4^2 B_1 B_2 + \text{c.c} \right]$$

$$- \frac{1}{2} \sum_j^4 A_j^* \left[\hat{C}_{\text{eff}}^{\text{bal}}(|\mathbf{q} + \mathbf{q}_j|) \hat{A}_j(\mathbf{q}) \right]_{\mathbf{r}} - \frac{1}{2} \sum_j^4 A_j \left[\hat{C}_{\text{eff}}^{\text{bal}}(|\mathbf{q} - \mathbf{q}_j|) \hat{A}_j(-\mathbf{q}) \right]_{\mathbf{r}}$$

$$\left. - \frac{1}{2} \sum_m^2 B_m^* \left[\hat{C}_{\text{eff}}^{\text{bal}}(|\mathbf{q} + \mathbf{q}_m|) \hat{B}_m(\mathbf{q}) \right]_{\mathbf{r}} - \frac{1}{2} \sum_m^2 B_m \left[\hat{C}_{\text{eff}}^{\text{bal}}(|\mathbf{q} - \mathbf{q}_m|) \hat{B}_m(-\mathbf{q}) \right]_{\mathbf{r}} \right\}. \qquad (3.23)$$

where the caret denotes the Fourier transform, $\hat{C}_{\text{eff}}^{\text{bal}} = \hat{C}_2 - \gamma \hat{g}$ is the effective two-point ballistic-correlation function, with $\hat{g} = \mathcal{R}^2 / (1 + |\mathbf{q}_{j,m}|^2 \mathcal{R}^2)$, $\hat{C}_2$ the XPFC spectral two-point correlation function and $[\ ]_{\mathbf{r}}$ denoting the inverse Fourier transform. We have defined $A_j \equiv \eta_j^1$ for the first mode and $B_m \equiv \eta_j^2$ for the second mode of our structures. [**Details of the derivation of Eq. (3.23) can be deduced from the derivation found in Chapter 7, where the XPFC complex amplitude model is derived.**] The free energy functional of Eq. (3.23) not only describes a system with multiple crystal orientations, elasto-plastic effects through the complex nature of the amplitudes, density changes through the field n_o, but also multiple crystal structures through the XPFC direct two-point correlation function. For a 2D system, this free energy will describe both square and triangular crystal symmetries. Further, like the coarse-grained model of the standard PFC model, it operates on scales much larger than the lattice constant of either of the crystalline solids produced with the corresponding XPFC model. An interesting and worthwhile result of Eq. (3.23) is the coupling between the direct two-point correlation kernel of the original XPFC model and the ballistic kernel. Being of opposite sign, there will be an obvious competition between the two kernels, as the XPFC correlation kernel attempts to drive the system to the equilibrium structures, while the ballistic kernel competes with this at a rate proportional to the reduced frequency, γ. This competition will be manifested, partly, as shifts in the temperature scale leading to a new effective temperature, however and perhaps more importantly is that it will also be manifested in the average density dimension allowing for preferred long-time equilibrium structures under ballistic driving. This phenomena cannot be predicted/shown with standard approaches. These effects are explored next in constructing a phase diagram for this model.

Phase Diagram - Pure Material

Considering 2D structures of square and triangular symmetry, we produce the phase diagram of Fig. 3.5 under ballistic conditions. The phase diagram, has as input a correlation kernel of a square crystal lattice. We choose as input parameters to the kernerl[‡], $q_{10} = 2\pi$ and $q_{11} = 2\pi\sqrt{2}$ and set, $\rho_{10} = 1$, $\beta_{10} = 1$, $\alpha_{10} = 1$ and $\rho_{11} = 4$, $\beta_{11} = 4$, $\alpha_{11} = 1$. We define real and constant amplitudes, $A_j \equiv \varphi_1$ and $B_m \equiv \varphi_2$, for the first and second modes, for all j and m respectively. We minimize for the amplitudes, which are then inserted back into the free energy. The free energy then becomes a function of only the average density, n_o, temperature, σ and the reduced forcing frequency, γ. A common tangent construction or equivalent Maxwell equal area construction gives Fig. 3.5. Figure 3.5 plots the phase diagram of a pure material under ballistic conditions, given the propensity for the material to have stable multiple crystal structures in equilibrium. This phase diagram, like those that have preceded it, also displays a general temperature shift of the system. However, a noteworthy consequence of the XPFC paradigm is that this effective functional can be used to steady the possible precipitation of out of equilibrium phases in NC materials due to forced external driving. A phenomena not considered in this dissertation, but one that warrants investigation.

In the dynamics section to follow, we return to the standard pure PFC model to study grain growth under ballistic effects.

[‡]The reader is referred to Section 2.2.5 for details as to how one builds an XPFC correlation kernel.
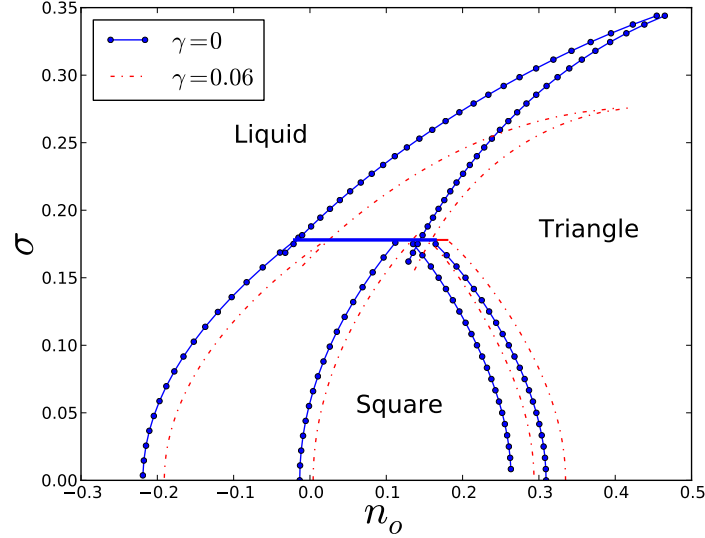
Figure 3.5: Pure material XPFC model phase diagram under forced ballistic mixing. The kinetic phase diagrams are shown here projected onto the σ, n_o phase space, plots the dimensionless temperature (σ) versus dimensionless average density (n_o). Circles and lines (blue) represent the XPFC model, with $\gamma = 0$ and dashed-dotted lines (red) correspond to a ballistic case of $\gamma = 0.06$ and $\mathcal{R} = 1a$, with a being the lattice spacing.

3.5   Applications to Grain Growth Dynamics

We present two sets of numerical simulations conducted to study the role of ballistic driving on the grain growth of a pure nanocrystalline material. The first is designed to illustrate the physics of the proposed effective ballistic PFC energy functionals, using the standard PFC model as an example. The second set of simulations examines the grain growth behaviour of a NC polycrystalline sample under ballistic conditions. For the simulations, we solve Eq. (3.11), with $\Delta x = 0.785$, $\Delta t = 1$, $M = 1$, $\Delta B_0 = -0.26$, $n_o = 0.285$ and $\zeta \neq 0$ (with amplitude $A_\zeta = 0.01$), using a semi-implicit Fourier technique[§].

3.5.1   Coarsening of a 3-Sided Grain

For the first set of simulations, we have 4 grains as shown in the inset of Fig. 3.6 as an initial structure. In this configuration, conventional theory states that grains "1", "2" and "3" will tend to grow at the expense of grain "4", driven by gradients in the chemical potential resulting from curvature effects. Simulations were performed for the regular PFC dynamics ($\gamma = 0$), for the proposed ballistic PFC model at $\gamma = 0.01$ and for several values of the ballistic distance, i.e. $\mathcal{R} = 1a, 5a, 10a, 50a$ and $200a$. For a particular measure of the coarsening rate, we focus on the behaviour of grain "4". Results were averaged over several runs, where grains "1", "2" and "3" assumed different orientations while keeping grain "4" fixed. In Fig. 3.6, we plot the average intensity of the Bragg peaks obtained from the power spectrum for grain "4" (which is proportional to its area) versus time. Several interesting aspects of the plot are noteworthy. First, the rate of coarsening is enhanced for all cases of ballistic mixing. However there exists two regimes of noteworthy behaviour. Namely, we

---

[§]The semi-implicit Fourier technique used to carry out numerical simulations here and in the rest of this thesis is described in Appendix A.

find one regime wherein the $\mathcal{R} = 5a$ and $10a$ conditions cluster and another for the $\mathcal{R} = 1a, 50a$ and $200a$ conditions. In the first regime we have the fastest coarsening rates.

The results of Fig. 3.6 can be understood as follows. The long-time ballistic effect acts over a length scale $\mathcal{R}$ and within this spatial extent the mobility and/or driving force is enhanced. Thus, when $\mathcal{R}$ becomes comparable to the size of grain "4", the coarsening rate is more pronounced as seen in the $\mathcal{R} = 5a$ and $10a$ cases. The plateaus evident at late time for these two conditions are a result of the background signal of the spectrum after the disappearance of grain "4" from the system. When the ballistic distance is much larger than the size of grain "4", i.e., $\mathcal{R} = 50a$ and $200a$ in the second regime, there is equal enhancement in the competition from all grains for growth (although still enhanced compared to the $\gamma = 0$ case). This results in a deadlock, which does not allow for preferential growth. Concerning the $\mathcal{R} = 1a$, the spatial extent of this ballistic event is not large enough to impact any relevant length scales necessary for pronounced preferential growth. However having influence on all interatomic length scales in the system, particularly those associated with boundary widths, it effectively behaves like the larger ballistic distances.
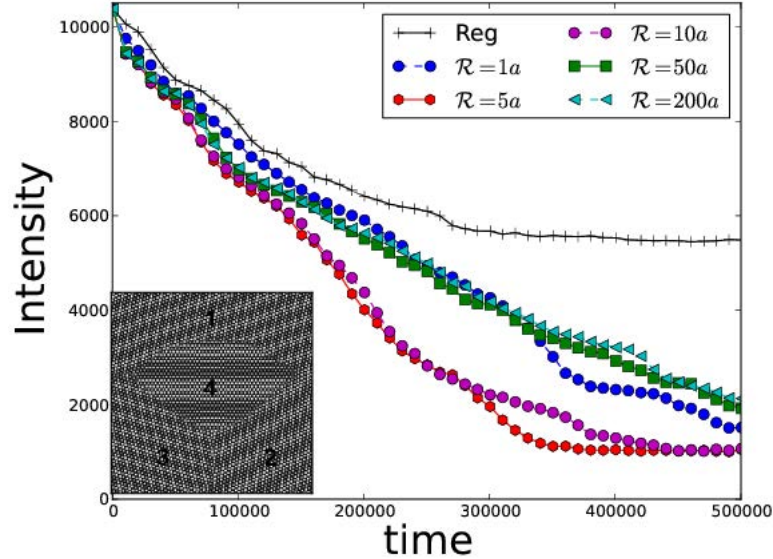
Figure 3.6: Grain intensity versus dimensionless time for a $512\Delta x \times 512\Delta x$, with $\gamma = 0.01$ for varying $\mathcal{R}$. Left bottom inset shows an example of the initial microstructure used to perform the simulations. Density (n) map is shown, where lighter regions represent areas with a higher probability [29].

3.5.2 Grain Growth

The second set of simulations examines grain growth for a nanocrystalline sample in a $1024\Delta x \times 1024\Delta x$ system, with approximately 100 grains. Figure 3.7 plots the average grain size versus time, for $\gamma = 0.05$ for varying ballistic distances $\mathcal{R}$. Grain growth was quantified by Fourier analysis, where the full width at half maximum of the Bragg peak was measured in the radially averaged signal. The multi-grain simulations are consistent with the results of Fig. 3.6. Grain growth is enhanced for all $\mathcal{R}$ values. Also note, in the time range of $500 - 1000$, the average grain size is $\sim 75a$, and the growth is enhanced most strongly for $\mathcal{R}$ comparable to this grain size ($\mathcal{R} = 100a$). Therefore, our results demonstrate that nanocrystalline materials, although possibly offering increased resistance when exposed to ballistic driving forces, such as that from irradiation damage,

are susceptible to enhanced grain growth under such driving forces, with the rate of growth generally increasing with increasing ballistic energy (i.e. $\mathcal{R}$), and particularly enhanced when $\mathcal{R}$ is comparable to the grain size.
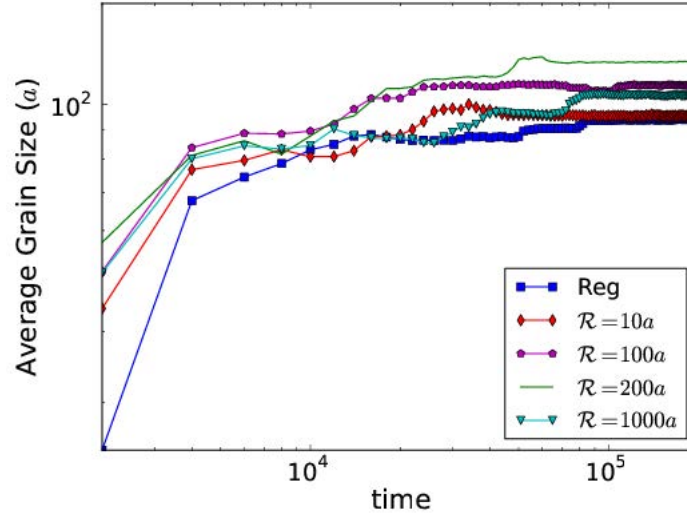
Figure 3.7: Grain growth results plotting average grain size versus time, on a log-log scale, for a $1024\Delta x \times 1024\Delta x$. The grain size is a dimensionless quantity, measured in units of the lattice spacing, plotted against dimensionless time. Here $\gamma = 0.05$ for $\mathcal{R} = 10a, 100a, 200a$ and $\mathcal{R} = 1000a$ [29].

3.6   Summary and Conclusions

In this chapter we have developed an atomistic continuum model of competing effects between thermally activated diffusional processes and those driven by externally imposed ballistic events in both pure materials and alloys using the standard PFC and XPFC free energy functionals. Extending the model of Enrique and Bellon, the approach we have taken is capable of describing defect microstructure, multiple crystal structures and orientations, and elasto-plastic effects.

A long wavelength analysis of the proposed models predicts that ballistic events change the phase diagram through a shift in the solid-liquid transition temperatures for a pure material for the standard PFC, while for the XPFC model, it also leads to alterations of the preferred crystal structures in equilibrium as a function of the driving condition. For a eutectic alloy, the model further predicts an alteration of equilibrium through shifts in the critical transition temperature in the solid solution region, an effect which has long been conjectured in the external driving and irradiation damage literature.

The kinetic properties of the model, under ballistic driving, showed that grain growth is enhanced with increasing average ballistic distance, with preferential enhancement for grain sizes comparable to the ballistic mixing range $\mathcal{R}$. Further numerical and experimental investigation would be instructive to elucidate the possible myriad of behavioural aspects in nanocrystalline system when subjected to ballistic driving. One such aspect worth investigation is the nucleation/precipitation of out of equilibrium phases as a function of the forcing conditions. With the ability of the XPFC model to stabilize multiple crystal structures, it would be fruitful to investigate such a phenomena using the model presented in this chapter.

In the following chapter we turn our attention to extending the XPFC formalism to multi-component alloys. We will emphasize the steps of how to non-trivially extend this paradigm to such systems while still maintaining the features of the formalism that make it efficient for numerical modeling. Once derived, the chapters to follow will reduce the model to binary and ternary systems where they will be applied to the study of solute clustering in Al-Cu systems.

Chapter 4

Structural Transformations in Multi-Component Alloys Using Phase-Field-Crystal Models

In the preceding chapter, we explored nanocrystalline systems under driven conditions using both the standard PFC method and the new XPFC method, where numerical results were presented for grain growth using the standard PFC model. We showed the robustness of the method, generally, in addressing phenomena where atomic scale effects and properties are important. The XPFC method, with its ability to easily model multiple crystal structures, clearly represents the natural direction which the PFC method should follow. Here we present an extension of the XPFC method to multi-component systems, a non-trivial task. After developing the model in this chapter, Chapters 5 and 6 consider binary and ternary extensions of the method, where general equilibrium properties and dynamic illustrations are demonstrated, followed by applications to clustering in Al alloys.

4.1   Motivation

Engineering alloys require the additions of multiple components in order to achieve desired properties. The addition of multiple components also makes available to the alloy, a plethora of possible phases from which the alloy can choose given the specific amounts of the components added. This, inevitably, makes the investigation of their microstructure evolution and defect interactions difficult. In the case of binary alloys, models of solidification processes such as nucleation, free growth and coarsening kinetics, segregation and second phase formation have been relatively well developed. However, for multi-component alloys, the complex interactions involved between the different chemical species, interplay between multiple phases, dislocations and other defects make such phenomena far more difficult to study, even with advances in characterization techniques such as conventional and high resolution transmission electron microscopy.

The current state in treating such systems is via the phenomenological phase-field approach. While the multiple component nature of complex alloys may be well captured by PF approaches, their multi-phase nature cannot, as PF methods represent a particular phase via scalar, uniform order-parameters. In doing so, the atomistic features such as defects, grain boundaries and orientations are often dealt with in a somewhat ad-hoc way that resort to the introduction of effective parameters or auxiliary fields.

In this chapter, we generalize the XPFC formalism of Greenwood *et. al* [19, 20] to the case of N-component alloys. The approach begins with the truncated CDFT energy functional of an N-component system. At the core of our excess free energy are the particle interactions of Refs. [19,

20], adapted for different structural phases in alloys by making the interaction kernel a function of the local species concentrations. We derive the full XPFC multi-component free energy functional, after which the model is simplified for convenience.

The chapter is organized as follows. In Section 4.2, a general free energy functional for an N-component alloy is derived starting from the classical density functional theory of freezing energy formalism of Ramakrishnan and Yussouff [22], where each alloy component is written in terms of a density field, ρ_i. The model is re-written in terms of total density and concentration variables to make contact with standard models used in the description of alloys. The model is then collapsed to a simplified form of the free energy in Section 4.3. We review the construction of correlation functions for the XPFC models in Sections 4.4, followed by describing the equations of motion for the total density and each concentration field in Section 4.5. Finally, we end with a summary and conclusions.

4.2 Deriving an XPFC Energy Functional for N-component Systems

The free energy functional of an N-component mixture can be described by two contributions; a local free energy for each of the N density fields and an excess free energy due to species interactions. The local free energy is treated as an ideal energy which drives the density fields to become uniform. The excess contribution drives the density fields to become periodic by creating minima in the free energy for these states. We can write the free energy functional of the mixture as

$$\frac{\Delta \mathcal{F}}{k_B T} = \int d\mathbf{r} \left\{ \frac{\Delta F_{id}}{k_B T} + \frac{\Delta F_{exc}}{k_B T} \right\}, \tag{4.1}$$

where ΔF_{id} denotes the ideal energy and ΔF_{exc} is the excess energy which accounts for interactions between atoms through correlative interactions. This latter term, gives rise to structural symmetry, elasticity and interactions between topological defects. The constant k_B is the Boltzmann constant and T the temperature.

The ideal energy, ΔF_{id}, gives the entropic contribution for an N-component system. For small density changes from a reference density of each component, it is defined as

$$\frac{\Delta F_{id}}{k_B T} = \sum_i^N \rho_i \ln \left(\frac{\rho_i}{\rho_i^\ell} \right) - \delta \rho_i, \tag{4.2}$$

where N denotes the number of components, which are denoted as $A, B, C, \ldots$, etc., ρ_i is the density of component i, and ρ_i^ℓ is a reference density of component i in the liquid phase at co-existence. Following previous PFC models [18], we define a total atomic number density, $\rho = \sum_i^N \rho_i$, and the total reference number density as $\rho^\ell = \sum_i^N \rho_i^\ell$. Following Refs. [18, 62], we define concentrations as $c_i = \rho_i/\rho$ and the corresponding reference compositions by $c_i^\ell = \rho_i^\ell/\rho^\ell$. Furthermore, for convenience we define a dimensionless atomic number density of the form $n = \rho/\rho^\ell - 1$. With these definitions and the conservation condition, $\sum_i c_i \equiv 1$, Eq. (4.2) simplifies to the dimensionless form

$$\frac{\Delta F_{id}}{k_B T \rho^\ell} = (n+1) \ln (n+1) - n + (n+1) \sum_i^N c_i \ln \frac{c_i}{c_i^\ell}. \tag{4.3}$$

The excess energy takes into account inter-particle interactions truncated at two-particle, i.e.,

A-A,B-B,..., N-N, A-B,...,A-N, $\cdots$ interactions. This can be defined as,

$$\frac{\Delta F_{exc}}{k_B T} = -\frac{1}{2} \int d\mathbf{r}' \sum_i^N \sum_j^N \delta\rho_i(\mathbf{r}) \, C_2^{ij}(\mathbf{r}, \mathbf{r}') \, \delta\rho_j(\mathbf{r}'), \tag{4.4}$$

where C_2^{ij} represent all combinations of two-particle correlations, assumed isotropic (i.e., $C_2^{ij}(\mathbf{r}, \mathbf{r}') = C_2^{ij}(|\mathbf{r} - \mathbf{r}'|)$), between the field describing species i and j, respectively, where $i, j = A, B, C, \ldots, N$. We write Eq. (4.4) in terms of the reduced density, n, and compositions, c_i. As in Refs. [18, 2], we consider only the lowest order contributions of the compositions c_i, which vary on length scales much larger than the density n, which are periodic on the scale of the lattice constant. This allows us to simplify integrals arising from Eq. (4.4), which couple $c_i(\mathbf{r}')$ together with $n(\mathbf{r}')^*$. For example,

$$\int d\mathbf{r}' \, C_2^{ij}(|\mathbf{r} - \mathbf{r}'|) n(\mathbf{r}') c_i(\mathbf{r}') \approx c_i(\mathbf{r}) \int d\mathbf{r}' C_2^{ij}(|\mathbf{r} - \mathbf{r}'|) n(\mathbf{r}').$$

To simplify notation, the notation $n(\mathbf{r}') \equiv n'$ and $c_i(\mathbf{r}') \equiv c_i'$ is used hereafter. With these simplifications and notations, the excess energy of Eq. (4.4) can be written in terms of the dimensionless variables n and $\{c_i\}$ as

$$\begin{aligned}
\frac{\Delta F_{ex}}{k_B T \rho^\ell} = &-\frac{1}{2} \sum_{i,j}^N \int d\mathbf{r} \left[n \, c_i \, c_j + c_i \, c_j - c_i^\ell \, c_j \right] \int d\mathbf{r}' \, C_2^{ij} \, n' \\
&-\frac{1}{2} \sum_{i,j}^N \int d\mathbf{r} \left[n \, c_i + c_i - c_i^o \right] \int d\mathbf{r}' \, C_2^{ij} \, c_j' \\
&-\frac{1}{2} \sum_{i,j}^N \int d\mathbf{r} \left[c_i^\ell \, c_j^\ell - n \, c_j^\ell \, c_i - c_j^\ell \, c_i \right] \hat{C}_2^{ij}(|\mathbf{k}|=0),
\end{aligned} \tag{4.5}$$

where $\hat{C}_2^{ij}$ is the Fourier transform of $C_2^{ij}(|\mathbf{r} - \mathbf{r}'|)$, and satisfies

$$\hat{C}_2^{ij}(|\mathbf{k}|=0) = \int d\mathbf{r}' \, C_2^{ij}(|\mathbf{r} - \mathbf{r}'|), \tag{4.6}$$

and where we have introduced the notation $C_2^{ij} \equiv \rho^\ell C_2^{ij}(|\mathbf{r} - \mathbf{r}'|)$, which is the direct two-point correlation function at the reference density, ρ^ℓ.

Collecting terms from Eqs. (4.3) and (4.5) gives the complete N-component free energy functional, written in dimensionless form,

$$\begin{aligned}
\frac{\Delta \mathcal{F}}{k_B T \rho^\ell} = &\int d\mathbf{r} \, (n+1) \ln(n+1) - n + F_{\text{mix}}(\{c_i\})(n+1) \\
&-\frac{1}{2} \sum_{i,j}^N \int d\mathbf{r} \left[n \, c_i \, c_j + c_i \, c_j - c_i^\ell \, c_j \right] \int d\mathbf{r}' \, C_2^{ij} \, n' \\
&-\frac{1}{2} \sum_{i,j}^N \int d\mathbf{r} \left[n \, c_i + c_i - c_i^\ell \right] \int d\mathbf{r}' \, C_2^{ij} \, c_j'
\end{aligned} \tag{4.7}$$

---

*This approximation captures the separation of scales between concentration and density adequately in direct PFC simulations. However, it is not suitable when coarse-graining the model to derive corresponding complex amplitude equations. In the latter case, a treatment may be to expand "slow" fields to at least second order Taylor series in powers of $(\mathbf{r} - \mathbf{r}')$.

$$-\frac{1}{2}\sum_{i,j}^{N}\int d\mathbf{r}\,\left[c_i^{\ell}\,c_j^{\ell}-n\,c_i\,c_j^{\ell}-c_j^{\ell}\,c_i\right]\,\hat{C}_2^{ij}(|\mathbf{k}|\!=\!0),$$

where $F_{\text{mix}}(\{c_i\})$ denotes the ideal entropy of mixing,

$$F_{\text{mix}}(\{c_i\}) = \sum_i^{N} c_i \ln \frac{c_i}{c_i^{\ell}}. \tag{4.8}$$

Equation (4.7) is the full N-component PFC model in CDFT form. When a form for C_2^{ij} is specified, it can be used directly. However, this form is not convenient to make contact with other theories and models in the literature. It will be transformed into a simpler form in the next section.

4.3   Simplified N-Component XPFC Free Energy

It is instructive to reduce the model of Eq. (4.7) to a minimal form that retains the salient features of the original model but can also make contact with previous PFC and PF models. To do so, certain simplifications must be made.

First, an expansion of the ideal free energy term is taken to fourth order in the limit of small n, i.e., around the reference ρ^{ℓ}. The logarithms in the entropy of mixing (Eq. (4.8)) are left unexpanded for convenience. Secondly, the terms with correlation kernels can be simplified by retaining the long wavelength behavior of all compositions c_i, where they vary much more slowly than n. Following the procedures outlined in Refs. [61, 62, 89, 67], it can be shown that upon coarse graining, all terms containing linear powers of n or n' in Eq. (4.7) vanish. Also, terms containing only concentration fields and a correlation function give rise to local products of $c_i\,c_j$ (which arise from the $\mathbf{k}=0$ part of C_2^{ij}, and look analogous to the last term in Eq. (4.7)) and products between their corresponding gradients. The reader is referred to Appendix C for details of the coarse graining procedure applied to terms of Eq. (4.7). After some tedious but straightforward algebra, the above approximations lead to the following simplified N-component XPFC free energy functional,

$$\mathcal{F} = \int d\mathbf{r}\,\left\{\frac{n^2}{2} - \eta\frac{n^3}{6} + \chi\frac{n^4}{12} + \omega\,F_{\text{mix}}(\{c_i\})(n+1)\right.$$
$$\left. -\frac{1}{2}n\int d\mathbf{r}'C_{\text{eff}}(|\mathbf{r}-\mathbf{r}'|)\,n' - \frac{1}{2}\sum_{i,j}^{N}\kappa_{ij}\nabla c_i \cdot \nabla c_j\right\}, \tag{4.9}$$

where

$$C_{\text{eff}}(|\mathbf{r}-\mathbf{r}'|) = \sum_{i,j=1}^{N} c_i\,c_j\,C_2^{ij}(|\mathbf{r}-\mathbf{r}'|). \tag{4.10}$$

The parameters η, χ and ω are constants, the significance of which is discussed further below. $\kappa_{ij} = \partial_{(\mathbf{k}^2)}\hat{C}_2^{ij}|_{\mathbf{k}=0}$ are gradient energy coefficients associated with compositional interfaces involving c_i and c_j. For notational convenience, $\mathcal{F}$ is used to denote $\Delta\mathcal{F}/k_BT\rho^{\ell}$.

The parameters η and χ corresponding to Eq. (4.9) are formally equal to one, but hereafter will be treated as free parameters that can be used to correct the density dependence of the ideal free energy away from the reference density ρ^{ℓ}, i.e., to match the bulk free energy to materials properties. Also, it was shown in Ref. [67] that the $\mathbf{k}=0$ mode of higher-order correlation terms in a CDFT expansion will contribute local polynomial terms in c_i and n, analogous to the $\hat{C}_2^{ij}(|\mathbf{k}|=0)$ terms of Eq. (4.7). These terms can be combined with an expansion of the F_{mix} term in Eq. (4.7) to produce a messy polynomial expansion of the local free energy in powers of the elements of $\{c_i\}$ and n.

To keep the form of the free energy compact, we find that it is simpler to introduce a parameter, ω, which modifies the mixing free energy from its ideal form, away from the reference compositions c_i^ℓ.

The correlation function defined by Eq. (4.10) is too basic to capture the properties of very complex alloys –although it can capture some properties of simple alloys. Guided by the form of the first term on the second line of Eq. (4.7), it can be seen that higher-order correlation functions will contribute terms of the form $c_i\, c_j\, c_k\, C_3^{ijk}$, $c_i\, c_j\, c_k\, c_l C_4^{ijkl}$, etc. To emulate such higher-order non-local contributions effectively, we introduce an effective correlation function of the form

$$C_{\text{eff}}(|\mathbf{r} - \mathbf{r}'|) = \sum_{i=1}^{N} X_i(\{c_j\})\, C_2^{ii}(|\mathbf{r} - \mathbf{r}'|). \tag{4.11}$$

The X_i are as yet undetermined polynomial functions of the elements of $\{c_j\}$. The role of the X_i are to determine the resultant local crystalline structure by interpolating between the kernels $\hat{C}_2^{ii}$ (defined below), which define the base equilibrium crystal structures of each pure component i. The interpolation is done through appropriately constructed polynomial expansions of the elements of $\{c_j\}$. The order of X_i depend on the number of components in the system and can be made as high as required to smoothly interpolate from one correlation kernel to another. We find that Eq. (4.11), in Chapters 5 and 6, through appropriate choices of X_i, combined with other model parameters, is robust enough to model a wide variety of alloy systems.

The model of Eq. (4.9) captures the usual features of other PFC models, while allowing for a very easy control of a wide range of crystal structures in different phases. It is motivated from considerations of classical density functional theory but simplified enough to make numerically tractable simulations possible, as will be shown in the following chapters. Finally, we note that the form of the expansion in Eq. (4.11) is dimensionally motivated from higher-order terms in CDFT but is flexible enough to model experimentally relevant multi-component alloys quantitatively using, for example, thermodynamic databases.

4.4 Correlation Functions C_2^{ii}

As discussed previously, the XPFC formalism is best suited for numerical simulation in Fourier space. The pure component correlation functions $C_2^{ii}(|\mathbf{r}-\mathbf{r}'|)$ are thus constructed directly in Fourier space, where they are denoted $\hat{C}_2^{ii}(|\mathbf{k}|)$. Each component, i, contributes a correlation function that supports the desired equilibrium crystal structure for that pure component. Like the pure component work of Greenwood *et al.* [19, 20], discussed in Section 2.2.5, a Fourier space peak of $\hat{C}_2^{ii}(|\mathbf{k}|)$ [20], for a given mode, j, is denoted by

$$\hat{C}_{2j}^{ii} = e^{-\frac{\sigma^2}{\sigma_{Mj}^2}} e^{-\frac{(k-k_j)^2}{2\alpha_j^2}}. \tag{4.12}$$

The total correlation function for component i, $\hat{C}_2^{ii}$, is defined by the *numerical envelope* of all peaks $\hat{C}_{2j}^{ii}$. The first exponential in Eq. (4.12) sets the temperature scale via a Debye-Waller prefactor that employs an effective temperature parameter, σ. We also define an effective transition temperature, σ_{Mj}, which subsumes the effect of planar and atomic densities associated with the family of planes corresponding to mode j [30]. The second exponential sets the position of the reciprocal space peak at k_j, which defines the inverse of the interplanar spacing for the jth family of planes in the equilibrium unit cell structure of component i. Each peak is represented by a Gaussian function, with α_j being the width of the peak, j. The $\{\alpha_j\}$ have been shown [20] to set the elastic and surface energies, as well as their anisotropic properties.

It is noted that the $\mathbf{k} = 0$ mode of all correlation functions is essentially zero. In principle, as

discussed above, the $\mathbf{k} = 0$ mode of these correlation functions can have their effects implicitly reflected through local coefficients in the free energy. As discussed, in the case of a pure material, a nonzero peak height at $\mathbf{k} = 0$ in the correlation function merely shifts the local free energy at densities away from the reference density, however the stability of equilibrium structures is typically unchanged [20]. The situation is similar for alloys, where the $\mathbf{k} = 0$ mode will have a negligible contribution for phases that remain relatively close to the reference density. Deviations of phases away from the reference density will be manifested in the average density dimension of the phase diagram. In what is presented henceforth, it is assumed that the average density $n_o = 0$ to simplify calculations. Of course, the more complex situations where both the concentration and average density need to be modeled can be treated by adding suitable $\mathbf{k} = 0$ contributions, or by choosing the appropriate coefficients in the bulk free energy. Thus, without loss of generality, we will assume no additional constant to the correlation function $\hat{C}_2^{ii}$ here.

4.5 Dynamics

Equations of motion for the density, n, and each of the concentration fields, c_i, follow conserved dissipative dynamics. Namely the dimensionless density n obeys

$$\frac{\partial n}{\partial t} = \nabla \cdot \left(M_n \nabla \frac{\delta \mathcal{F}}{\delta n} \right) + \nabla \cdot \zeta_n \tag{4.13}$$

$$= \nabla \cdot \left(M_n \nabla \left\{ n - \eta \frac{n^2}{2} + \chi \frac{n^3}{3} + \omega F_{\text{mix}}(\{c_i\}) - C_{\text{eff}} \, n \right\} \right) + \nabla \cdot \zeta_n.$$

The dynamics of each composition field, c_i, evolve according to the dissipative response to the general thermodynamic driving force for diffusion in solution thermodynamics [90, 91]. That is,

$$\frac{\partial c_i}{\partial t} = \nabla \cdot \left(\sum_j^N M_{c_i c_j} \nabla \frac{\delta \mathcal{F}}{\delta c_j} \right) + \nabla \cdot \zeta_{c_i} \tag{4.14}$$

$$= \nabla \cdot \left(\sum_j^N M_{c_i c_j} \nabla \left\{ \omega(n+1) \frac{\delta F_{\text{mix}}}{\delta c_j} - \frac{1}{2} n \frac{\delta C_{\text{eff}}}{\delta c_j} \, n + \kappa_{ij} \nabla^2 c_j \right\} \right) + \nabla \cdot \zeta_{c_i},$$

where the following shorthand notations have been made,

$$C_{\text{eff}} \, n \equiv \int d\mathbf{r}' C_{\text{eff}}(|\mathbf{r} - \mathbf{r}'|) n(\mathbf{r}')$$

$$n \frac{\delta C_{\text{eff}}}{\delta c_j} \, n \equiv n(\mathbf{r}) \int d\mathbf{r}' \frac{\delta C_{\text{eff}}(|\mathbf{r} - \mathbf{r}'|)}{\delta c_j} n(\mathbf{r}'). \tag{4.15}$$

The coefficient M_n denotes the mobility of the density and strictly speaking can be a function of the fields. $M_{c_i c_j}$ is the composition mobility tensor and it reads as

$$M_{c_i c_j} = M_{c_i c_i} \left(\delta_{ij} - \frac{M_{c_j c_j}}{\sum_{l=1}^N M_{c_l c_l}} \right), \tag{4.16}$$

where δ_{ij} is the Kronecker-delta function, which satisfies,

$$\delta_{ij} = \begin{cases} 1 & \text{if } i = j \\ 0 & \text{otherwise} \end{cases} \tag{4.17}$$

41

The noise terms, ζ_n and ζ_{c_i}, model coarse-grained thermal fluctuations on density and each concentration field, respectively. They formally satisfy the fluctuation dissipation relation, i.e., $\langle \zeta_\nu(\mathbf{r}, t) \rangle = 0$ and $\langle \zeta_\nu(\mathbf{r}, t)\zeta_\nu(\mathbf{r}', t') \rangle = \Gamma_\nu \delta(\mathbf{r} - \mathbf{r}')\delta(t - t')$, where ν denotes the density or one of the composition fields, with $\Gamma_\nu \propto M_\nu k_B T$. The precise form of Γ_ν, which sets the scale of the thermal fluctuations is not properly understood in the context of PFC modeling but is the object of several investigations [92, 93]. We will neglect these fluctuations in the chapters to follow.

If we assume that the mobility tensor, in Eq. (4.14), is diagonal and symmetric, the equation of motion for each respective concentration field reduces to

$$\frac{\partial c_i}{\partial t} = \nabla \cdot \left(M_{c_i} \nabla \frac{\delta \mathcal{F}}{\delta c_i} \right) + \zeta_{c_i} \tag{4.18}$$

$$= \nabla \cdot \left(M_{c_i} \nabla \left\{ \omega(n+1)\frac{\delta F_{\mathrm{mix}}}{\delta c_i} - \frac{1}{2}n\frac{\delta C_{\mathrm{eff}}}{\delta c_i}n + \kappa_{ii}\nabla^2 c_i \right\} \right) + \nabla \cdot \zeta_{c_i}.$$

We will be discussing results and demonstrations under the aforementioned assumptions regarding the mobility tensor.

4.6   Summary and Conclusions

This chapter introduced a new phase-field-crystal method for structural transformations in multi-component alloys. The salient features of the derivation were presented, along with its simplification to a more tractable form. Dynamics of the multi-component model were also discussed.

This is the first multi-component PFC model, and one which is capable of self-consistently incorporating multiple crystalline phases. As a novel and simple method, it is expected that this model can thus be used to elucidate the role of multiple solutes and phases in phenomena governed by atomic-scale elasticity and defects operating on diffusional time scales.

In Chapter 5, we will take the multi-component model developed here, and reduce it to simple two component systems. We then use it to explore some equilibrium properties and kinetic demonstrations of the model. After that, we apply the model to the study of defect-assisted clustering and nucleation of precipitates in binary Al-Cu alloys.

In Chapter 6, we specialize the model developed in this chapter to the more complex ternary alloying systems. The addition of one extra component, as compared with binary systems, affords some intriguing equilibrium and kinetic properties, which are explored when we study solute clustering in ternary Al-Cu-Mg alloys.

Chapter 5

Specialization of the Multi-Component Model to Binary Systems and Application to Ageing in Binary Alloys

This chapter considers the binary alloy limit of the multi-component model derived in the preceding chapter. Being the simplest of alloys, binary alloying systems present an opportunity for us to explore the validity and capability of our model. After writing the energy functional associated with a binary alloy, we explore its equilibrium properties. The dynamics of the model are then illustrated. Finally we apply the binary model to the study of clustering in model Al-Cu alloys.

5.1 Motivation

Binary alloys being the simplest representation of alloys are widely studied. Often, more complex alloying systems are even represented as binary alloys, since it is far easier to analyze and quantify interactions and mechanisms between such a limited number of components. As such, a multi-component model when reduced to a binary alloy should be well equipped in describing many systems of interest. The added benefit of the atomistic nature of our model and the ability to describe multiple crystal structures, also overcomes the weaknesses of traditional, i.e., phase-field, approaches used in the wide range of models used to describe binary systems.

Solute segregation in the presence of defects, i.e., vacancies, dislocations, grain boundaries, is an interesting and important phenomena. With many precipitation hardening and strengthening mechanisms owing to solute-solute, defect-defect and solute-defect interactions, a fundamental understanding of this process is necessary, even in simple binary alloys. Namely, in Al-Cu systems, solute clustering is the term given to the segregation processes which take place at suitable temperatures in the presence of quenched-in defects, such as dislocations. Clustering in these alloys represents the early stages of a phase transformation process within bulk crystals.

Reducing the multi-component model of the previous chapter to a simple binary model, we are afforded the opportunity to investigate clustering at a fundamental level. A level where all the important interactions and features needed, defect-defect, defect-solute, elasto-plasticity, etc., are readily available. Before investigating clustering, we first interrogate the equilibrium properties of the reduced binary model via phase diagram constructions. Following that, the kinetic properties of the binary model are demonstrated by considering eutectic solidification and solute segregation to

grain boundaries. The model is the then applied to the study of clustering in Al-Cu alloys.

The chapter is organized as follows. Section 5.2 describes the approximations made in arriving at the XPFC binary model, with a discussion on the effective correlation function to follow in Section 5.3. We state the resulting dynamical equations in Section 5.4, following which we discuss the equilibrium properties for a few choice systems, in Section 5.5. Finally some kinetic illustrations of the binary model in Section 5.6. The chapter ends with the application of the XPFC binary model to early stage clustering and precipitation in Section 5.7 and summary and conclusions.

5.2   Simplified XPFC Multi-Component Energy Functional for Binary Alloys

The simplified N-component XPFC model free energy functional, Eq. (4.9), can be reduced to a simple binary system. Regarding the system as having two components, A and B, we then have concentrations c_A and c_B. We use the conservation condition in order to represent the system in terms of one composition, i.e., the solute composition, here chosen in relation to component B for convenience ($c \equiv c_B$), then define $c_A = 1 - c_B$. Analogous definitions follow in regards to the reference compositions c_i^ℓ, where $i = A, B$.

The assumptions of the previous paragraph lead to the following simplified dimensionless binary alloy XPFC free energy functional

$$\mathcal{F}^{\text{bin}} = \int d\mathbf{r} \left\{ \frac{n^2}{2} - \eta \frac{n^3}{6} + \chi \frac{n^4}{12} + (n+1)\omega F_{\text{mix}}^{\text{bin}}(c) - \frac{1}{2} n \int d\mathbf{r}' C_{\text{eff}}^{\text{bin}}(|\mathbf{r} - \mathbf{r}'|) n' + \kappa |\nabla c|^2 \right\},$$
(5.1)

where $n' \equiv n(\mathbf{r}')$. The entropy of mixing for a binary system, $F_{\text{mix}}^{\text{bin}}(c)$, modifies to

$$F_{\text{mix}}^{\text{bin}}(c) = \left\{ c \ln\left(\frac{c}{c^\ell}\right) + (1-c) \ln\left(\frac{1-c}{1-c^\ell}\right) \right\},$$
(5.2)

with c^ℓ being a reference liquid solute composition. Equation (5.1) has the form of a Cahn-Hilliard model (when $F_{\text{mix}}^{\text{bin}}(c)$ is expanded to fourth order) plus a PFC contribution for the total density analogous to that in Greenwood *et al.* [19, 20], Section 2.2.5. The gradient energy coefficient is defined by $\kappa = -\kappa_{AA} - \kappa_{BB} + \kappa_{AB} + \kappa_{BA}$[*] and satisfies the condition $\kappa > 0$. To reiterate, the parameters η, χ, and ω can be used fit the ideal energy away from the reference density ρ^ℓ and entropic energy away from the reference composition c^ℓ.

5.3   Effective Correlation Properties

Having stated the simplified binary alloy model, we turn our attention to the definition of the effective correlation, $C_{\text{eff}}^{\text{bin}}(|\mathbf{r} - \mathbf{r}'|)$, appropriate for binary systems. Strictly speaking, the effective correlation for binary systems is a polynomial interpolation of C_2^{AA}, C_2^{BB}, C_2^{AB} and C_2^{BA}, weighted by the composition field. The correlation functions C_2^{AB} and C_2^{BA} represent, respectively, contributions to the excess free energy for the cases where A atoms are in a crystalline structure preferred by B atoms and B atoms that are in a structure preferred by A atoms. As discussed in Section 4.9, we can approximate these correlation functions by a composition-modulated interpolation between C_2^{AA} and C_2^{BB}. For binary systems, we have

$$C_{\text{eff}}^{\text{bin}}(|\mathbf{r} - \mathbf{r}'|) = X_A(c) C_2^{AA}(|\mathbf{r} - \mathbf{r}'|) + X_B(c) C_2^{BB}(|\mathbf{r} - \mathbf{r}'|)$$
(5.3)

---

[*]Refer to Appendix C for details concerning this gradient coefficient.

where

$$X_A(c) = 1 - 3c^2 + 2c^3$$
$$X_B(c) = 1 - 3(1-c)^2 + 2(1-c)^3 \tag{5.4}$$

are interpolation functions which interpolate between the two correlation functions, weighting each as a function of the local composition.

Finally, the correlation functions, $C_2^{ii}(|\mathbf{k}|)$ for each respective pure component, are constructed to include relevant reciprocal space peaks at positions determined by the equilibrium unit cell for each component. The curvature at the tips of each corresponding Bragg peak is tuned to fit the elastic coefficients, while the heights of the peaks are linked to the temperature, σ. These effects are all crucial in driving structural transformations. Further details concerning the correlation functions can be found in Section 4.4 of the preceding chapter.

5.4   Binary Model Dynamics

For a binary system, the dynamics of the total density and concentration fields obey the usual dissipative dynamics. They are,

$$\frac{\partial n}{\partial t} = \nabla \cdot \left(M_n \nabla \left\{ n - \eta \frac{n^2}{2} + \chi \frac{n^3}{3} + \omega F_{\text{mix}}^{\text{bin}} - C_{\text{eff}}^{\text{bin}} n \right\} \right), \tag{5.5}$$

$$\frac{\partial c}{\partial t} = \nabla \cdot \left(M_c \nabla \left\{ (n+1)\omega \frac{\delta F_{\text{mix}}^{\text{bin}}}{\delta c} - \frac{1}{2} n \frac{\delta C_{\text{eff}}^{\text{bin}}}{\delta c} n - \kappa \nabla^2 c \right\} \right), \tag{5.6}$$

where a similar shorthand notation, like that in Eq. (4.15), has been used. M_n and M_c are the mobility coefficients for the density and concentration field respectively. Note we have neglected the associated noise terms making these equations fully deterministic. Without loss of generality, conserved noise terms maybe added without difficulty.

5.5   Equilibrium Properties

The phase coexistence between the respective phases is determined by a common tangent construction between the free energy curves of bulk phases at the reference density ($n_o = 0$). The common tangent construction satisfies,

$$\mu_c^I = \mu_c^J$$
$$\Omega^I = \Omega^J, \tag{5.7}$$

where the latter can be explicitly written as,

$$f^I - \mu_c^I c^I = f^J - \mu_c^J c^J. \tag{5.8}$$

The superscripts I and J denote any two phases in equilibrium. $\mu_c^I = \partial f^I / \partial c$ is the chemical potential of phase I with respect to the concentration, c, with analogous definitions for μ_c^J. Ω^I and Ω^J are the grand potentials of phases I and J, respectively.

Free energy curves are calculated by considering single mode approximations for structures described by a correlation peak, such as BCC and triangular phases and two mode approximations for structures described by two-peaked correlations, such as FCC and square phases. As stated

previously, periodic phases are approximated, around the reference density (i.e., $n_o = 0$), by

$$n_i(\mathbf{r}) = \sum_j \varphi_j \sum_l \exp\left(\frac{2\pi}{a_i}\mathbf{i}\mathbf{k}_l \cdot \mathbf{r}\right), \tag{5.9}$$

where i denotes a solid phase, with lattice spacing a_i, j is the index over the included modes of the i-phase, φ_j is the real and constant amplitude of mode j, and l is the index over the collection of reciprocal lattice peaks corresponding to mode j. $\mathbf{k}_l$ is the reciprocal lattice vector corresponding to each index l. After insertion of the density approximation into the free energy of Eq. (5.1), the energy is integrated over a unit cell and minimized with respect to the amplitudes φ_j, resulting in a composition dependent free energy. A common tangent is then performed in the resulting solid and liquid phases. More details about this methodology can be found in Appendix B[†].

5.5.1 Eutectic Alloys

First we examine alloys where each component is represented by a correlation kernel, C_2^{ii}, where the structure produced for each element is topologically identical. However, they differ in the absolute position of the peaks, which allows each component to assume different equilibrium lattice spacings. Additionally, through the width of each peak, α_j, different elastic and surface energies can be set for each element. When both elements have square structural symmetry, we get the phase diagram shown in Fig. 5.1, while the inset shows a phase diagram for a triangle-triangle binary system. Both diagrams are asymmetric with clearly defined eutectic points and meta-stable coexistence lines (grey dotted). Below the eutectic transition, in the solid solution portions of the phase diagram, the density field is expected to assume a structure according to that prescribed by the effective correlation function.

Figure 5.2(a) presents phase diagrams where the elements are structurally dissimilar. Element A is chosen to have a correlation function with square symmetry by including two peaks in C_2^{AA}, while element B has a correlation function corresponding to a triangular structure and therefore only contains a single peak in C_2^{BB}. Normalizing the lattice spacing of each phase to be 1, a common tangent construction gives the eutectic phase diagram in Fig. 5.2(a).

The validity of the mode density approximations made in constructing the phase diagram was tested, represented by the circles in Fig. 5.2(a), using the equations of motion described by Eqs. (5.5) and (5.6). Equilibrium square and triangular phases are initially seeded in a narrow channel, at the edge of the simulation domain, at a composition close to the equilibrium composition as predicted by the phase diagram. The liquid phase is set as to preserve the total alloy composition. An example resulting from such a setup is depicted in Fig. 5.2 (left). Solute rejection at the moving interface follows naturally during the growth process, resulting in an increase solute diffusion tail ahead of the interface until the interface eventually comes to rest, as expected in 1D diffusion-limited front growth. Snapshots of profiles of the moving front are shown in Fig. 5.2(b). Once the system equilibrates, over several temperatures (σ), we compare the resulting bulk concentrations to the analytic phase diagram in Fig. 5.2(a). The construction of the phase diagram depends on the ratio of the amplitudes, $\varphi_{11} : \varphi_{10}$, for the two mode square phase. We find that removing the temperature dependence of the ratio of the two amplitudes ($\varphi_{11} : \varphi_{10}$) corresponding to the two square correlation peaks (i.e., using the ratio at $\sigma = 0$ for all temperatures) results in good agreement at low temperatures, but begins to deviate as the temperature increases[‡].

[†]For the case where density variations are considered, Eq. (5.9) can be replaced by $n_i(\mathbf{r}) = n_o^i + \sum_j \varphi_j \sum_l \exp\left(\frac{2\pi}{a_i}\mathbf{i}\mathbf{k}_l \cdot \mathbf{r}\right)$. This would require additional contributions to the common tangent equations described by Eq. (5.7). This is also discussed in Appendix B. For an alternative formalism, see appendix of Ref. [62] derived for binary alloys.

[‡]More details about this approximation can be found in Appendix B.
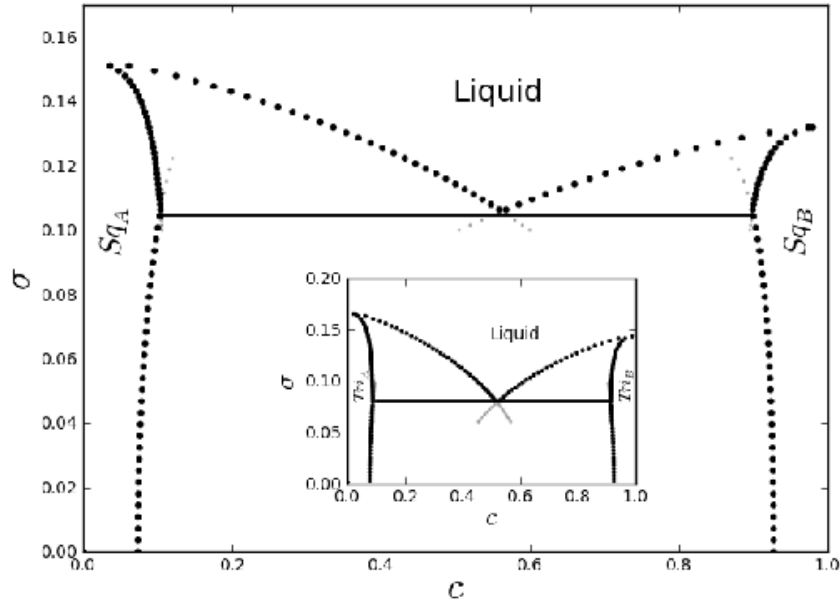
Figure 5.1: Eutectic phase diagram for a square-square system with the inset showing a corresponding eutectic phase diagram of a triangle-triangle alloy. Meta-stability lines are evident by thin grey dots. For both sets of phase diagrams, the ideal parts of the energy have parameters set to; $\eta = 1.4$, $\chi = 1$, while $\omega = 0.02$ and $c_\ell = 0.5$. For the square-square system, the widths of the correlation peaks correspond to $\alpha_{11A} = 0.9$, $\alpha_{10A} = \sqrt{2}\alpha_{11A}$, $\alpha_{11B} = 0.9$ and $\alpha_{10B} = \sqrt{2}\alpha_{11B}$. The peak positions for species A correspond to $k_{11A} = 2\pi$ and $k_{10A} = \sqrt{2}k_{11A}$ and for species B, $k_{11B} = 4\pi/\sqrt{3}$ and $k_{10B} = \sqrt{2}k_{11B}$. For the triangle-triangle system, peak widths are $\alpha_{10A} = 0.8$ and $\alpha_{10B} = 0.8$ and peak positions are $k_{10A} = 2\pi$ and $k_{10B} = 4\pi/\sqrt{3}$ [30].
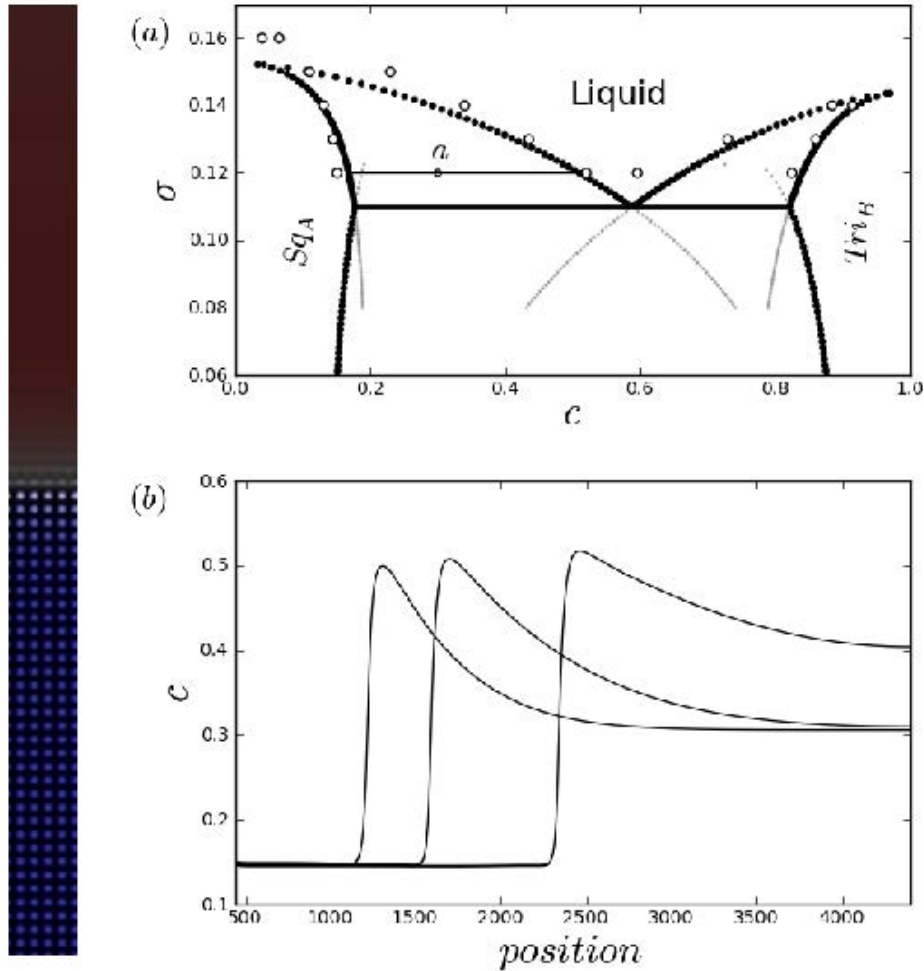
Figure 5.2: Eutectic system for two structurally dissimilar elements. (a) Phase diagram with A having square structural symmetry and B triangular symmetry. Grey dots depict metastable coexistence points and open circles are equilibrated values from dynamic simulations. The parameters for the ideal energy portions of the energy are $\eta = 1.4$, $\chi = 1$, while $\omega = 0.02$ and $c_\ell = 0.5$. The square structure has widths ad peak positions set at $\alpha_{11A} = 1.5$, $\alpha_{10A} = \sqrt{2}\alpha_{11A}$ and $k_{11A} = 2\pi$, $k_{10A} = \sqrt{2}k_{11A}$. The triangular structure has peak width and positions corresponding to $\alpha_{11B} = 1.5$ and $k_{11B} = 4\pi/\sqrt{3}$. (b) Time slices of an evolving compositional profile through a solid-liquid interface corresponding to a quench to point "a" in the phase diagram. A corresponding density-concentration profile of the advancing 1D solid-liquid interface in a channel is shown on the left. The color represents local composition, where blue is saturated at $c = 0.15$ and red is $c = 0.5$ [30].

5.5.2   Peritectic and Isomorphous Alloys

Extending the model for 3D structures, such as those occurring in BCC and FCC transitions, are easily accomplished. We present here a particular construction of a phase diagram for structural transformations that features a peritectic point akin to the Fe-Ni phase diagram. The resulting phase diagram is shown in Fig. 5.3(a), while a simpler isomorphous FCC-liquid, akin to the high temperature Ni-Cu phase diagram, is shown in Fig. 5.3(b). These two classes of phase diagrams are obtained by careful control and tuning of the model parameters, particularly parameters of the correlation functions of each species.

For the initial diagram, Fe-Ni type phase diagram in Fig. 5.3(a), we have two components of similar lattice spacing. Component A, has normalized spacing of 1, and B with a normalized spacing of 1.016. Element A transforms at high temperature (σ) from the liquid phase into the BCC phase. Component B transforms directly from the liquid phase into the FCC phase at a temperature somewhere between the two transition temperatures of component A. At lower temperatures, both A and B transform to the more stable FCC phase. A correlation function containing two peaks, i.e., FCC symmetry, is chosen for both A and B. In order for element A to undergo transitions from liquid to BCC to FCC, the peaks of its correlation should be comparable at low temperatures, while at higher temperature the height of second peak should be negligible compared to the first. The latter effectively leaves behind a one peak correlation,which would produce a BCC phase. On the other hand, element B must maintain the relative heights of the two peaks over the entire range of the stable FCC phase.

A method of designing the desired properties of the correlation described in the previous paragraph is readily available through the Debye-Waller prefactor of each peak. We turn our attention to the effective transition temperature σ_{Mj}^2, which is formally defined by $(2\beta_j\rho_j)/k_j^2$ in Ref. [19, 20]. In allowing it to be a free parameter, each peak now has its own scaling factor, allowing the transition temperature from a liquid to a BCC or from a liquid to an FCC phase to be controlled independently.

To achieve the above requirements for component A, we set the σ_{Mj} parameter for the first peak to be larger than that of the second peak. This will give rise to the necessary transition from a single-peak dominated kernel to a two-peak dominated kernel in the region of stability over the liquid phase. That is, BCC at high temperature, FCC at low temperature. For component B, we set σ_{Mj} to be the same value for both peaks. This allows both peaks to have the same dependence on temperature (σ), leading to a direct transition from liquid to FCC after which it remains FCC below the transition temperature. Above, it was assumed that element B has a lower melting point than A. To ensure this behaviour, σ_{M1A} for the first peak of A is made larger than σ_{M1B} for the first peak of element B. The resulting phase diagram is illustrated in Fig. 5.3(a).

Based on a similar treatment of the correlation variable, σ_{Mj}, we also constructed the isomorphous diagram of Fig. 5.3(b). Here both components directly transform to the stable FCC phase, at distinct temperatures, from the high temperature liquid phase. The lattice spacings from the peritectic phase diagram of Fig. 5.3(a) were kept the same for each respective component, while the effective transition temperatures are set such that the transformation from liquid to FCC occurs at different effective temperatures for the entire range of compositions.

The phase diagram calculations presented in this section illustrate the robustness of the XPFC binary alloy model, through the various parameters, to produce various experimentally relevant phase diagrams. Our approximations notwithstanding, we find that, at least for the case of the square-triangle system, they are in agreement with numerical validations.

5.6   XPFC Binary Model Applications

In this section we demonstrate the XPFC binary alloy model for phase transformation phenomena that represent paradigms of materials processes. First, we apply the model to the solidification of
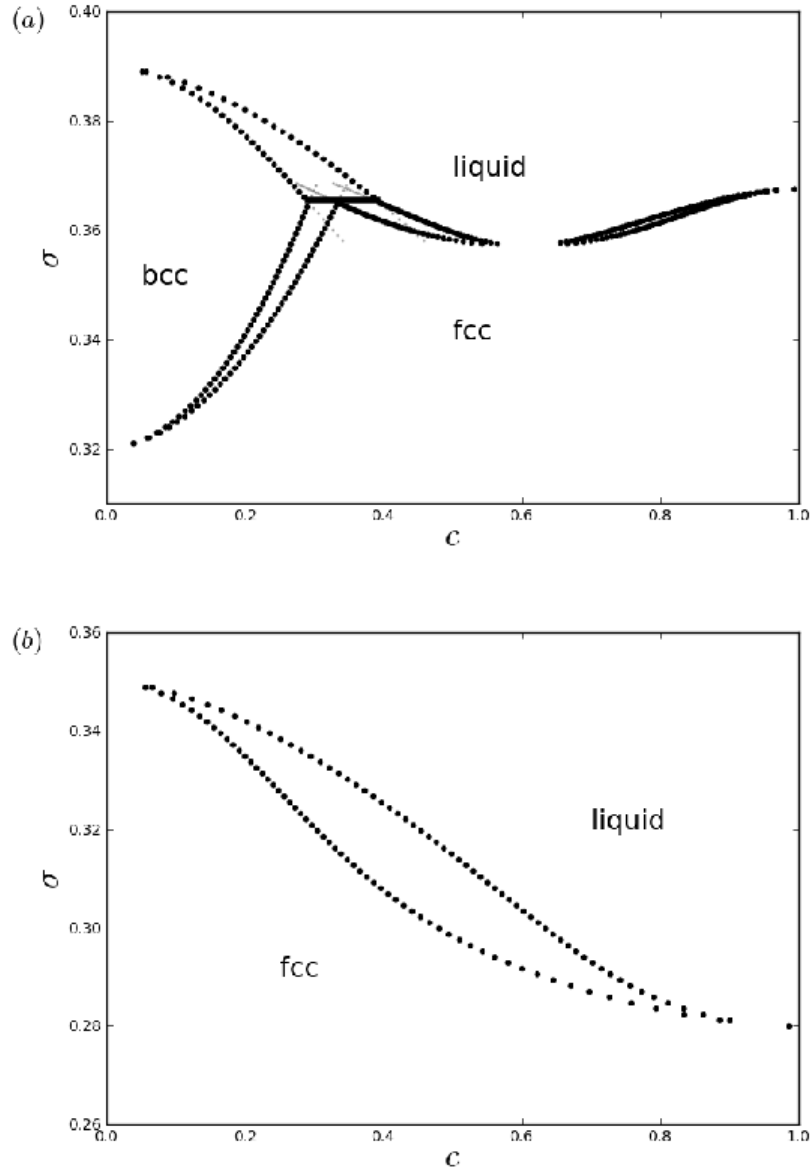
Figure 5.3: Phase diagram for 3D FCC and BCC structures. For both (a) and (b), parameters for the ideal portion of the energy are set to, $\eta = 1.3$, $\chi = 1$ and $\omega = 0.01$, and $c_\ell = 0.5$. Thin gray dots represent the metastable coexistence lines. (a) Peritectic, Fe-Ni type phase diagram. Correlation parameters are set to, $\alpha_{111A} = 0.4$, $\alpha_{100A} = 0.4$, $\alpha_{111B} = 0.6$ and $\alpha_{100B} = 0.6$ and the effective transition temperatures are set to $\sigma_{M111A} = 1.2$, $\sigma_{M100A} = 0.8$, $\sigma_{M111B} = 1.05$ and $\sigma_{M100B} = 1.05$ for elements A and B, respectively . (b) Isomorphous, high temperature Cu-Ni type phase diagram. Correlation parameters are set to, $\alpha_{111A} = 0.8$, $\alpha_{100A} = 0.8$, $\alpha_{111B} = 0.9$ and $\alpha_{100B} = 0.9$, while effective transition temperatures are, $\sigma_{M111A} = 1.0$, $\sigma_{M100A} = 1.0$, $\sigma_{M111B} = 0.8$ and $\sigma_{M100B} = 0.8$ for elements A and B, respectively [30].

eutectic lamellae involving components having similar and dissimilar structures. Secondly, we look at solute segregation, and its role in solute clustering around defects.

5.6.1 Eutectic Lamellae Growth

Compared with other growth process in materials science, such as dendritic growth and grain growth, there has been a lack in an exhaustive investigation of the growth processes of eutectic lamellae. A long standing weakness of previous theoretical and numerical studies of eutectic growth has been the lack of direct atomic scale features, such as structural and elasto-plastic effects. It stands to reason that such atomistic scale effects are paramount when investigating the co-operative growth and lamellae elimination processes involved during eutectic growth, since such properties are bound to manifest themselves in the energetics and diffusional aspects inherently involved. The present XPFC binary alloy model developed above is ideal, through its description of multiple structures, elasto-plasticity, grain boundaries, solute and defect interactions. Here we showcase, qualitatively, the co-operative eutectic growth of eutectic lamellae of two topologically identical structures.

For an alloy system, we choose the eutectic system above describing structurally similar components for the square-square binary system calculated above, with the results depicted in Fig. 5.4. Simulations were carried out in a domain of $10000\Delta x \times 2000\Delta x$ ($\sim 1500 \times 300$ lattice spacings), with numerical time step of $\Delta t = 3$ and grid spacing of $\Delta x = 0.15$. Equations of motions were solved by employing a semi-implicit Fourier technique[§]. Initial conditions comprised four individual lamella of each phase/structure ($\sim 22 \times 37$ lattice spacings), and initial concentration satisfying the tie line at the given temperature of $\sigma = 0.09$. Our structures being topologically identical, but differing lattice spacing, we only investigate the role of orientational mismatch between the given phases. Figure 5.4 plots different simulation time slices of the lamellae evolution for different mis-orientations between lamellae. In Fig. 5.5, we show an example of a simulation conducted where the eutectic lamellae is composed of dissimilar structures.

The surface and elastic energy dependence on orientation (mis-orientation) are well known and documented relationships. In Fig. 5.4, it is evident that these relationships lead to different coarsening and growth rates, as well as changes in the short circuit diffusion behaviour of the growing lamellae as a function of the mis-orientation. The mis-orientation also plays a critical role in the spacing selection process. As mis-orientations are changed, so does the surface energy characteristics, especially between the two growing solid phases. This results in different pinch off/elimination rates of individual lamella. On elimination of a particular lamella, there exists a temporary local region of depleted solute. The system must then wait for long range lateral diffusion to reintroduce a new short circuit diffusion path, which then allows for continual growth. The interplay between the aforementioned processes, i.e., pinch off, coarsening and short circuit diffusion, are all paramount in determining the final eutectic microstructure, particularly under transient conditions that dominate the complex formation of microstructure during industrial processing. The current XPFC binary alloy model, affords us the means by which we can study the effect of mismatched lattices, mis-orientations and anisotropic elastic and surface energies in a natural way.

5.6.2 Compositional Segregation

With the ability to produce and control multiple crystal structures, through the properties of a given correlation function, and the self consistency in describing defects and elasto-plasticity, our XPFC binary alloy model is well suited to study a myriad of interactions and phenomena. One such phenomena is solute segregation to defects. We use the phase diagram calculated above, where component A has square structural symmetry in equilibrium and B has triangle symmetry (Fig. 5.2), to consider the equilibrium segregation process in a binary alloy. The system is initialized to be a bi-crystal, of square lattices, i.e., dominated by component A, having a low angle tilt boundary,

---

[§]This technique is described in Appendix A

(a)   (b)   (c)
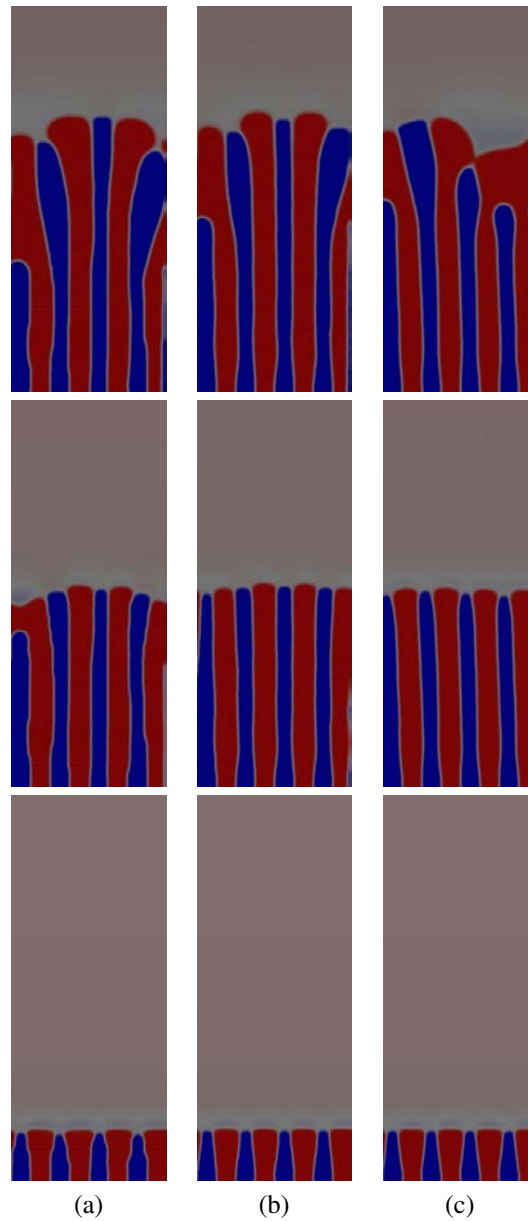
Figure 5.4: Snap shots of parts of the simulation domain of eutectic lamella, generated using the free energy used to produce the square-square phase diagram of Fig. 5.1. Eutectic quench temperature was $\sigma = 0.09$, at an average concentration of $c_o = 0.56$. Colour represents amount of solute, where low solute content is blue (Sq_A) and high is red (Sq_B). Different orientations of the structures were considered, low concentration structure versus high, represented by each column of images. The mis-orientations shown are: (a) 0 (b) 4 and (c)20 degrees. Simulation times are increasing from bottom to top [30].
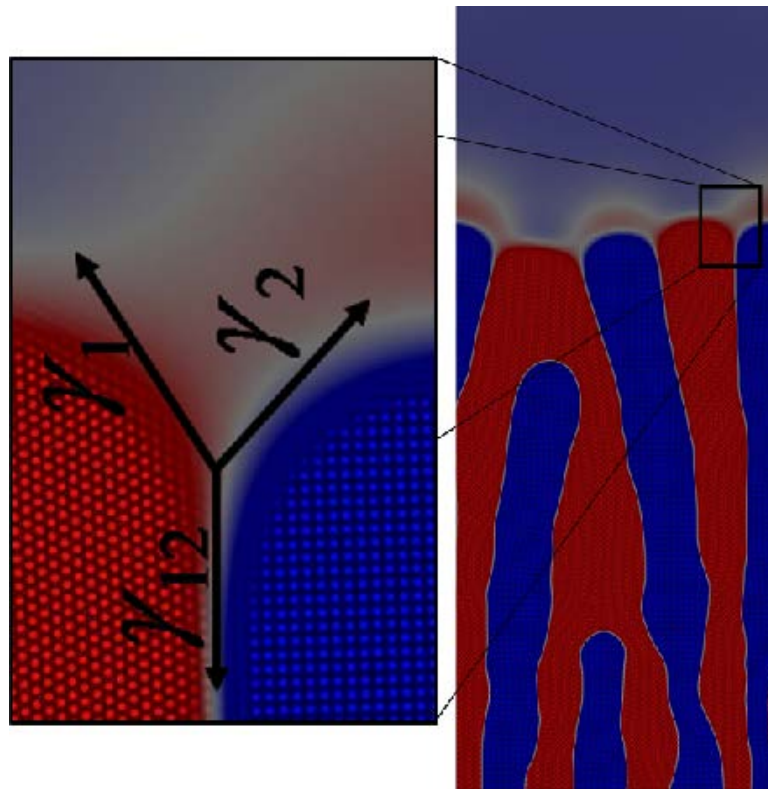
Figure 5.5: Time slice showing eutectic growth, where the alloy consists of structurally dissimilar elements. Portion of the simulations domain is shown here. Component A has an equilibrium structure of a square lattice, while B prefers to solidify to a triangular symmetry. Colour represents amount of solute, where low solute content is blue (Sq_A) and high is red (Sq_B). In these structurally different lamellae the surface energy between the triangle-liquid interface (γ_1), square-liquid interface (γ_2) and the square-triangle interface (γ_{12}) are set by the correlation kernel variables α_{Ai} and α_{Bi} [30].

with a uniform average solute content of $c_o = 0.1$. The system is then allowed to relax, where we consider two different behaviours due to the elastic parameters of each component, which can be set by tuning the widths of the correlation peaks. The first case we consider is an elastically isotropic phase for A, Fig. 5.6(a). Secondly, we consider an elastically anisotropic phase for A, Fig. 5.6(b).
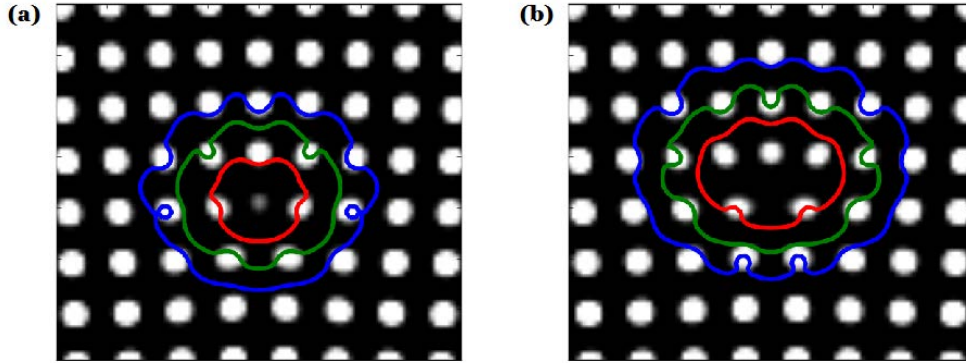
Figure 5.6: Segregation of solute to a dislocation forming part of the dislocation line in a low angle tilt boundary. Density, n, is shown in grayscale, while contours map out constant concentrations of $c = 0.12, 0.13$ and 0.14, from outside to inside. (a) elastically isotropic, i.e., $\alpha_{10A} = 0.8\sqrt{2}$ and $\alpha_{11A} = 0.8$ for A and (b) elastically anisotropic, i.e., $\alpha_{10A} = 0.8$ and $\alpha_{11A} = 0.8$ for A [30].

The choice and relative relationship between the elastic coefficients is manifested in three separate effects worth noting. According to Greenwood *et al.* [20], the bulk modulus of a square phase is proportional to the inverse of the sum of the two peak widths, i.e., $C_{11} + C_{12} \propto \alpha^{-2}$. Thus the stiffness is altered by increasing or decreasing the peak widths. This is evident in Fig. 5.6, where the amount of solute segregating to the defect is smaller when phase A is "soft" (a), and increases when phase A is stiff (b).

A second effect worth noting is the distribution of solute around the defect itself. With appropriate choice of the peak widths, we can achieve an elastically isotropic state, Fig. 5.6(a), for parameters for a "soft" matrix A phase, which leads to a compositional profile that is also isotropic, with a small anisotropy arising due to the defect itself. As the stiffness increases however, we find that the compositional profile also becomes more anisotropic Fig. 5.6(b), featuring a more elliptical distribution.

Finally, the third effect is the topology of the defect itself in terms of the density behaviour. A triangular phase can be described as a sheared state of a square structure, where in our model, the barrier for this shearing process is set by the elastic coefficients. A system with no shear barrier can be achieved by making the peak widths infinitely wide, essentially giving rise to a single peak correlation. Since in this demonstration, we have chosen finite widths for the correlation peaks, we have concurrently set the shear barrier for the system. In the limit where the shear barrier is small, i.e., for the "soft" system of Fig. 5.6(a), the system being in a frustrated state, attempts to select a more triangular phase causing the emergence of a low amplitude density peak in the defect itself. Where the matrix is stiff, i.e., corresponding to a larger shear barrier, Fig. 5.6(b), the defect chooses a structure commensurate with the matrix, thus eliminating the emergence of the density peak. All of these effects play a role in the selection of the compositional and density profiles around the defects. The relaxed state of these fields will thus affect how defects move and interact with grain boundaries or other defects during thermo-mechanical processing.

5.7   Application to Solute Clustering in Al-Cu Alloys

In this section, we apply the XPFC binary alloy model developed in this chapter to study the solute clustering mechanism in a model Al-Cu system. Solute clustering in metallic alloys represents the initial stages of a first-order phase transformation process occurring in bulk crystals. The method is employed often in the so-called precipitation hardening treatment of alloys, for achieving required mechanical properties, that takes place during late stage processing of materials. As such, understanding clustering mechanisms is paramount in the design engineering of alloys.

Theoretically, the nucleation mechanisms of early stage cluster are poorly understood. However, recent observations made using transmission electron microscopy [94, 95], 3D atom probe [96, 94] and positron annihilation [97], suggest that early clusters are associated with quenched-in bulk defects, such as excess vacancies and/or dislocation loops. The conjecture is that the collections of these defects decrease the energy barrier for nucleation, thus facilitating the clustering mechanism [96, 95, 94].

A study of clustering requires atomic scale features (defects, elasto-plasticity, etc.) operating on diffusive time scales, yet numerically efficient. Current atomistic scale modelling formalisms, e.g., MD, Monte Carlo, or dynamic DFT, are all restricted to either atomistic temporal and spatial scales or are numerically inefficient for large scale simulation. It is the aim of this section to report on a study on clustering in Al-Cu systems, having quenched-in defects (dislocations), using the current XPFC binary model. While the full details of the work is beyond the scope of this thesis[¶], we hope the salient features presented in this section serve to illustrate the full capability of the current XPFC model.

5.7.1   Al-Cu Phase Diagram Construction

To examine the clustering mechanism, here we construct a model Al-Cu type alloy, in 2D for simplicity. As demonstrated with the peritectic and isomorphous phase diagrams of Section 5.5, the XPFC binary alloy model is robust enough to admit a wide range of systems. We reconstruct the Al-rich portion of the Al-Cu phase diagram through manipulating the given parameters in the XPFC binary model. The Al-rich phase and terminal θ-phase are assumed to have square structural symmetry. Following the procedures outlined above and in Appendix B, Fig. 5.7 represents our model Al-Cu phase diagram, describing the Al-rich side.

5.7.2   Numerical Simulation of Early Clustering

Motivated from recent observations from TEM, 3D atom probe and positron annihilation measurements, as an initial condition, we initialize the system with a quenched bulk state with a random distribution of dislocations. According to this current hypothesis, vacancy and dislocation complexes (some in the form of defect loops), are the primary cause of early clustering and precipitation in Al-Cu alloys. The system is set to a uniform alloy composition, $c_o = 2at.\%$, at a solutionizing temperature $\sigma = 0.17$. Simulations using Eqs. (5.5) and (5.6) were conducted on a rectangular grid with grid spacing $\Delta x = 0.125$ and numerical time step $\Delta t = 1$, using a semi-implicit Fourier technique.

The initial state of our clustering simulations, shown in Fig. 5.8(b), was equilibrated for some time at the solutionizing temperature, following equilibration the system was quenched/aged at the ageing temperature of $\sigma = 0.04$. During ageing, small clusters initially appear with higher Cu-content than that of the originally distorted matrix. As the simulations proceed, some clusters of a non-critical size or lacking sufficient Cu-content decrease in size and Cu-content, or vanish entirely. Some clusters, particularly those in the vicinity of a large enough density of dislocations, stabilize and start increasing in size, e.g., Fig. 5.8(a). In contrast, when we increase the ageing temperature

---

[¶]The interested reader is referred to Ref. [32], for the full details of the study.
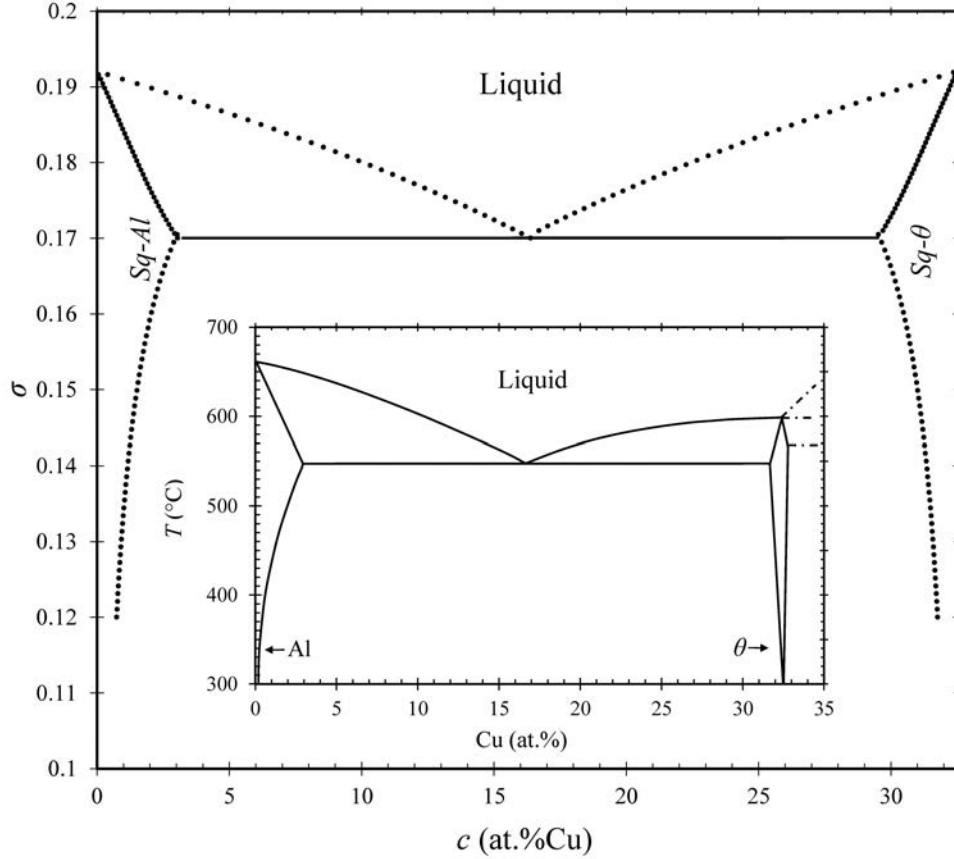
Figure 5.7: A reconstructed model Al-Cu type phase diagram, displaying the Al-rich side. Where, structures are approximated in 2D to have square symmetry. Inset shows an experimental (Al-rich side) Al-Cu phase diagram taken from Ref. [98]. Parameters for the ideal energy are set to, $\eta = 1.4$ and $\chi = 1$, $\omega = 0.005$ and $c_\ell = 0.5$. Correlation peak widths were set to, $\alpha_{11Al} = 2.4$, $\alpha_{10Al} = \sqrt{2}\alpha_{11Al}$, guaranteeing an elastically isotropic phase, and $\alpha_{11\theta} = 2.4$ and $\alpha_{10\theta} = \sqrt{2}\alpha_{11\theta}$. Equilibrium peak positions were chosen to mimic the relative atomic radii differences between Al and Cu and were chosen to be, $k_{11Al} = 2\pi$, $k_{10Al} = \sqrt{2}k_{11Al}$, $k_{11\theta} = (81/38)\pi$ and $k_{10\theta} = \sqrt{2}k_{11\theta}$. Transition temperatures are set to $\sigma_{M11Al} = 0.55$, $\sigma_{M10Al} = 0.55$, $\sigma_{M11\theta} = 0.55$ and $\sigma_{M10\theta} = 0.55$; and the concentration axis is rescaled to be commensurate with the maximum Cu-content ($\approx 32.5at.\%$) in the θ-phase [32].
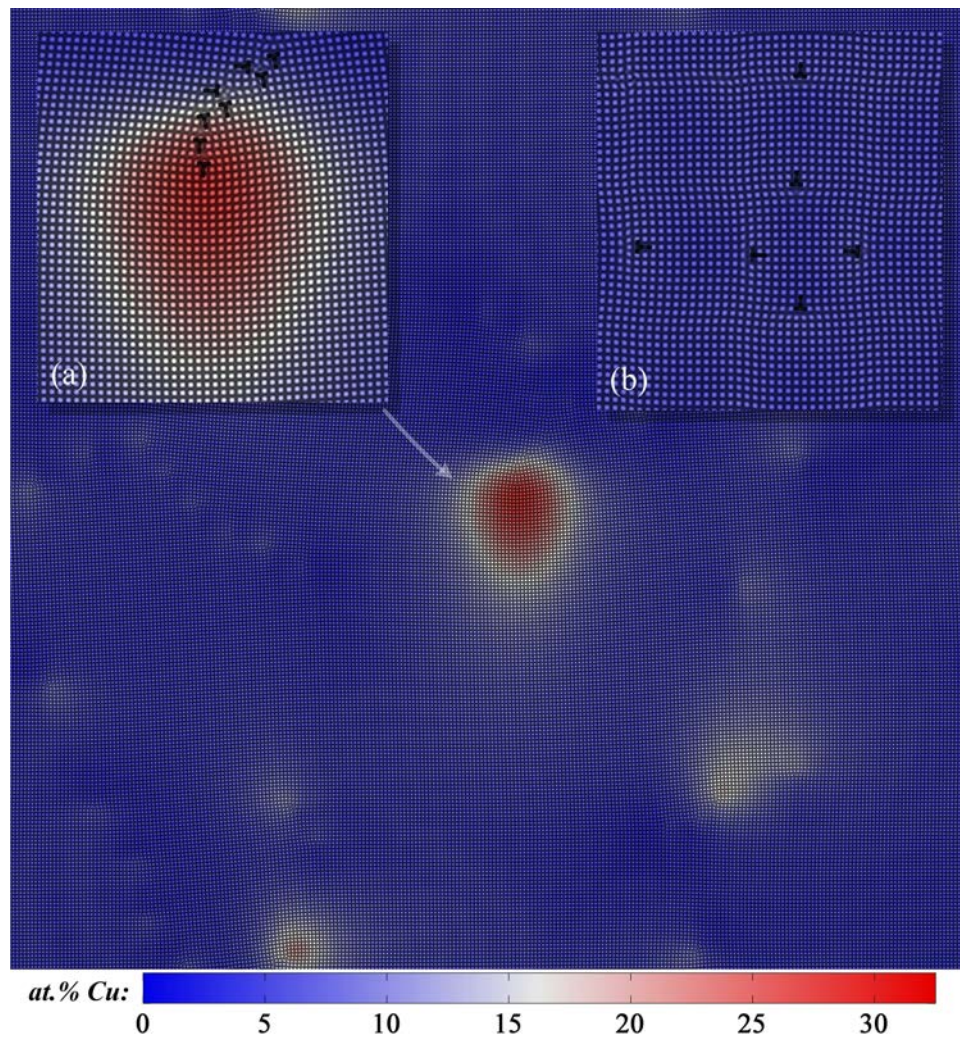
Figure 5.8: XPFC binary alloy simulation of clustering. Domain size shown is 256×256 lattice spacing, and after 225,000 iterations, the domain contains clusters of various sizes and solute content. (a) Long-lived well developed cluster; (b) Initial structure of the matrix distorted with randomly distributed dislocations. Colour indicates solute content, with blue representing low Cu-content while red is high Cu-content. Black symbols map out dislocations.

within the single-phase (Al) region, e.g., $\sigma = 0.16$, no clustering is observed and the initial distortions are removed from the matrix through dislocation-dislocation annihilation as the system heals itself. The dislocation-mediated clustering mechanism, evident in Fig. 5.8(a), is consistent with past TEM observations in Al-Cu alloys, and to our knowledge, our simulations are the first such atomistic scale numerical experiments which support the dislocation-assisted clustering and precipitation nucleation hypothesis.

5.7.3 Quantitative Analysis of System Energetics
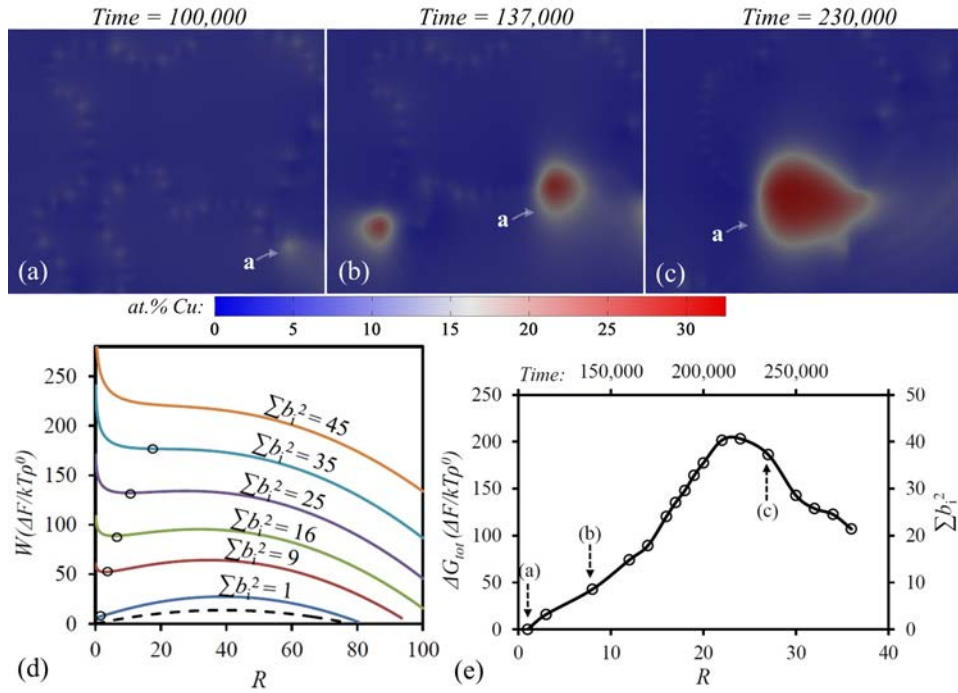
Figure 5.9: (a-c) Snapshots in time of the formation and growth of cluster "a"; (d) Plot of the work of formation (analytic) versus effective cluster radius (R) of increasing dislocation density (Σb_i^2), i.e., increasing strain fields. Dashed curve denotes work of formation for dislocation unassisted homogeneous nucleation ($\Sigma b_i^2 = 0$). The points on the curves represent the local minimum, which is seen to also shift to larger nucleus sizes until it vanishes; (e) Change in the total work of formation, ΔG_{tot} (numerically calculated in the neighbourhood of the cluster), and weighted average burger's vectors, Σb_i^2, versus effective cluster radius, R, [32].

Dislocation-mediated clustering can be quantified through analysis of the effect of dislocations on the nucleation through investigation of the work of formation. When considering dislocations, and their corresponding elastic contributions, the work of formation of a cluster can be written as,

$$W = 2\pi R\gamma + \pi R^2(-\Delta f + \Delta G_s) - \Delta G_{sr} + \Delta G_d, \qquad (5.10)$$

where R is the effective cluster radius in terms of lattice spacings, γ is a Cahn-Hilliard type interfacial energy, here taken to be solely chemical$^{\parallel}$. Δf represents the bulk thermodynamic driving

---

$^{\parallel}$With recent PFC work on describing surface energy [62, 60], a more complete treatment can also include structural information directly from the correlation functions.

force for nucleation of a cluster in the bulk matrix, ΔG_s is the coherent strain energy for a nucleus formed in the matrix [91], ΔG_{sr} denotes the energy associated with stress relaxation due to solute-dislocation interaction and ΔG_d is the dislocation energy**.

In Figure 5.9(d), we plot the work of formation for cluster "a" versus mean cluster radius, up to the largest cluster shown in Fig. 5.9(c). The mean concentration is that evaluated for an effective radius given by R. The lower bound dashed curved in Fig. 5.9(d) denotes the work of formation associated with homogeneous nucleation neglecting the effects of dislocations, i.e., $\Sigma b_i^2 = 0$ (the weighted average of the burgers vectors of dislocations surrounding a given cluster). Though the energy barrier for homogeneous nucleation seems to be smaller than that of a single dislocation ($\Sigma b_i^2 = 1$), Fig. 5.9(d) demonstrates that the energy barrier can be reduced significantly when in the neighbourhood of a large enough collection of dislocations. A phenomenon originally dating back to the work of Cahn [99], who proposed it in the context of one dislocation that can reduce the barrier. Here we have generalized this mechanism to account from strain from a stochastic field of dislocations. These results present some apparently counterintuitive results, in that they predict an increasing critical radius with accumulating dislocation energy, as well as an increasing overall free energy within the neighbourhood wherein the dislocations accumulate. The crucial mechanism that is at work here, however, is that the relative energy barrier separating a spontaneous growing cluster to a subcritical cluster at a local equilibrium is diminishing with the accumulating strain energy field. It is likely that this mechanism is more generic and applies to any defects that can collectively work to locally strain the field around a cluster of solute atoms. One of these defects is so-called vacancy loops that are quenched in after a rapid temperature quench during heat treatments of aerospace alloys.

Further to considering the work of formation, our system can also be quantified by examining the change in the total work of formation, ΔG_{tot}, of some representative box encapsulating cluster "a" during its formation and growth. The change in total work of formation can be described as the grand potential difference, mathematically written as,

$$
\begin{aligned}
\Delta G_{tot} &= \int_V \Omega - \int_V \Omega^b \\
&= \int_V [f - \mu_c c - \mu_n n] - \int_V [f^b - \mu_c^b c^b - \mu_n^b n^b].
\end{aligned}
\tag{5.11}
$$

$\mu_c = \frac{\partial f}{\partial c}$ and $\mu_n = \frac{\partial f}{\partial n}$ are the chemical potentials of the concentration and density field, respectively, and V is the total encapsulated volume around the cluster. In this formulation, we are assured that all elastic, interfacial and bulk contributions are included, as the grand potential is a function of the free energy. It is noted that, though the growth of cluster "a" may cause an increase in the local free energy, other parts of the system undergo a decrease in energy caused by the homogenization of sub-critical clusters, dislocations and solute, leading to an overall minimization of the system free energy. As evident in Fig. 5.9(e), there is an increase in the change of the total work of formation until a maximum is reached, i.e., the critical nucleation radius, after which there is a decrease. Moreover, the numerically calculated values of Σb_i^2 for various sizes of cluster "a", are in very good agreement with those calculated analytically in Fig. 5.9(d).

Our simulation data demonstrates a continuous growth of cluster "a" mediated by dislocations, where for each sub-critical size, the system is considered to be in local equilibrium. This is analogous to previous PFC studies of crystal nucleation in solid-liquid systems [100, 57], we refer to sub-critical clusters which grow continuously as metastable precursors to the formation of cluster "a" at its critical size. This mechanism of growth, makes it favourable, thermodynamically, for continuous growth of the cluster by attracting more solute atoms from the surrounding matrix.

**Details of the specific definitions of the energetic terms can be found in Ref. [32].

5.8   Summary and Conclusions

In this chapter, we reduced the multi-component XPFC model of Chapter 4 to represent the simplest case of structural transformations in binary alloys. We presented a wide range of realistic phase diagram calculations, eutectic, peritectic and isomorphous, demonstrating the robust capability of the XPFC binary model.

We demonstrated the model for two potential applications where atomic scale elasto-plastic effects operating on diffusive time scales are of practical importance in the design engineering of materials. First we examined the growth of eutectic lamellae for both structurally similar and dissimilar phases. We qualitatively found that along with structural and lattice mismatch, orientational mismatch between phases plays an important role in the spacing selection processes of such system. Secondly, we investigated solute segregation to dislocations of a low angle tilt boundary in materials. The afforded control over structures and their underlying elastic properties allowed us to investigate the compositional and density variations and their interactions resulting from the elastic properties of the material inherited from the effective correlation function.

Finally, we applied our model to the study of the mechanisms of clustering in quenched/aged Al-Cu alloys. Our XPFC binary alloy simulations were the first, to our knowledge, atomistic scale modelling formalism which are consistent with the current defected-mediated (dislocations in our simulations) clustering hypothesis in the literature.

In the next chapter, we reduce the multi-component model to the more complex ternary alloy system and investigate its properties.

Chapter 6

Specialization of the Multi-Component Model to Ternary Systems and Application to Ageing in Ternary Alloys

Chapter 5 explored a binary representation of the multi-component XPFC model derived in Chapter 4. Its equilibrium and dynamic properties were studied, culminating in its application to clustering in Al-Cu alloys. In this chapter we consider the more complex ternary alloy system. After describing the appropriate free energy functional and related model parameters, we demonstrate its equilibrium and dynamic properties. Lastly, we investigate clustering in the presence of multiple solute species.

6.1 Motivation

Unlike binary alloys, there have been less investigations and studies conducted in ternary and higher order component alloys. This is because the inclusion of even a single additional alloying element can make measurements or observations difficult, as solute-solute, solute-defect and defect-defect interactions can become highly complex and non-linear in their descriptions. Numerical modelling affords us an avenue from which we can include such complex behaviour of several alloying components.

In the following pages, we reduce the multi-component model derived previously to ternary alloy systems. With a ternary reduction in hand, we examine its validity and capability by constructing phase diagrams. We follow by demonstrating its kinetic behaviour with dendritic and eutectic solidification. Lastly, we revisit the phenomena of clustering with the effect of three alloying species. The ternary model is applied to the study of clustering in a Al-Cu-Mg system, where the addition of an extra solute species is found to have repercussions on the final microstructure.

We have organized the chapter as follows. First, we discuss the approximations required in reducing the multi-component model in Section 6.2, followed by a description of the effective ternary correlation kernel in Section 6.3. Section 6.4 presents the dynamic equations for our ternary XPFC model, following which we discuss the equilibrium properties for a couple of choice systems in Section 6.5. The kinetic properties of the model are demonstrated in Section 6.6. Finally, we apply the model to clustering in ternary systems in Section 6.7 and conclude the chapter.

6.2 Simplified XPFC Multi-Component Energy Functional for Ternary Alloys

In this section, we reduce the simplified free energy functional of Section (4.9) to the case of three-components (A, B, C), or ternary alloys. To do so, we describe the system in terms of two solute components, c_A and c_B, where the third component can be deduced from mass conversation, i.e., $c_C = 1 - c_A - c_B$. Analogous descriptions are also imposed on the accompanying reference compositions, c_i^ℓ.

Specializing Eq. (4.9) for 3-components, with the above mentioned conditions, the ternary simplified free energy functional reads[*]

$$\mathcal{F}^{\text{ter}} = \int d\mathbf{r} \left\{ \frac{n^2}{2} - \eta \frac{n^3}{6} + \chi \frac{n^4}{12} + \omega F_{\text{mix}}^{\text{ter}}(c_A, c_B)(n+1) \right. \tag{6.1}$$

$$\left. - \frac{1}{2} n \int d\mathbf{r}' C_{\text{eff}}^{\text{ter}}(|\mathbf{r} - \mathbf{r}'|) n' + \frac{\kappa_A}{2} |\nabla c_A|^2 + \frac{\kappa_B}{2} |\nabla c_B|^2 \right\},$$

where $n' \equiv n(\mathbf{r}')$, η, χ and ω are treated hereafter as fitting parameters, and $\kappa_A > 0$ and $\kappa_B > 0$ are the gradient energy coefficients, defined by $\kappa_A = -\kappa_{AA} + \kappa_{AC} + \kappa_{CA}$ and $\kappa_B = -\kappa_{BB} + \kappa_{BC} + \kappa_{CB}$, respectively[†]. The entropy of mixing, $F_{\text{mix}}^{\text{ter}}$, for a ternary system given the above constraints modifies to

$$F_{\text{mix}}^{\text{ter}}(c_A, c_B) = c_A \ln \left(\frac{c_A}{c_A^\ell} \right) + c_B \ln \left(\frac{c_B}{c_B^\ell} \right) + (1 - c_A - c_B) \ln \left(\frac{1 - c_A - c_B}{1 - c_A^\ell - c_B^\ell} \right), \tag{6.2}$$

where c_A^ℓ and c_B^ℓ are reference liquid compositions. Equation (6.1) has a similar form to the simplified binary model. It couples the contribution for the total density, like that of the original XPFC model of Greenwood *et al.* [19, 20] (described in Section 2.2.5), to an entropy of mixing term which can be Taylor expanded to yield Cahn-Hilliard like terms in solute species c_A and c_B.

6.3 Effective Correlation Properties

With the definition of the simplified ternary free energy defined by Eq. (6.1), we now define the effective correlation function suitable for a ternary alloy system. For three components, the effective correlation function is defined by,

$$C_{\text{eff}}^{\text{ter}}(|\mathbf{r} - \mathbf{r}'|) = X_A(c_A, c_B) C_2^{AA}(|\mathbf{r} - \mathbf{r}'|) \tag{6.3}$$
$$+ X_B(c_A, c_B) C_2^{BB}(|\mathbf{r} - \mathbf{r}'|) + X_C(c_A, c_B) C_2^{CC}(|\mathbf{r} - \mathbf{r}'|),$$

such that the interpolation functions satisfy $X_A + X_B + X_C \equiv 1$ at all compositions. Here, their particular form is chosen to model the generic properties of eutectic systems. However, by careful alteration of other parameters, other alloy systems can be modeled, e.g. isomorphous and peritectic systems[‡]. Their specific forms chosen here are,

$$X_A(c_A, c_B) = 3c_A^2 + 2c_A c_B - 2c_A^3 - 2c_A^2 c_B - 2c_A c_B^2$$

---

[*]We have neglected cross gradient terms, which arise after imposing the conservation condition, as they are interpreted to be of higher order. Note that such terms can become important for studying particular phenomena and can be added quite readily.

[†]Concentration gradients and their coefficients are derived in Appendix C.

[‡]See Section 5.5 of the preceding chapter.

$$X_B(c_A, c_B) = 2c_A c_B + 3c_B^2 - 2c_A^2 c_B - 2c_A c_B^2 - 2c_B^3$$
$$X_C(c_A, c_B) = 1 - 3c_A^2 + 2c_A^3 - 3c_B^2 + 2c_B^3 - 4c_A c_B + 4c_A^2 c_B + 4c_A c_B^2. \tag{6.4}$$

The construction of each individual correlation function, $C_2^{ii}(|\mathbf{k}|)$, corresponding to each respective pure component, follows from the pure material work of Greenwood *et al.* [19, 20]. They are constructed in Fourier space, where to represent the structure of interest, a select number of spectral peaks are added, with the total correlation being the numerical envelope of all such spectral peaks.

6.4   Ternary Model Dynamics

The density and each composition field follow conserved dissipative dynamics. They are derived variationally, written as

$$\frac{\partial n}{\partial t} = \nabla \cdot \left(M_n \nabla \left\{ n - \eta \frac{n^2}{2} + \chi \frac{n^3}{3} + \omega F_{\text{mix}}^{\text{ter}} - C_{\text{eff}}^{\text{ter}} n \right\} \right), \tag{6.5}$$

for the density field. While for each solute field, we have,

$$\frac{\partial c_A}{\partial t} = \nabla \cdot \left(M_{c_A} \nabla \left\{ \omega(n+1) \frac{\delta F_{\text{mix}}^{\text{ter}}}{\delta c_A} - \frac{1}{2} n \frac{\delta C_{\text{eff}}^{\text{ter}}}{\delta c_A} n - \kappa_A \nabla^2 c_A \right\} \right), \tag{6.6}$$

$$\frac{\partial c_B}{\partial t} = \nabla \cdot \left(M_{c_B} \nabla \left\{ \omega(n+1) \frac{\delta F_{\text{mix}}^{\text{ter}}}{\delta c_B} - \frac{1}{2} n \frac{\delta C_{\text{eff}}^{\text{ter}}}{\delta c_B} n - \kappa_B \nabla^2 c_B \right\} \right), \tag{6.7}$$

where M_n, M_{c_A} and M_{c_B} are dimensionless mobility coefficients for density and compositions fields. They are set to 1 throughout the remainder of this chapter. The shorthand notation used in Eqs. (4.13) and (4.14) have also been used here. Once again, we have neglected noise terms in the dynamic equations for the illustrations and applications shown here. They can easily be included in the equations above making them stochastic.

6.5   Equilibrium Properties

Ternary equilibrium is defined by co-existence of bulk phases, e.g. solid$_\alpha$-solid$_\beta$, liquid-solid$_\alpha$-solid$_\beta$, etc. The governing properties, e.g. partitioning, of such an equilibrium state can be determined from standard thermodynamic minimization methods. In general, for 3-component alloys, free energy minimization is defined by a common plane tangent between the free energy wells of any two or three coexisting phases[§]. This construction is a geometrical representation of the statement that the chemical potentials and grand potentials of any two phases are equal with respect to each component. Here, we construct isothermal ternary phase diagrams by examining all combinations of phase coexistence (e.g., solid$_\alpha$-liquid, solid$_\alpha$-solid$_\beta$, etc.).

[§]The number of possible phases that can be in equilibrium is determined by Gibbs phase rule.

6.5.1 Phase Diagram Construction Method

For solid phases, the density field, which varies on atomic length scales, is approximated using a multi-mode approximation given by

$$n_i(\mathbf{r}) = \sum_{j=1}^{N_i} \varphi_j \sum_{l=1}^{N_j} \exp\left(\frac{2\pi}{a_i}\mathbf{ik}_l \cdot \mathbf{r}\right), \tag{6.8}$$

where a_i is the lattice spacing of the solid phase i and N_i denotes the number of mode families (families of planes) in the unit cell of phase i, φ_j is the amplitude associated with the jth family of planes. Each mode contains N_j reciprocal lattice peaks, enumerated by the index l. Strictly speaking, there is a distinct amplitude, $A_{l,j}$, for each reciprocal lattice peak. However, for the purposes of simplifying the construction of phase diagrams (i.e., working with the fewest number of variables to minimize), they are assumed constant leading to φ_j.

Substituting Eq. (6.8) into Eq. (6.1), and integrating over one unit cell, the free energy can be calculated for each phase as a function of c_A, c_B and the amplitudes φ_j. Since amplitudes are non-conserved fields, the resulting free energy is then minimized with respect to each φ_j. The result is substituted back into the free energy. After this procedure, we are left with an energy landscape, $\mathcal{F}_{sol}^{\text{ter}}(c_A, c_B)$, where $\mathcal{F}_{sol}^{\text{ter}}$ represents an amplitude-minimized solid free energy[¶]. As with previous XPFC models presented, we neglect the contribution of a $\mathbf{k} = 0$ mode to the correlations and therefore explicitly assume that the density of all phases is close to the reference, i.e., $n_o = 0$. For the liquid phase, the free energy $\mathcal{F}_{liq}^{\text{ter}}(c_A, c_B)$ is trivially computed by setting all $\varphi_j = 0$

With the free energy landscapes of liquid and solids, the phase boundary lines between a combination of phases at a given temperature parameter, σ, are computed by solving the following set of equations simultaneously,

$$\mu_{c_A}^I = \mu_{c_A}^J$$
$$\mu_{c_B}^I = \mu_{c_B}^J$$
$$\Omega^I = \Omega^J, \tag{6.9}$$

where the last of these implies,

$$f^I - \mu_{c_A}^I c_A^I - \mu_{c_B}^I c_B^I = f^J - \mu_{c_A}^J c_A^J - \mu_{c_B}^J c_B^J. \tag{6.10}$$

The superscripts I and J denote any two phases in equilibrium (e.g. liquid-solid$_\alpha$), respectively. The expressions $\mu_{c_A}^I = \partial f^I/\partial c_A$ and $\mu_{c_B}^I = \partial f^I/\partial c_B$ are the chemical potentials of phase I with respect to the concentrations c_A and c_B, respectively, with analogous definitions for $\mu_{c_A}^J$ and $\mu_{c_B}^J$. The expressions Ω^I and Ω^J are the grand potentials of phases I and J, respectively. See Appendix B for further details on calculating phase diagrams. The set of conditions in Eq. (6.9), along with Eq. (B.13) defining the average concentration, can be solved to find the four equilibrium concentrations (two per phase) defining coexistence on a given tie line.

6.5.2 Ternary Eutectic Alloys

A first example of the equilibrium properties of the ternary XPFC model is demonstrated for a system where all three components (A, B, and C) are structurally similar, differing only in their equilibrium lattice spacings. Here, 2D square symmetry is assumed as the equilibrium structure for each pure component, which in this context implies that all $\hat{C}_2^{ii}$ have the same number of peaks, with the corresponding ratios of their positions in reciprocal space being the same. However, each

---

[¶]It is noted that there will be one free energy for the $\varphi = 0$ -liquid-solution and one for the $\varphi \neq 0$ -solid-solution).

structure is differentiated by the absolute positions (k_j) of each peak. Though it has not been done here, by adjusting the widths (α_j) of each peak, each element can also be differentiated by different elastic and surface energies. The full list of parameters used to construct the phase diagrams in this subsection are listed in the caption of Fig. 6.1.

Allowing all three components to have square structural symmetry, at sufficiently low temperature we can construct a bulk solid free energy landscape describing multiple solid phases. The solid free energy is described by an effective lattice parameter (a^{ter}), that is a weighted average of the individual lattice parameters of all three components, using the interpolation functions of Eq. (6.4), namely, $a^{\text{ter}} = a_A X_A + a_B X_B + a_C X_C$. This leads to the solid-liquid free energy landscape in Fig. 6.1(a) for $\sigma = 0.17$, where the values of all other parameters are specified in the figure caption. The corresponding isothermal phase diagram is illustrated in Fig. 6.1(c), which is constructed form the coexistence lines calculated between the liquid phase and the different solid-solution phases, using the set of conditions in Eq. (6.9). Figure 6.1(b) shows an isothermal cut at a higher temperature, i.e., $\sigma = 0.182$, depicting an increased region where the bulk liquid is stable compared to the solid phases. At sufficiently low temperature, the free energy admits eutectic coexistence of three phases. We construct an isothermal cut right above the eutectic temperature, i.e., at $\sigma = 0.164$, shown in Fig. 6.1(d). The corresponding concentrations c_A and c_B in Fig. 6.1, are given as fractions, where unity represents pure A or B, respectively, along each axis of the phase diagram.

6.5.3   Simplified Al-Cu-Mg Type Alloy

The parameters of the ternary XPFC model can be chosen to produce sections of experimental phase diagrams, qualitatively, as in the work of Fallah *et al.* [32] and Section 5.7, where the binary XPFC model was used to model clustering and precipitation in a 2D model of the Al-Cu system. Here, we demonstrate how the equilibrium properties of a portion of the Al-rich (simplified) part of the Al-Cu-Mg phase diagram can be described qualitatively by the ternary XPFC model. An experimental phase diagram at $400°C$ is shown in Fig. 6.2(b), taken from Ref. [101]. We will use this phase diagram in Section 6.7, to study clustering and precipitation in Al-Cu-Mg ternary alloy systems.

Consider the part of the phase diagram for (Al)$-\beta$-θ outlined by the red dashed line and circled solid phases in the experimental phase diagram shown in Fig. 6.2(b), and ignoring the (Al)+S and (Al)+β+T phase regions. In the dilute-Mg region, a eutectic transition occurs between the Al-rich, (Al)-FCC phase, and an intermediate phase, θ, which has a tetragonal crystal structure. The eutectic system of (Al)-θ has a small solubility for Mg, however past the maximum solubility limit, there exists other intermediate phases terminating at the cubic β-phase. The equilibrium lattice constants (and thus the positions of the reciprocal space peaks) of θ and β phases are determined by interpolating between those of Al with 32.5 at.%Cu, and Al with 38.5 at.%Mg, respectively. For simplicity, we assume a square structural symmetry for all three equilibrium phases, and like the preceding section, the effective lattice constant is interpolated by weighting using the local solute compositions, c_{Cu} and c_{Mg}. The parameters (η, χ, ω), along with the peak widths α_j are chosen to give a satisfactory mapping of the solubility limits of the (Al)-phase for Cu and Mg to those in the experimental phase diagram of Fig. 6.2(b), for a range of temperature parameters (σ). The full list of parameters used to construct the phase diagrams in this subsection are listed in the caption of Fig. 6.2.

Figure 6.2(a), shows the free energy landscape for the solid at $\sigma = 0.04$. Figure 6.2(c) shows the corresponding isothermal phase diagram at $\sigma = 0.04$, where the inset shows a zoomed in image of the Al-rich corner. Comparing the inset with the Al-rich corner of the experimental phase diagram, reasonable agreement is evident between the calculated and the experimental phase diagram. Figure 6.2(d) shows the isothermal phase diagram for $\sigma = 0.155$. At this higher temperature (still below the eutectic), there is an increase in the solubility limits of the phase boundaries. Section 6.7 will use this phase diagram to demonstrate the initial stages of solid-state precipitation.
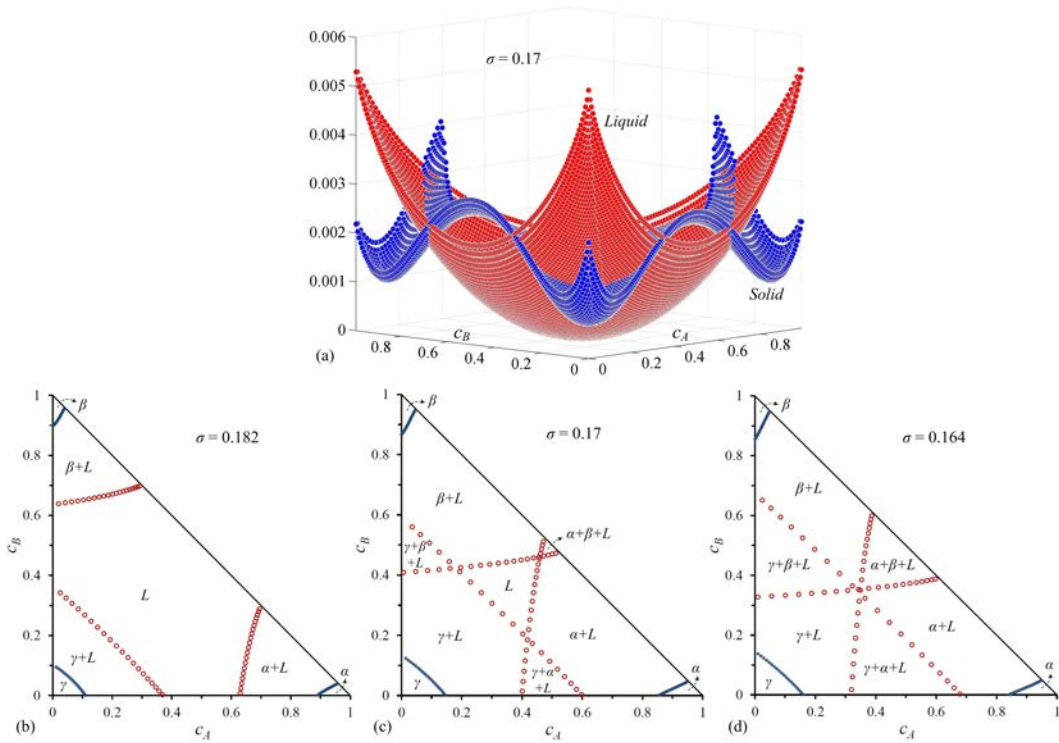
Figure 6.1: Ternary eutectic system: (a) Solid and liquid energy landscapes of a square-square-square (A-B-C) system at temperature parameter $\sigma = 0.17$. Corresponding phase diagrams at temperatures (b) $\sigma = 0.182$, (c) $\sigma = 0.17$ and (d) $\sigma = 0.164$. The parameters for ideal free energy and entropy of mixing were $\eta = 1.4$, $\chi = 1$, $\omega = 0.005$, while reference concentrations were $c_A^\ell = 0.333$ and $c_B^\ell = 0.333$. Widths of the correlations peaks are taken $\alpha_{11} = 0.8$ and $\alpha_{10} = \sqrt{2}\alpha_{11}$ for all phases. The peak positions for the given structures are $k_{11A} = (81/38)\pi$ and $k_{10A} = \sqrt{2}k_{11A}$ for α, $k_{11B} = (54/29)\pi$ and $k_{10B} = \sqrt{2}k_{11B}$ for β and $k_{11C} = 2\pi$ and $k_{10C} = \sqrt{2}k_{11C}$ for γ. The effective transition temperatures are set to $\sigma_{Mj} = 0.55$ for all family of planes in all phases. The concentrations on the isothermal phase diagrams are read in a Cartesian coordinate system.
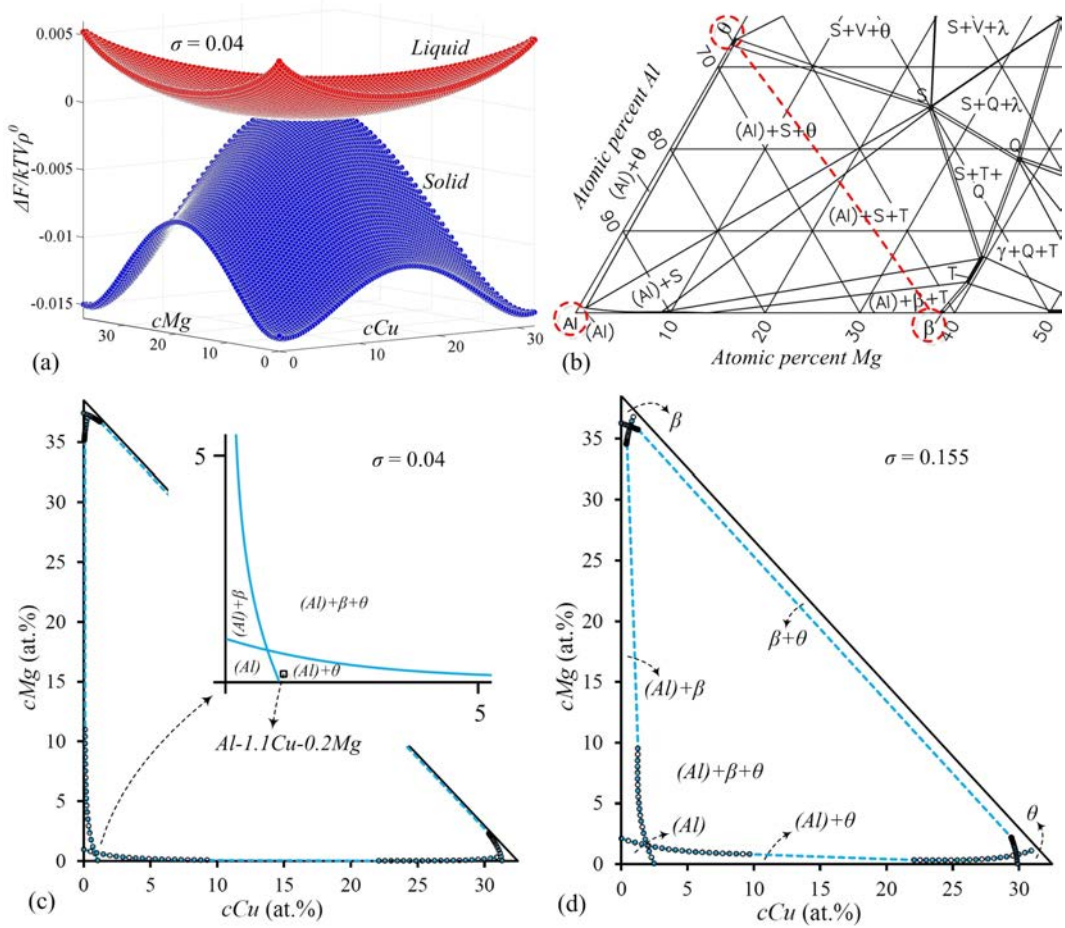
Figure 6.2: Al-Cu-Mg Phase diagram: (a) Solid and liquid energy landscapes of a square-square-square ($(Al)-\beta-\theta$) system at temperature $\sigma = 0.04$, (b) The Al-rich side of an isothermal cut (at $400°C$) from the experimental phase diagram of the Al-Cu-Mg system taken from Ref. [101]. Dashed circles mark the regions of the Al-rich (Al), Cu-rich (θ) and Mg-rich (β) regions considered for reconstruction by the model phase diagram. Reconstructed phase diagrams at temperatures (c) $\sigma = 0.04$ and (d) $\sigma = 0.155$. The parameters for ideal free energy and entropy of mixing were $\eta = 1.4$, $\chi = 1$, $\omega = 0.005$, $c_{Cu}^o = 0.333$ and $c_{Mg}^o = 0.333$. Widths of the correlations peaks are $\alpha_{11} = 0.8$ and $\alpha_{10} = \sqrt{2}\alpha_{11}$ for all phases. The peak positions are $k_{11(Al)} = 2\pi$, $k_{10(Al)} = \sqrt{2}k_{11(Al)}$, $k_{11\theta} = (2.0822)\pi$, $k_{10\theta} = \sqrt{2}k_{11\theta}$, $k_{11\beta} = (1.8765)\pi$ and $k_{10\beta} = \sqrt{2}k_{11\beta}$. For all family of planes, $\sigma_{Mj} = 0.55$, in all phases. The maxima in concentrations c_{Cu} and c_{Mg} are rescaled from unity, 1, to correspond to the Cu and Mg-content in the θ-phase and β-phase given by the experimental phase diagram, i.e., ≈ 32.5 and ≈ 38.5 $at.\%$, respectively. The concentrations on the isothermal phase diagrams are read in a Cartesian coordinate system.

6.6   XPFC Ternary Model Applications

The binary XPFC approach was previously demonstrated as a tool with which to model the role of defects and elasticity in structural phase transformations that operate over diffusive time scales. Further to these capabilities, the ability to have multi-component interactions between solute atoms and defects now makes it possible to examine much more complex interactions of the above atomic-scale effects with different solutes, and their diffusion. This capability opens a myriad of possibilities for applications for microstructure engineering in materials. This section showcases some applications of the XPFC ternary model presented in this chapter. In particular, using phase diagrams from the previous section, we demonstrate dendritic and eutectic solidification, and precipitation in the presence of two solute species. These phenomena are paradigms of microstructure evolution of relevance to materials engineering applications and are strongly influenced by diffusion of impurities, elastic strain, crystal anisotropy and defect structures.

6.6.1   Dendritic Solidification

Dendritic solidification arises when a supercooled liquid is quenched into the solid-liquid coexistence part of the phase diagram. Figure (6.3) shows snapshots in time of a dendritic crystal in a ternary alloy. The simulation was done using the phase diagram in Fig. 6.1(b). Simulations were conducted in a 2D domain of size $768a \times 768a$, where a is the lattice spacing. A uniform grid spacing and discrete time of $\Delta x = 0.125$ (which makes for a domain of size 6144×6144 grid points) and $\Delta t = 3$ were used and equations of motion, (6.5), (6.6) and (6.7), were solved semi-implicitly in Fourier space. The initial conditions consisted of a small circular seed of diameter, $d = 8a$ of the γ-phase, seeded in liquid at a temperature of $\sigma = 0.182$. The initial concentration of solute components A and B was uniform in both phases and set to the average alloy values $c_{o,A} = 0.1$ and $c_{o,B} = 0.1$. Several time slices of the simulation domain, showing the fields (n, c_A and c_B) at early times, are shown in Fig. 6.3.

As time progresses during the simulation, Fig. 6.3(a)-(c), dendritic growth is evident. The crystal develops a characteristic 4-fold symmetry of the underlying square crystal structure, produced with the correlation function for the given pure component of the γ-phase. The top two rows show the time evolution of the concentration fields (from left to right), c_A and c_B, respectively, indicating the interface boundary layer for each component. Both solutes, A and B, reach their maximum solute content at the interface of the growing dendrite, in agreement with the solute rejection mechanism of crystal growth. The bottom row shows the evolution of the density. There is also evidence of the associated density jump at the interface between solid and liquid phases as depicted by the light halo-like region around the interface. Figure 6.4 shows a composite view of the dendrite at later time, highlighting in each quadrant one of the three fields. This simulation depicts multiple diffusing species, density changes and surface tension anisotropy. In a larger numerical domain (where multiple dendrites can be grown), grain boundaries would also naturally emerge. It is noteworthy that these physical ingredients arise self-consistently and are very straightforward to simulate numerically. We also note that side-branching of the growing dendrite is not observed in Fig. 6.3 due to the size of the simulation domain and the exclusion of thermal noise in the dynamical equations.

6.6.2   Eutectic Solidification

Highly concentrated alloys feature solidification of coexisting solid phases. An example of these is eutectic growth, where co-existing solid phases grow by co-operative diffusion, a mechanism that allows eutectic colonies to grow with different kinetics than dendritic crystals. Figure (6.5) shows time slices of a simulation of a ternary eutectic colony for the alloy system studied in the previous section. The simulation was done using the phase diagram of Fig. 6.2(d). The temperature was set at $\sigma = 0.164$, with alloy concentrations $c_{o,A} = 0.6$ and $c_{o,B} = 0.025$, respectively. The
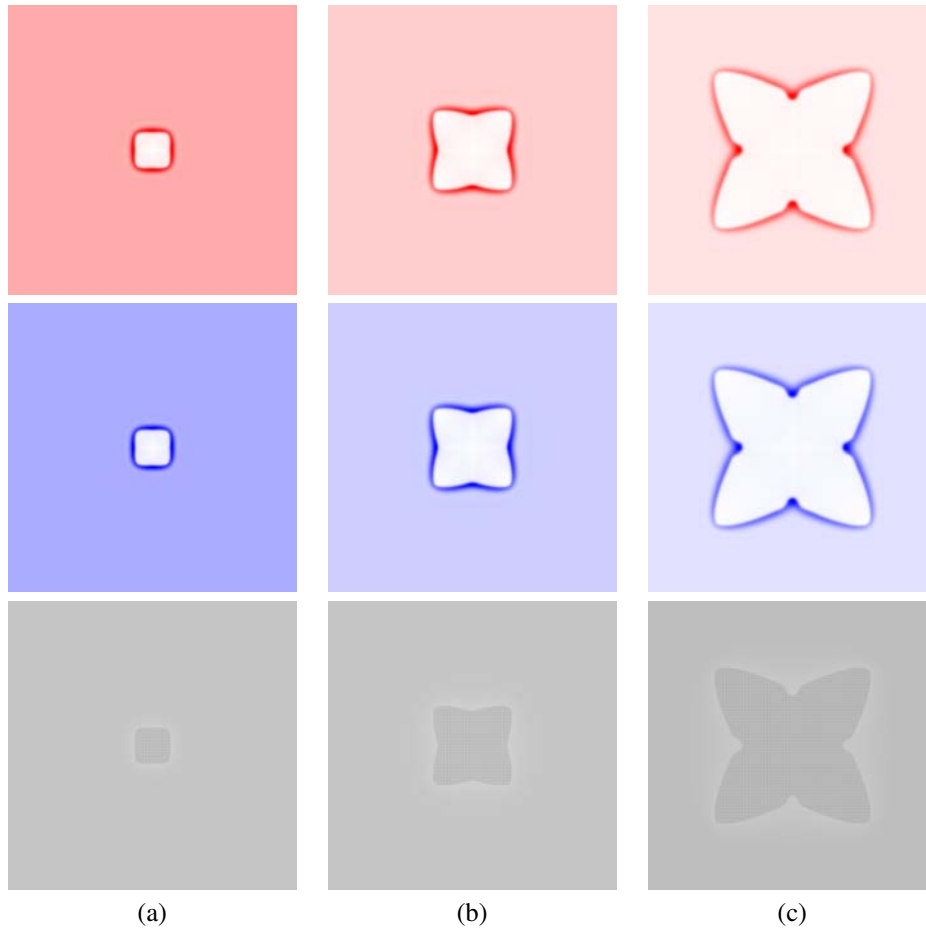
Figure 6.3: Early-time dendritic solidification in a ternary alloy, simulated using the phase diagram of Fig. 6.1(b). The quench temperature is $\sigma = 0.182$ and the initial solute compositions are uniform and set to the alloy averages, $c_{o,A} = 0.1$ and $c_{o,B} = 0.1$. Each Column of images represents a different time during the simulation. The times shown are: (a) 1000 (b) 3000 and (c)7000 iterations. From bottom to top, each row displays the progression of n, c_B and c_A, respectively, with c_A plotted in the color range from white (lowest concentration) to red (highest concentration) and c_B is plotted in the color range from white (lowest concentration) to blue (highest concentration).
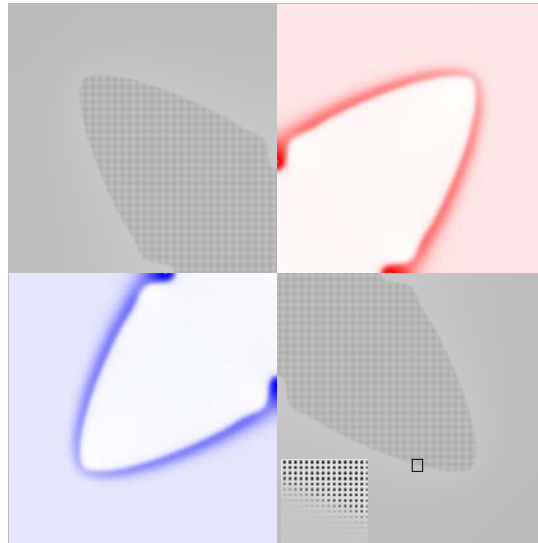
Figure 6.4: Dendritic solidification at time, $t = 10000$, displaying the values of all three fields. The top left and bottom right quadrants show the density field, n. The inset on the bottom right, is a zoomed-in image of the rectangular area marked in black, revealing the structure of the underlying square lattice and density wave structure through the interface. Top right quadrant shows c_A, with colour range white (low concentration) to red (high concentration), while bottom left shows c_B, with colour range white (low concentration) to blue (high concentration). Both show the high solute content at the interface.

system was initialized with an initial circular seed of the α-phase at compositions $c_A = 0.16$ and $c_B = 0.005$, while the remaining liquid was set as to satisfy the lever rule for each solute species. As the system evolves, the seed initially becomes dendritic, as is evident by the emerging four fold symmetry of the crystal. During further growth, because of solute depletion, an instability occurs which causes the finger like growth of the α-phase, admitting subsequent nucleation of the secondary γ-phase in regions where there is depletion of species A. After the emergence and growth of γ, there exists an accumulation zone of A, which then allows a nucleation of α. This process is repeated through out the evolution of the system giving rise to the unique pattern seen in the last frame on the bottom right of Fig. 6.5. It has been suggested that this method of growth; solute depletion (or accumulation), nucleation; solute accumulation (or depletion), nucleation and further growth may be the true mechanism of eutectic formation in alloy systems. In this demonstration, not only is the effect of the correlation function apparent, through emergence of phases as a function of the local composition, but there is evidence of topological defects, elasticity and nucleation. All of which are captured naturally and self-consistently.

6.7   Application to Solute Clustering in Al-Cu-Mg Alloys

Many properties of engineering alloys are typically attained through downstream processing following solidification. These downstream processes typically involve either thermo-mechanical manipulations or heat treatment of the as-cast microstructure. One of the most important aims is to induce certain phase transformations in the as-cast primary solid matrix to help strengthen alloys, a process known as precipitation hardening. In this section we apply the ternary XPFC alloy model to the study of such a process. In particular, we investigate the initial stages solute clustering, the precursor stage of precipitation in Al-Cu-Mg alloys. The aim is to elucidate the interactions of impurities
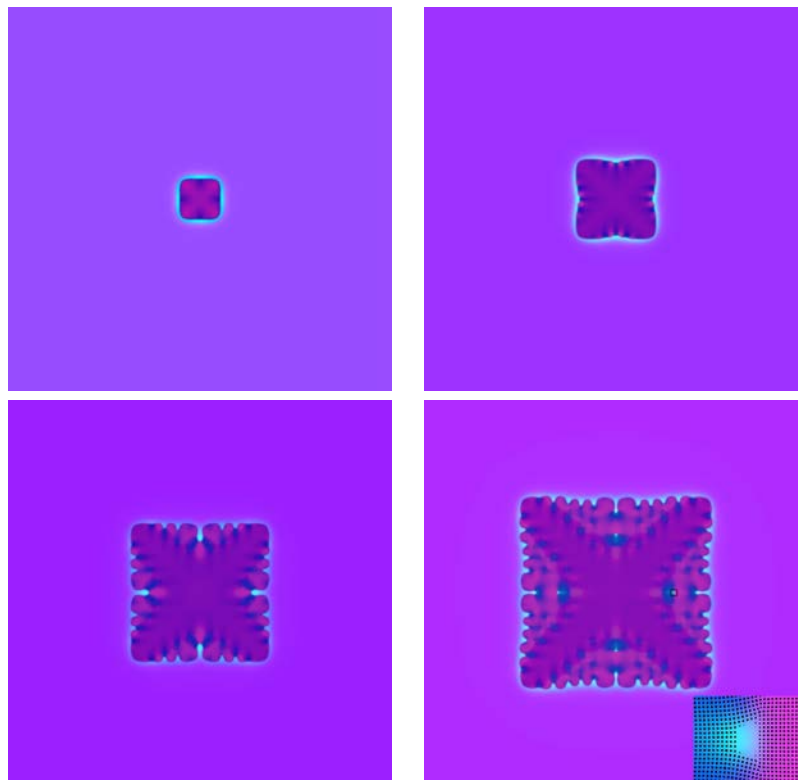
Figure 6.5: Ternary eutectic solidification simulated using the phase diagram of Fig. 6.1(d). The quench temperature is $\sigma = 0.164$ and the initial solute compositions are uniform and set to the alloy averages, $c_{o,A} = 0.6$ and $c_{o,B} = 0.025$. Time evolves from top left image to bottom right. Here, bright purple represents higher concentration values of c_A with additions of c_B, dark blue represents lower concentrations c_A with small additions of c_B, while bright blue regions present relatively moderate amounts of c_A and c_B.

with dislocations and how this alters the nucleation barrier for cluster formation. The main results and features of this work were made possible by the ternary model developed in this thesis. They are presented here, while the full details of the study can be found in Ref. [33].

6.7.1   Numerical Simulation of Early Clustering in Ternary Alloys

Solute clustering/early-stage precipitation simulations were preformed using the equilibrium properties calculated for the $(Al) - \beta - \theta$ system in Figs. 6.2(c) and 6.2(d). Simulations were performed using Eqs. (6.5)-(6.7) on a 2D rectangular mesh, 4096×4096 ($\sim 512 \times 512$ lattice spacings) with grid spacing $\Delta x = 0.125$ and time step $\Delta t = 10$. Dynamical equations were solved semi-implicitly in Fourier space. Inspired from our work on clustering in binary alloys, and recent experimental observations and measurements, initial conditions consisted of distorted single-phase structures, through the introduction of a uniform distribution of dislocations, and a uniform alloy composition everywhere of $c_{o,Cu} = 1.1$ and $c_{o,Mg} = 0.2$ at.%. All simulations were initially solutionized for some time at $\sigma = 0.155$, following which they were quenched/aged at a temperature $\sigma = 0.04$. During ageing, small clusters initially appear with higher Mg and/or Cu-content than that of the matrix. As time progresses, some of these clusters decrease in size and Cu-Mg-content, or vanish entirely. Several stabilize, as shown by the typical stabilized clusters "a" and "b" in Fig. 6.6(a)-(c) and (d)-(f) for Al-1.1Cu and Al-1.1Cu-0.2Mg alloys, respectively. In contrast, for either alloy, when we increase the ageing temperature within the single-phase (Al) region , e.g., $\sigma = 0.145$, no clustering is observed and the initial distortions are removed from the matrix.
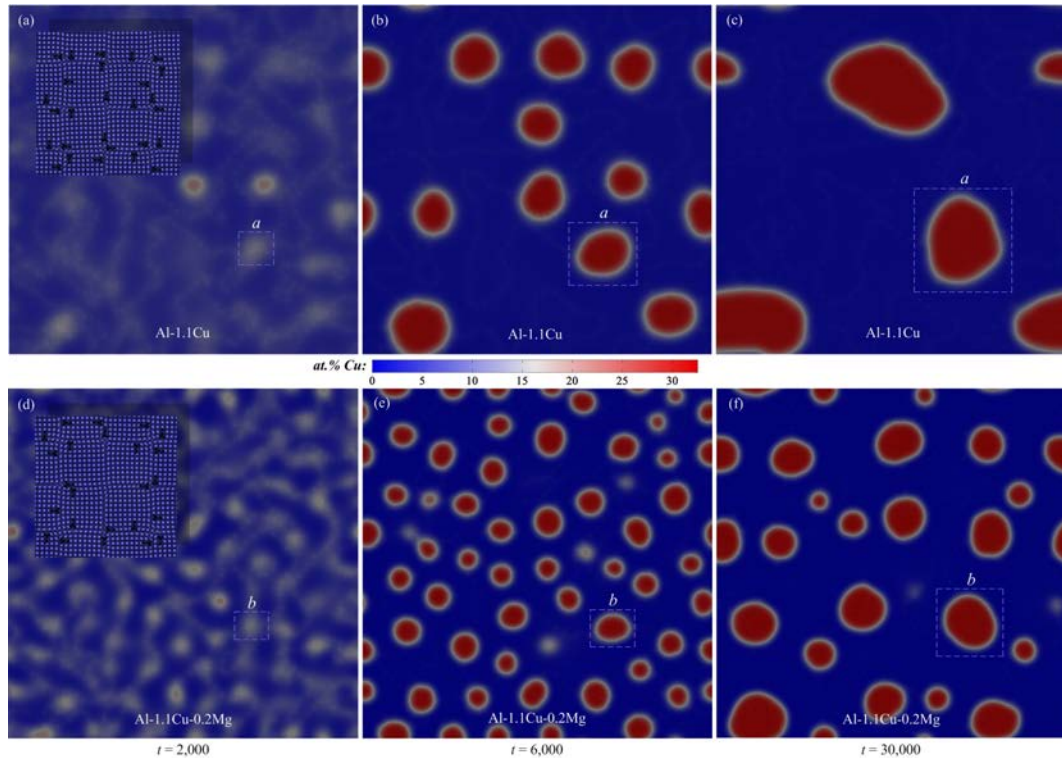
Figure 6.6: Time evolution of clusters in quenched (a)-(c) Al-1.1Cu and (d)-(f) Al-1.1Cu-0.2Mg alloys at $\sigma = 0.04$. The insets in (a) and (d) show the initial distorted/damaged single-phase structures, with dislocations clearly marked in the insets, for each set of simulations.

In Fig. 6.6, we see a marked difference between the different microstructures resulting from

clustering in binary alloys, (a)-(c), compared with that of the ternary alloy, (d)-(f). For the ternary system, it appears that the addition of a third component enhances the clustering kinetics as well as promoting a refinement of the final microstructure. The effect of Mg on clustering is clearly illustrated in Figs. 6.7 and 6.8. The first of the figures, Fig. 6.7, displays the marked effects of Mg on the microstructure, while the latter, Fig.6.8, demonstrates the evolutionary nature of the solute components when Mg is present in the system. In Fig. 6.7, the effective cluster radius (R) is mea-
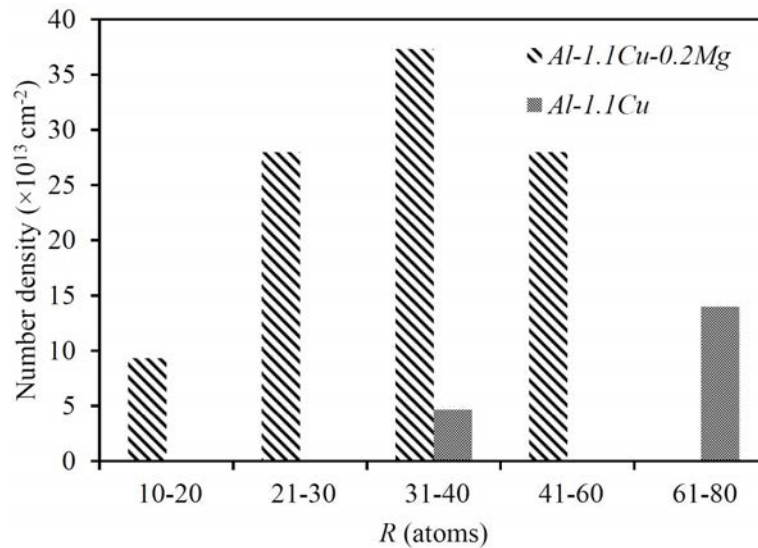
Figure 6.7: Cluster density distribution versus cluster size in solutionized binary Al-1.1Cu and ternary Al-1.1Cu-0.2Mg alloys, plotted at $t = 30,000$.

sured by averaging the concentration field bounded by a predefined threshold. A density/distribution of the number of clusters, is approximated by a normalization of the number of clusters in a given size range within the 2D simulation domain having an effective lattice parameter of a 3D Al-FCC lattice parameter. Figure 6.7 plots the resulting distribution for both a binary alloy and the current ternary alloy. The addition of Mg to the binary alloy, not only increases the number density of clusters, but also shifts the distribution to smaller radii, thereby causing a reduction in the size of observed clusters. This observation is supported by TEM, atom probe and various other experimental investigations in the literature.

The effect of Mg was also examined by observing its evolution, as well as that of Cu, in a typical cluster, "b". We find, from the data of Fig. 6.8, that we have a continuous increase in the Cu-content of cluster "b" as a function of the effective radius towards its equilibrium value for the θ-phase. For Mg and the Mg/Cu ratio, there is an increase until a maximum, after which there is a continuous drop to the respective equilibrium values. From the data of Fig. 6.8, the formation of Cu-rich clusters can be considered as occurring in a two stage process. Initially, both Cu- and Mg-content increase continuously in early clusters until the cluster reaches a critical size. The second stage consists of a depletion of the Mg-content past the critical cluster size, while attracting more Cu for continuous growth until the cluster has reached equilibrium according to the phase diagram. This occurs as the growing cluster releases more stress, whereby it is allowed to reach its equilibrium phase, which notably contains less Mg than the highly strained Cu-Mg co-cluster.
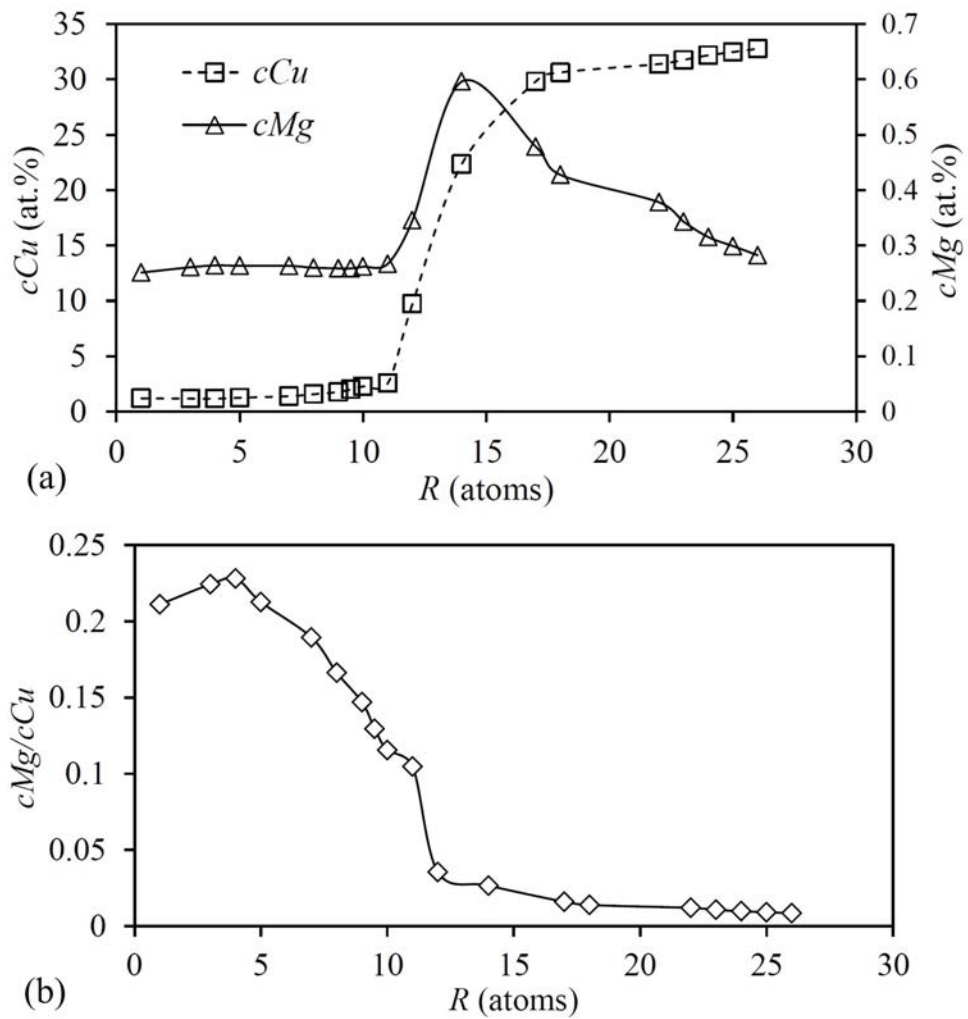
Figure 6.8: Composition evolution of Mg, (a), and the ratio of solute compositions Mg/Cu, (b), for typical cluster "b" from Fig. 5.8. $R = 0$ defines the centre of the cluster.

6.7.2   Quantitative Analysis of Clustering

In the previous chapter, when we applied the XPFC binary alloy model to clustering in Al-Cu alloys, we presented a quantitative analysis using the energetics of the system. An analogous analysis using the total work of formation (numerical) is employed here. From Section 5.7, the equation for the total work of formation augmented for ternary alloys takes the form

$$\Delta G_{tot} = \int_V \Omega - \int_V \Omega^b$$
$$= \int_V [f - \mu_{Cu}c_{Cu} - \mu_{Mg}c_{Mg} - \mu_n n] - \int_V [f^b - \mu_{Cu}^b c_{Cu}^b - \mu_{Mg}^b c_{Mg}^b - \mu_n^b n^b], \quad (6.11)$$

where the superscript b denotes bulk quantities, μ_ν are chemical potentials with ν being one of the fields, and V is the volume which encapsulates clusters "a" and "b" (i.e., boxes marked in Figs. 6.6(c) and Fig. 6.6(f)). A numerical calculation examining typical clusters, labeled "a" and "b" from Fig. 6.6 yields the data plotted in Fig. 6.9. As can be seen from the plot, the total work
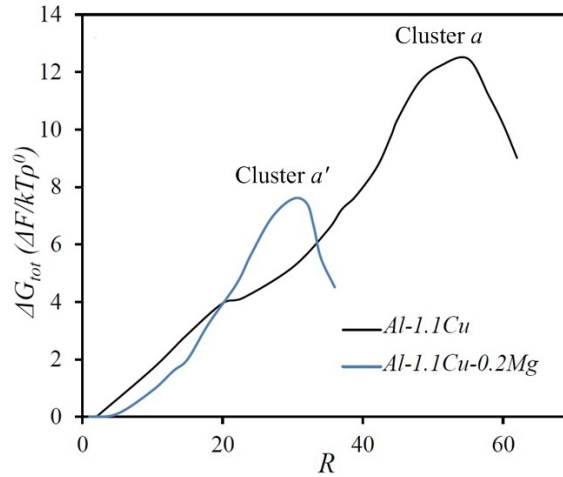
Figure 6.9: The variation of numerically evaluated total energy, ΔG_{tot}, due to the formation of clusters "a" and "a'", within the boxes marked on the images shown in Fig. 6.6(a)-(c) and (d)-(f), respectively.

of formation increases locally with the growth of clusters to some maximum value, i.e., until the clusters become stable, and then decreases. This trend is quite indicative of a nucleation process as the peak in the plot represents an energy barrier. While this increase and subsequent decrease of the total work of formation is local, we note that the entire system energy is driven to minimization. In other words, while the energy may increase locally due to the attraction of dislocations and solute atoms, there might also be other parts in the system where there is a depletion of solute and annihilation of dislocations.

Experiments in quenched/aged Al-Cu and Al-Cu-Mg alloys [95, 97, 102] have found increasing evidence that the interaction of ternary impurities and quenched-in defects, such as dislocations [103], dynamically reduce the local nucleation barrier for precipitation at locations in the matrix. We have also found that the addition of Mg to an Al-1.1Cu alloy promotes clustering and refinement of the final microstructure, as seen in the simulation data of Fig. (6.6). The clustering phenomenon observed in these simulations can be attributed to the propensity for solute segregation to defects and surrounding areas to relieve stresses induced by the presence of said defects, in this case dislocations. As more solute aggregates to dislocations, the size of the cluster increases but the

75

structural nature of the cluster also begins to approach that of the next nearest stable solid phase. As this process continues and the ever growing cluster attracts more solute, it creates additional stresses in the surrounding matrix. This in turn draws nearby dislocations to the cluster in attempts to relieve these additional stresses caused by solute accumulation[||].

6.8   Summary and Conclusions

This chapter reported on the XPFC ternary alloy model, attained by reducing the multi-component energy of Chapter 4. To our knowledge this is the first PFC model that has explored a system containing more than two components. The free energy of the system was discussed as well as the dynamics. We followed with static, i.e., equilibrium, calculations of the system by examining a generic ternary alloy exhibiting eutectics, both binary and ternary. Secondly, we examined the mapping of the ternary model, qualitatively, to the Al-rich portion of the Al-Cu-Mg phase diagram.

This multi-component PFC model is able to capture the complex kinetics of solidification and elastic and plastic effects on solid-state processes. To this end the kinetic properties of model were demonstrated for dendritic and eutectic solidification. The model was then applied to the study of early clustering and precipitate growth in Al-Cu-Mg alloys. The results of our work, more comprehensive in Ref. [33], seem to support recent experiments on the elusive mechanisms of the early stages of clustering and precipitation. Particularly, through clustering simulations and analysis of system energetics, that the addition of trace amounts of Mg to Binary Al-1.1Cu promotes clustering and grain refinement. Such simulations are currently outside the feasibility of other atomistic or mean field modeling formalisms, however are well suited using the current XPFC ternary model.

The dynamic demonstrations and applications in this chapter has demonstrated some important thermodynamic and kinetic properties of the model. Moreover, aside from the quantitative and self-consistent nature of the model, it is particularly simple to operate numerically. It is expected that this model can thus be used to elucidate the role of multiple solutes in phenomena governed by atomic-scale elasticity and defects operating on diffusional time scales.

The next chapter explores how to derive complex order-parameter (amplitude), phase-field type, models from PFC models through so-called coarse-graining methods. Such models affords the opportunity to bring the self-consistent and quantitative nature of the PFC to larger size scales.

[||]The interested reader is should consult Ref. [33] for a more in-depth study and description of clustering in ternary alloys.

Chapter 7

Multi-Scale Modelling: Amplitude Expansions of Phase-Field-Crystal Models

The phase-field-crystal (PFC) methodology was introduced to create a bridge between the atomistic and traditional phase-field (PF) regimes. The latter of which is typically based on phenomenological free energy forms. Through coarse-graining methods, it has been demonstrated that the form of traditional PF models can also be derived, albeit with complex order-parameters, from PFC models. Such coarse-graining procedures can be seen to provide a connected path from the microscopic properties of the PFC formalism to the traditional PF methods. This has an obvious advantage of providing a self-consistent road map for deriving the form of more complex PF models that couple order-parameters to elastic [89, 67], temperature [**?**], magnetic [**?**] and polarization fields. It also allows a way to understand how and where microscopic parameters enter mesoscale theories. In this chapter, we end the research component of this dissertation by introducing a novel Fourier method in deriving amplitude models, from truncated classical density functional theories. As an example of the method, we apply it to the single component structural PFC model of Greenwood *et. al.* After derivation of the model, we demonstrate its use for some choice phenomena.

7.1   Motivation

Traditional phase-field methods are capable of operating on length scales considerably larger than that of the phase-field-crystal approach. Through the use of adaptive mesh techniques [104, 105, **?**], the accessible length scales increase even further. Having a basis in phenomenological theory, the self-consistent description of various atomistic scale effects is severely lacking in PF models. However, PFC models naturally capture atomistic scale features.

Coarse-graining approaches have recently shown that PFC-type models can be used to derive the form of traditional PF models, expressed, however, in the form of complex order-parameters, which makes it possible to simulate different crystal orientations and defect structures on meso-scopic length and time scales. These amplitude models, remarkably, retain many salient atomistic level phenomena, making them prime candidates for multiple scale modelling of microstructure phenomena. Recent amplitude descriptions have been used to describe surface energy, and anisotropy, of crystal-melt interfaces in pure materials and alloys [60, 61, 62], solidification of multiple crystallites using an adaptive mesh [106], island and quantum dot formation [107], segregation and alloy solidification [89, 108] and grain boundary premelting [109, 93]. However, these for the most part,

have involved pure materials or binary alloys where both elements had the same crystal structure, i.e., that employ a single peaked correlation function.

The purpose of this chapter is to apply a new coarse-graining approach to the recent XPFC model. In so doing, our coarse-graining technique is shown to be general enough to be applicable to any PFC model. Recent work with coarse-grained PFC models suggests that an amplitude model capable of describing multiple crystal structures and elasto-plastic effects will be valuable in elucidating the atomistic scale interactions of processes at the mesoscale, as well as motivating better forms of mesoscale continuum models, such as PF models. Here, we present the amplitude expansion of the XPFC model of a pure material by Greenwood *et al.* [19, 20], for 2D structures. At the core of our approach is a Fourier method applied to the excess term, coupled to the volume-averaging technique described in Refs. [61, 62]. After derivation of the corresponding coarse-grained free energy functional, we perform dynamic simulations illustrating peritectic solidification and solid-solid interactions in grain growth between differing crystal structures.

The chapter is organized as follows. Section 7.2 goes through the various steps of generating a corresponding complex amplitude free energy functional, starting with the construction of an appropriate density expansion, then a brief remark on the volume-averaging technique and finally the coarse-graining of the XPFC energy. The dynamics of the amplitude set of equations are discussed in section 7.4, followed by numerical illustrations of the model in section 7.5.

7.2 Amplitude Model Derivation: 2D Square-Triangle Structures

Recently, numerous works have been published that perform amplitude expansions, particularly of PFC models. The main approaches that have been used are: the multiple scale analysis [110, 89, 67], volume-averaging method [61, 62] and the renomarlization group (RG) approach [111, 112, 113, 106], with the multiple scale method being the most widely applied across disciplines. Older works where these expansions have been performed directly on CDFT models, like the work of Haymet and Oxtoby [23, 24] and Lakshmi*et al.* [114] fall under the volume-averaging method. Others still, e.g. Kubstrup *et al.* [115] fall under the multiple scale analysis. The central theme in all these techniques is that the density can be separated into so-called "fast" length scales, where the density oscillates rapidly, and "slow" length scales, where the amplitudes of the oscillations vary slowly, with respect to the rapidly varying oscillation of the density. Beyond this, each method has its own additional underlying assumptions and approximations.

A noteworthy consideration is the validity or accuracy of the various methods in arriving at the same self consistent system of equations. Namely, the multiple scale analysis and RG methods operate on the PFC equations of motion, after which the coarse-grained free energy functional is derived. The volume-averaging method can operate on both the PFC energy functional and the dynamical equations, however it has been implemented for the most part at the energy functional level of the PFC or CDFT energy functionals. A point of criticism against the volume-averaging method, has been the lack of a covariant gradient operator [116] in the amplitude equations. In previous implementations, a second order expansion was taken of the "slow" variables (i.e., the amplitudes) [61, 62]. In particular, while to second order, surface energy calculations can be performed quite quantitatively, dynamic simulations are fixed to certain orientations. It has been shown [117], that an expansion to at least fourth order is necessary to recover the lowest order covariant gradient operator.

7.2.1 Density Expansion in Two Lattices

The PFC suite of models, for a pure material, contain only a single dimensionless density field, n. A self-consistent method of defining a density expansion which incorporates multiple crystal

structures is nontrivial. For the XPFC, in 2D, these crystal structures are, crystals of triangular and square symmetry. Kubstrup *et al.* [115] in a study of pinning effects between fronts of hexagon (i.e., triangle) and square phases, have proposed a construction through which variable phases can be described by a single expansion definition. This density expansion, for the XPFC model, can be written as,

$$n(\mathbf{r}) = n_o(\mathbf{r}) + \sum_j^6 A_j(\mathbf{r})e^{i\mathbf{k}_j \cdot \mathbf{r}} + \sum_m^6 B_m(\mathbf{r})e^{i\mathbf{q}_m \cdot \mathbf{r}} + c.c., \tag{7.1}$$

where $n_o(\mathbf{r})$ is the dimensionless average density and is a "slow" variable, $c.c.$ denotes the complex conjugate, $\{A_j\}$ represent the amplitudes describing the first mode of our structures, while all $\{B_m\}$ represent the amplitudes for the second mode and like the dimensionless average density, the amplitudes are also "slow" variables. Following Kubstrup *et al.*, the density expansion we construct can
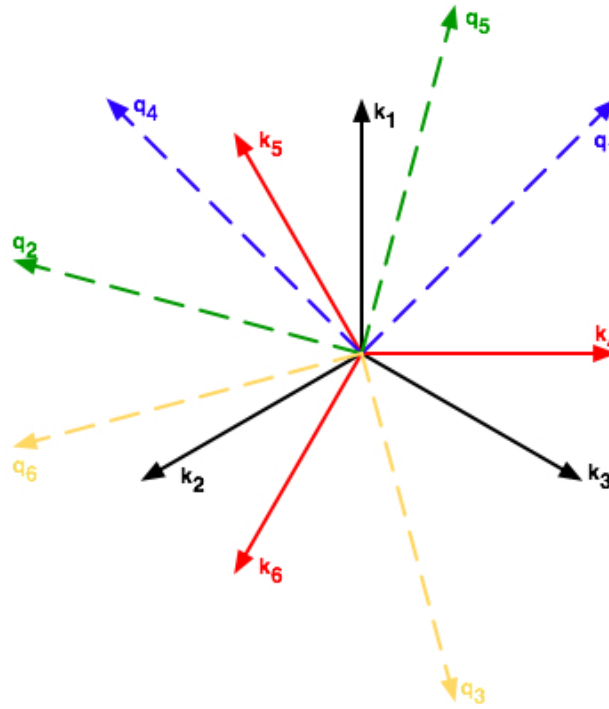
Figure 7.1: Schematic representation of, mis-oriented by 30 degrees, the vectors $\mathbf{k}_1, \mathbf{k}_2, \mathbf{k}_3$ and $\mathbf{k}_4, \mathbf{k}_5, \mathbf{k}_6$ form a resonant set and compromise two triangular lattices, while vectors $\mathbf{k}_1$ and $\mathbf{k}_4$ and similar permutations are orthogonal forming the first mode of the square correlation kernel. The other set of vectors, $\{\mathbf{q}_m\}$ dashed-dotted, correspond to the second mode of the correlation kernel necessary to stabilize the square structure in the XPFC, and are formed from a linear combination of the orthogonal set of the first mode. A more thorough description is included in the text.

be schematically inferred from Fig. 7.1 in terms of the required set of reciprocal lattice vectors. Figure 7.1 represents the reciprocal lattice vectors that enter the density expansion in Eq. (7.1), having two interlaced triangular structures mis-oriented by $30°$, i.e., vectors $\mathbf{k}_1, \mathbf{k}_2, \mathbf{k}_3$ and $\mathbf{k}_4, \mathbf{k}_5, \mathbf{k}_6$ each form a triangular lattice, respectively. It will be useful in what follows that a so-called property of resonance is satisfied by these two vector sets. Resonance between density waves, is satisfied when $\mathbf{k}_1 + \mathbf{k}_2 + \mathbf{k}_3 = 0$ and $\mathbf{k}_4 + \mathbf{k}_5 + \mathbf{k}_6 = 0$. The square structure can then be partly constructed from combinations of the reciprocal lattice vectors of the two triangular sets. For example, $\mathbf{k}_1$ and $\mathbf{k}_4$

(which are orthogonal, i.e., $\mathbf{k}_1 \cdot \mathbf{k}_4 = 0$) represent the first mode of a square lattice, while the second mode of the square can be constructed from a linear combination from the first, i.e, $\mathbf{q}_1 = \mathbf{k}_1 + \mathbf{k}_4$ and $\mathbf{q}_4 = \mathbf{k}_1 - \mathbf{k}_4$. Analogous definitions can be made for the second and third set of square lattices which arise from the two interlaced triangular lattices. In total, the density expansion for a system described by the vectors of Fig. 7.1 amount to 12 vectors and therefore 12 complex amplitudes.
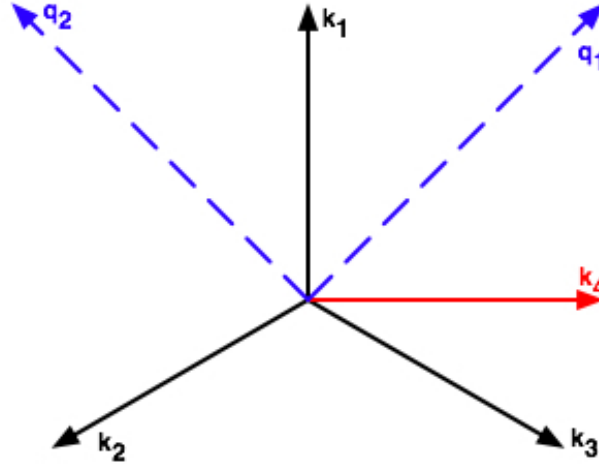
Figure 7.2: Second Schematic representation of the reciprocal set of basis vectors which comprise a density simultaneously describing crystals with square and triangular symmetry respectively. Vectors $\mathbf{k}_1, \mathbf{k}_2, \mathbf{k}_3$ form a resonant set and compromise a single triangular lattice. Vectors $\mathbf{k}_1$ and $\mathbf{k}_4$ are orthogonal forming the first mode of the correlation kernel. The other set of vectors, $\{\mathbf{q}_m\}$ dashed-dotted, comprise the second mode of the square correlation kernel.

The expansion described by Eq. (7.1) and the vectors of Fig. 7.1, each corresponding to one of the 12 amplitudes may prove to be intractable or at the least tedious and cumbersome to deal with. A simpler more intuitive expansion, is also proposed here as a comparison. This is illustrated by the reciprocal lattice vectors of Fig. 7.2. Unlike the previous expansion, this expansion requires 6 vectors and hence 6 amplitudes. At first glance, there seems to be a limited number of degrees of freedom afforded to us by an expansion of this kind. It is not known *a priori* what differences exist between the two expansions. The nuances that may exist between the two expansions may be ascertained through numerical simulations. For convenience, we will be using this latter expansion in our derivation to follow. In Appendix C.3, we also report on the complex amplitude model derived from the 12 amplitude expansion described by Eq. (7.1). The simpler density expansion is written as

$$n(\mathbf{r}) = n_o(\mathbf{r}) + \sum_j^4 A_j(\mathbf{r})e^{i\mathbf{k}_j \cdot \mathbf{r}} + \sum_m^2 B_m(\mathbf{r})e^{i\mathbf{q}_m \cdot \mathbf{r}} + c.c. \tag{7.2}$$

7.2.2 Volume-Averaging Technique for Coarse Graining

As mentioned in the previous section, the amplitudes $\{A_j\}$ and $\{B_m\}$ along with the dimensionless average density n_o, are all slowly varying on atomic scales. After inserting the density expansion of Eq. (7.2) into the XPFC free energy terms of Eq. (2.42) (in Section 2.2.5), to lowest order the terms that will survive the coarse-graining procedure are those where the oscillating exponential phase factors vanish. In particular, under coarse-graining, the free energy effectively becomes a series of terms with "slow" variables multiplying phase factors of the form $e^{i\Delta Q_l \cdot \mathbf{r}}$, where ΔQ_l are sums or

differences in the reciprocal lattice vectors. As in all coarse-graining approaches, the lowest order approximation, i.e., so-called "quick and dirty" approach [111], amounts to the situation where the only surviving coarse-grained terms result from all $\Delta Q_l \equiv 0$. This is the standard condition from the symmetry requirement of translational invariance of the total free energy [118].

Formally, the volume-averaging method can be performed using a convolution operator [119, 61], defined by,

$$\langle f(\mathbf{r}) \rangle_V \equiv \int_{-\infty}^{\infty} d\mathbf{r}' f(\mathbf{r}') \xi_V(\mathbf{r} - \mathbf{r}'), \tag{7.3}$$

where $f(\mathbf{r}')$ is the function being coarse-grained, for our purposes collections of "slow" variables or "slow" variables multiplied by phase factors, and V is the coarse-graining volume, i.e., typically the volume of a unit cell. The function ξ_V in the integrand of Eq. (7.3) is a smoothing function that is normalized to unity, i.e.,

$$\int_{-\infty}^{\infty} d\mathbf{r} \, \xi_V(\mathbf{r} - \mathbf{r}') \equiv 1. \tag{7.4}$$

In the long wavelength limit, $L_{slow} \gg L \gg a$, where $L \sim V^{1/d}$, in d-dimensions, while L_{slow} is the length scale of variation of the "slow" variables (i.e. microstructural features), and a is the equilibrium lattice spacing. This condition implies that the function $\xi_V(\mathbf{r})$ varies on dimensions much larger than the lattice constant, e.g. $a = 2\pi/|\mathbf{k}_j|$, but much less than the length scale of variation of the average density and amplitudes. Equation (7.3) is formally applied by changing the dependent variable in the free energy functional from $\mathbf{r}$ to $\mathbf{r}'$, multiplying the resulting free energy by the left hand side of Eq. (7.4) (i.e., 1) and inverting the order of integration, thus arriving at a series of terms of the form of Eq. (7.3). Equation (7.3) defines a noninvertible limiting procedure that can be used to average a function over some volume. The reader is referred to Refs. [119, 61, 31] and Appendix C for greater detail about the application of the volume-averaging convolution operator.

7.2.3 Coarse-Graining the Ideal Term

Inserting the density expansion of Eq. (7.2) into the ideal portion, ΔF_{id} (Section 2.2.5), of the XPFC free energy, and coarse-graining, via the convolution operator as described in the preceding section, yields to lowest order in amplitudes and the average density,

$$\frac{F_{id}^{cg}}{k_B T \rho_o V} = \int d\mathbf{r} \left\{ \frac{n_o^2}{2} - \eta \frac{n_o^3}{6} + \chi \frac{n_o^4}{12} + \left(1 - \eta \, n_o + \chi \, n_o^2\right) \left(\sum_j^4 |A_j|^2 + \sum_m^2 |B_m|^2 \right) \right.$$

$$- (\eta - 2\chi n_o) \left[A_1 A_2 A_3 + A_1^* A_4^* B_1 + A_1 A_4^* B_2^* + c.c. \right] + \frac{\chi}{2} \left[\sum_j^4 A_j^2 (A_j^*)^2 + \sum_m^2 B_m^2 (B_m^*)^2 \right]$$

$$+ 2\chi \left[\left(\sum_j^4 \sum_{m>j}^4 |A_j|^2 |A_m|^2 + \sum_j^4 \sum_m^2 |A_j|^2 |B_m|^2 + |B_1|^2 |B_2|^2 \right) \right]$$

$$+ \chi \left[2A_2^* A_3^* A_4^* B_2^* + 2A_2^* A_3^* A_4 B_1^* + A_1^2 B_1^* B_2^* + A_4^2 B_1^* B_2 + c.c. \right] \bigg\}, \tag{7.5}$$

where "*" denotes the complex conjugate. As alluded to earlier, the correlation-containing excess term has received some attention in the coarse-graining of PFC models. In the following section, we introduce a general Fourier space method to treat this term in the context of the present XPFC model.

7.2.4   Coarse-Graining the Excess Term

We first rewrite the correlation kernel in its Fourier series representation, i.e.,

$$C_2(|\mathbf{r} - \mathbf{r}'|) = \int d\mathbf{k}\, \hat{C}_2(|\mathbf{k}|)\, e^{i\mathbf{k}\cdot\mathbf{r}}\, e^{-i\mathbf{k}\cdot\mathbf{r}}. \tag{7.6}$$

The convolution term, $\mathcal{G}$, the integral over $d\mathbf{r}'$ (Section 2.2.5), in the free energy involving the excess term then becomes,

$$\begin{aligned}
\mathcal{G} &= \int d\mathbf{r}' C_2(|\mathbf{r} - \mathbf{r}'|)n(\mathbf{r}') \\
&= \int d\mathbf{r}' \int d\mathbf{k}\, \hat{C}_2(|\mathbf{k}|)e^{i\mathbf{k}\cdot\mathbf{r}}\, e^{-i\mathbf{k}\cdot\mathbf{r}'}\, n(\mathbf{r}').
\end{aligned} \tag{7.7}$$

Next we take the Taylor series expansion of the correlation function around $\mathbf{k} = 0^*$, i.e., the infinite wavelength mode of the correlation, to all orders. This expansion can be compactly written as,

$$\hat{C}_2(|\mathbf{k}|) = \sum_{l=0}^{\infty} \frac{1}{l!}(\mathbf{k})^l \frac{\partial^l \hat{C}_2}{\partial \mathbf{k}^l}\bigg|_{\mathbf{k}=0}, \tag{7.8}$$

where l enumerates the order of the terms in the expansion. This functional Taylor series expansion is formally exact, as it goes to all orders. It is valid provided the correlation function is some well-behaved function of $\mathbf{k}$. Substituting the density expansion, Eq. (7.2), into the convolution term of the free energy and employing the definition of the Fourier transform yields

$$\begin{aligned}
\mathcal{G} &= \int d\mathbf{k} \sum_{l=0}^{\infty} \vartheta_l(\mathbf{k})^l \hat{n}_o(\mathbf{k})e^{i\mathbf{k}\cdot\mathbf{r}} \\
&+ \int d\mathbf{k} \sum_{l=0}^{\infty} \vartheta_l(\mathbf{k})^l \sum_{j}^{4} \hat{A}_j(\mathbf{k} - \mathbf{k}_j)e^{i\mathbf{k}\cdot\mathbf{r}} \\
&+ \int d\mathbf{k} \sum_{l=0}^{\infty} \vartheta_l(\mathbf{k})^l \sum_{m}^{2} \hat{B}_m(\mathbf{k} - \mathbf{q}_m)e^{i\mathbf{k}\cdot\mathbf{r}} + c.c.,
\end{aligned} \tag{7.9}$$

where we have made the following definition,

$$\vartheta_l = \frac{1}{l!} \frac{\partial^l \hat{C}_2}{\partial \mathbf{k}^l}\bigg|_{\mathbf{k}=0} \tag{7.10}$$

along with the Fourier components,

$$\hat{n}_o(\mathbf{k}) = \int d\mathbf{r}' n_o(\mathbf{r}')e^{-i\mathbf{k}\cdot\mathbf{r}'}$$

$$\hat{A}_j(\mathbf{k} - \mathbf{k}_j) = \int d\mathbf{r}' A_j(\mathbf{r}')e^{i\mathbf{k}_j\cdot\mathbf{r}'}e^{-i\mathbf{k}\cdot\mathbf{r}'}$$

$$\hat{B}_m(\mathbf{k} - \mathbf{q}_m) = \int d\mathbf{r}' B_m(\mathbf{r}')e^{i\mathbf{q}_m\cdot\mathbf{r}'}e^{-i\mathbf{k}\cdot\mathbf{r}'}. \tag{7.11}$$

Next we re-sum the correlation function for the average density part of the convolution term in Eq. (7.9) and make consecutive change of variables, i.e., $\mathbf{k}' = \mathbf{k} - \mathbf{k}_j$ and then $\mathbf{k}' = \mathbf{k} - \mathbf{q}_m$, for

---

*It is tacitly assumed in doing so that the expansion, Eq. (7.8), is convergent over a large enough window of $\mathbf{k}$-values.

both the second and third terms in Eq. (7.9), respectively. Following these steps, we arrive at

$$
\mathcal{G} = \left[\hat{C}_2(|\mathbf{k}|)\hat{n}_o(\mathbf{k}) \right]_{\mathbf{r}} + \sum_j^4 \int d\mathbf{k}' \sum_{l=0}^{\infty} \vartheta_l(\mathbf{k}' + \mathbf{k}_j)^l \, \hat{A}_j(\mathbf{k}') e^{i\mathbf{k}' \cdot \mathbf{r}} e^{i\mathbf{k}_j \cdot \mathbf{r}} \tag{7.12}
$$

$$
+ \sum_m^2 \int d\mathbf{k}' \sum_{l=0}^{\infty} \vartheta_l(\mathbf{k}' + \mathbf{q}_m)^l \hat{B}_m(\mathbf{k}') e^{i\mathbf{k}' \cdot \mathbf{r}} e^{i\mathbf{q}_m \cdot \mathbf{r}}
$$

$$
+ c.c.
$$

Applying the definition of the Fourier transform to the second and third terms on the RHS of Eq. (7.12) yields,

$$
\mathcal{G} = \left[\hat{C}_2(|\mathbf{k}|)\hat{n}_o(\mathbf{k}) \right]_{\mathbf{r}} + \sum_j^4 e^{i\mathbf{k}_j \cdot \mathbf{r}} \left[\hat{C}_2(|\mathbf{k} + \mathbf{k}_j|)\hat{A}_j(\mathbf{k}) \right]_{\mathbf{r}} \tag{7.13}
$$

$$
+ \sum_m^2 e^{i\mathbf{q}_m \cdot \mathbf{r}} \left[\hat{C}_2(|\mathbf{k} + \mathbf{q}_m|)\hat{B}_m(\mathbf{k}) \right]_{\mathbf{r}} + c.c.,
$$

where $[\ ]_{\mathbf{r}}$ denotes the inverse Fourier transform. Equation (7.13) represents the total convolution term of the excess free energy. To complete the coarse-graining of the excess term, we multiply the convolution term in Eq. (7.13) by the expansion of the density field, i.e., $n\,\mathcal{G}$. This results in,

$$
\frac{\Delta F_{ex}}{k_B T \rho^{\ell}} = \tag{7.14}
$$

$$
- \frac{n_o}{2} \left[\hat{C}_2(|\mathbf{k}|)\hat{n}_o(\mathbf{k}) \right]_{\mathbf{r}} - \frac{n_o}{2} \sum_j^4 e^{i\mathbf{k}_j \cdot \mathbf{r}} \left[\hat{C}_2(|\mathbf{k} + \mathbf{k}_j|)\hat{A}_j(\mathbf{k}) \right]_{\mathbf{r}} - \frac{n_o}{2} \sum_m^2 e^{i\mathbf{q}_m \cdot \mathbf{r}} \left[\hat{C}_2(|\mathbf{k} + \mathbf{q}_m|)\hat{B}_m(\mathbf{k}) \right]_{\mathbf{r}}
$$

$$
- \frac{n_o}{2} \sum_j^4 e^{-i\mathbf{k}_j \cdot \mathbf{r}} \left[\hat{C}_2(|\mathbf{k} - \mathbf{k}_j|)\hat{A}_j(-\mathbf{k}) \right]_{\mathbf{r}} - \frac{n_o}{2} \sum_m^2 e^{-i\mathbf{q}_m \cdot \mathbf{r}} \left[\hat{C}_2(|\mathbf{k} - \mathbf{q}_m|)\hat{B}_m(-\mathbf{k}) \right]_{\mathbf{r}}
$$

$$
- \frac{1}{2} \sum_j^4 A_j e^{i\mathbf{k}_j \cdot \mathbf{r}} \left[\hat{C}_2(|\mathbf{k}|)\hat{n}_o(\mathbf{k}) \right]_{\mathbf{r}} - \frac{1}{2} \sum_j^4 \sum_l^4 A_j e^{i(\mathbf{k}_j + \mathbf{k}_l) \cdot \mathbf{r}} \left[\hat{C}_2(|\mathbf{k} + \mathbf{k}_l|)\hat{A}_l(\mathbf{k}) \right]_{\mathbf{r}}
$$

$$
- \frac{1}{2} \sum_j^4 \sum_m^2 A_j e^{i(\mathbf{k}_j + \mathbf{q}_m) \cdot \mathbf{r}} \left[\hat{C}_2(|\mathbf{k} + \mathbf{q}_m|)\hat{B}_m(\mathbf{k}) \right]_{\mathbf{r}} - \frac{1}{2} \sum_j^4 \sum_l^4 A_j e^{i(\mathbf{k}_j - \mathbf{k}_l) \cdot \mathbf{r}} \left[\hat{C}_2(|\mathbf{k} - \mathbf{k}_l|)\hat{A}_l(-\mathbf{k}) \right]_{\mathbf{r}}
$$

$$
- \frac{1}{2} \sum_j^4 \sum_m^2 A_j e^{i(\mathbf{k}_j - \mathbf{q}_m) \cdot \mathbf{r}} \left[\hat{C}_2(|\mathbf{k} - \mathbf{q}_m|)\hat{B}_m(-\mathbf{k}) \right]_{\mathbf{r}} - \frac{1}{2} \sum_m^2 B_m e^{i\mathbf{q}_m \cdot \mathbf{r}} \left[\hat{C}_2(|\mathbf{k}|)\hat{n}_o(\mathbf{k}) \right]_{\mathbf{r}}
$$

$$
- \frac{1}{2} \sum_m^2 \sum_j^4 B_m e^{i(\mathbf{q}_m + \mathbf{k}_j) \cdot \mathbf{r}} \left[\hat{C}_2(|\mathbf{k} + \mathbf{k}_j|)\hat{A}_j(\mathbf{k}) \right]_{\mathbf{r}} - \frac{1}{2} \sum_m^2 \sum_l^2 B_m e^{i(\mathbf{q}_m + \mathbf{q}_l) \cdot \mathbf{r}} \left[\hat{C}_2(|\mathbf{k} + \mathbf{q}_l|)\hat{B}_l(\mathbf{k}) \right]_{\mathbf{r}}
$$

$$
- \frac{1}{2} \sum_m^2 \sum_j^4 B_m e^{i(\mathbf{q}_m - \mathbf{k}_j) \cdot \mathbf{r}} \left[\hat{C}_2(|\mathbf{k} - \mathbf{k}_j|)\hat{A}_j(-\mathbf{k}) \right]_{\mathbf{r}} - \frac{1}{2} \sum_m^2 \sum_l^2 B_m e^{i(\mathbf{q}_m - \mathbf{q}_l) \cdot \mathbf{r}} \left[\hat{C}_2(|\mathbf{k} - \mathbf{q}_l|)\hat{B}_l(-\mathbf{k}) \right]_{\mathbf{r}}
$$

$$
+ c.c.
$$

Coarse-graining, after the application of the convolution operator in Eq. (7.3), leads to lowest order in amplitudes and the average density,

$$\frac{\Delta F_{ex}}{k_B T \rho^\ell V} = -\frac{n_o}{2} \left[\hat{\xi}_V(\mathbf{k}) \hat{C}_2(|\mathbf{k}|) \hat{n}_o(\mathbf{k}) \right]_{\mathbf{r}} - \frac{1}{2} \sum_j^4 A_j^* \left[\hat{C}_2(|\mathbf{k} + \mathbf{k}_j|) \hat{A}_j(\mathbf{k}) \right]_{\mathbf{r}} \tag{7.15}$$

$$- \frac{1}{2} \sum_m^2 B_m^* \left[\hat{C}_2(|\mathbf{k} + \mathbf{q}_m|) \hat{B}_m(\mathbf{k}) \right]_{\mathbf{r}} + c.c.,$$

where $\hat{\xi}_V$ is a convolution operator, in Fourier space, that cuts off $\hat{C}_2$ oscillations beyond its $\mathbf{k} = 0$ peak. The explicit derivation of this term is discussed in Section 7.3.

Several things are worth noting in Eq. (7.15). It becomes evident that the rotational invariance nature of a system, afforded through the covariant gradient operator in real space, is manifested here in the re-summed correlation kernel, which has as input a shifted wavenumber for the respective modes being considered. This shifted wavenumber samples low-$\mathbf{k}$ value deviations (long wavelength limit) around the peaks of the original correlation function. Essentially treating each reciprocal space peak of the original correlation kernel as a corresponding effective "$\mathbf{k} = 0$" mode. It is worth noting that, like the microscopic XPFC model, the full correlation kernel, in this amplitude formalism, is the *numerical envelope* of all reciprocal space peaks included to represent the crystal structural of interest. The form of the average density contribution is clarified in Section 7.3.

For a system exhibiting density variations, multiple crystal structures, multiple orientations and elasto-plastic effects operating on diffusive time and length scales, the total coarse-grained free energy, with the complex conjugate part of the excess term written explicitly for clarity, is,

$$F^{cg} = \int d\mathbf{r} \left\{ \frac{n_o^2}{2} - \eta \frac{n_o^3}{6} + \chi \frac{n_o^4}{12} + \left(1 - \eta\, n_o + \chi\, n_o^2\right) \left(\sum_j^4 |A_j|^2 + \sum_m^2 |B_m|^2 \right) \right.$$

$$- (\eta - 2\chi n_o) \left[A_1 A_2 A_3 + A_1^* A_4^* B_1 + A_1 A_4^* B_2^* + c.c. \right] + \frac{\chi}{2} \left[\sum_j^4 A_j^2 (A_j^*)^2 + \sum_m^2 B_m^2 (B_m^*)^2 \right]$$

$$+ 2\chi \left[\left(\sum_j^4 \sum_{m>j}^4 |A_j|^2 |A_m|^2 + \sum_j^4 \sum_m^2 |A_j|^2 |B_m|^2 + |B_1|^2 |B_2|^2 \right) \right]$$

$$+ \chi \left[2 A_2^* A_3^* A_4^* B_2^* + 2 A_2^* A_3^* A_4 B_1^* + A_1^2 B_1^* B_2^* + A_4^2 B_1^* B_2 + c.c. \right]$$

$$- \frac{n_o}{2} \left[\hat{\xi}_V(\mathbf{k}) \hat{C}_2(|\mathbf{k}|) \hat{n}_o(\mathbf{k}) \right]_{\mathbf{r}} - \frac{1}{2} \sum_j^4 A_j^* \left[\hat{C}_2(|\mathbf{k} + \mathbf{k}_j|) \hat{A}_j(\mathbf{k}) \right]_{\mathbf{r}} - \frac{1}{2} \sum_j^4 A_j \left[\hat{C}_2(|\mathbf{k} - \mathbf{k}_j|) \hat{A}_j(-\mathbf{k}) \right]_{\mathbf{r}}$$

$$\left. - \frac{1}{2} \sum_m^2 B_m^* \left[\hat{C}_2(|\mathbf{k} + \mathbf{q}_m|) \hat{B}_m(\mathbf{k}) \right]_{\mathbf{r}} - \frac{1}{2} \sum_m^2 B_m \left[\hat{C}_2(|\mathbf{k} - \mathbf{q}_m|) \hat{B}_m(-\mathbf{k}) \right]_{\mathbf{r}} \right\}. \tag{7.16}$$

7.2.5 Recovering Covariant Operators and amplitude representations of Other PFC Models

Our Fourier method from the above section can also be used to recover the gradient covariant operators found in amplitude expansions of other PFC models. Here we consider an expansion of the correlation around $\mathbf{k} = 0$, in powers of $\mathbf{k}^2$, like the standard PFC model of Elder and co-

workers [16, 17], however generalized to all orders. This can be compactly written as,

$$\hat{C}_2(|\mathbf{k}|) = \sum_{l=0}^{\infty} \frac{1}{l!}(\mathbf{k}^2)^l \frac{\partial^l \hat{C}_2}{\partial (\mathbf{k}^2)^l}\bigg|_{\mathbf{k}=0}, \tag{7.17}$$

where l enumerates the order of the terms in the expansion. We note that this expansion can be generally valid provided the correlation is some well-behaved function and expressible to reasonable accuracy in even powers of $\mathbf{k}$. This is true for most correlations derived from experiments or first principles or that can be fit to such techniques, like that of the eighth order fitting of Jaatinen and Ala-Nissila [59], which was found to be an accurate and efficient approximation to CDFT. Applying the same arguments for the average density and other couplings in the density expansion, as done above, Eq. (7.9) now becomes

$$\mathcal{G} = \int d\mathbf{k} \sum_{l=0}^{\infty} \varepsilon_l (\mathbf{k}^2)^l \hat{n}_o(\mathbf{k}) e^{\mathbf{i}\mathbf{k}\cdot\mathbf{r}} + \int d\mathbf{k} \sum_{l=0}^{\infty} \varepsilon_l (\mathbf{k}^2)^l \sum_{j}^{4} \hat{A}_j (\mathbf{k} - \mathbf{k}_j) e^{\mathbf{i}\mathbf{k}\cdot\mathbf{r}} \tag{7.18}$$

$$+ \int d\mathbf{k} \sum_{l=0}^{\infty} \varepsilon_l (\mathbf{k}^2)^l \sum_{m}^{2} \hat{B}_m (\mathbf{k} - \mathbf{q}_m) e^{\mathbf{i}\mathbf{k}\cdot\mathbf{r}} + c.c.,$$

where the Fourier transforms follow from Eq. (7.11), and where we have made the following definition,

$$\varepsilon_l = \frac{1}{l!} \frac{\partial^l \hat{C}_2}{\partial (\mathbf{k}^2)^l}\bigg|_{\mathbf{k}=0}. \tag{7.19}$$

Taking the inverse Fourier transform of Eq. (7.18) leads to

$$\mathcal{G} = \sum_{l=0}^{\infty} \varepsilon_l (-\nabla^2)^l \, n_o(\mathbf{r}) + \sum_{l=0}^{\infty} \varepsilon_l (-\nabla^2)^l \sum_{j}^{4} A_j(\mathbf{r}) e^{\mathbf{i}\mathbf{k}_j \cdot \mathbf{r}}$$

$$+ \sum_{l=0}^{\infty} \varepsilon_l (-\nabla^2)^l \sum_{m}^{2} B_m(\mathbf{r}) e^{\mathbf{i}\mathbf{q}_m \cdot \mathbf{r}} + c.c. \tag{7.20}$$

Noting that, $\nabla^2 \to \nabla^2 + 2\mathbf{i}\mathbf{k}_j \cdot \nabla - \mathbf{k}_j^2$ (the covariant gradient operator), when Laplacian operators act on terms of the form $A_j(\mathbf{r}) e^{\mathbf{i}\mathbf{k}_j \cdot \mathbf{r}}$, we have

$$\mathcal{G} = \sum_{l=0}^{\infty} \varepsilon_l (-\nabla^2)^l \, n_o(\mathbf{r}) + \sum_{j}^{4} e^{\mathbf{i}\mathbf{k}_j \cdot \mathbf{r}} \sum_{l=0}^{\infty} \varepsilon_l \bigg\{ - \big(\nabla^2 + 2\mathbf{i}\mathbf{k}_j \cdot \nabla - \mathbf{k}_j^2 \big) \bigg\}^l A_j(\mathbf{r}) \tag{7.21}$$

$$+ \sum_{m}^{2} e^{\mathbf{i}\mathbf{q}_m \cdot \mathbf{r}} \sum_{l=0}^{\infty} \varepsilon_l \bigg\{ - \big(\nabla^2 + 2\mathbf{i}\mathbf{q}_m \cdot \nabla - \mathbf{q}_m^2 \big) \bigg\}^l B_m(\mathbf{r}) + c.c.$$

Equations (7.20) and (7.21) show that an infinite set of covariant gradient operators (in the long wavelength limit) is needed to accurately capture the salient features, in real space, of a correlation kernel constructed in Fourier space, reflecting that the latter would require an infinite series of square gradient terms to be represented in a traditional PFC form. If we neglect all second mode contributions and truncate the series at $l = 2$ in Eq. (7.21), we recover the amplitude expansion of the standard PFC model [89], after the usual application of the coarse-graining operation. To make contact with the generalized formalism of the previous section, the amplitude terms are rewritten in terms of an inverse Fourier transform via a change of variable, and in Fourier space the resulting

correlation kernel expansion is re-summed, resulting in

$$
\mathcal{G} = \left[\hat{C}_2(|\mathbf{k}|)\hat{n}_o(\mathbf{k}) \right]_{\mathbf{r}} + \sum_{j}^{4} e^{\mathbf{i}\mathbf{k}_j \cdot \mathbf{r}} \left[\hat{C}_2(|\mathbf{k} + \mathbf{k}_j|)\hat{A}_j(\mathbf{k}) \right]_{\mathbf{r}}
$$

$$
+ \sum_{m}^{2} e^{\mathbf{i}\mathbf{q}_m \cdot \mathbf{r}} \left[\hat{C}_2(|\mathbf{k} + \mathbf{q}_m|)\hat{B}_m(\mathbf{k}) \right]_{\mathbf{r}} + c.c. \tag{7.22}
$$

Equation (7.22) represents the total convolution term of the excess free energy when the correlation function is expanded in even powers of $\mathbf{k}$, which gives the exact same result as Eq. (7.13). Completing the coarse-graining, after the application of the convolution operator in Eq. (7.3), it is easily seen that we recover the same coarse-grained excess free energy of Eq. (7.15).

7.3 Periodic Instability of the Average density

When one considers a density jump in performing amplitude expansions, using the standard PFC model of Elder and co-workers, it has been shown, with the standard coarse-graining approaches [107, 67], one recovers the original PFC model in the average density variable, n_o. This means that the same instability that causes the periodic solutions to be the equilibrium solutions, at sufficiently low temperature, can also cause the average density to become unstable. Often a second long wavelength approximation is made to suppress the associated terms responsible for the instability [110]. There exists two possible explanations as to the origin of this instability; (i) our assumption of the long wavelength nature of the average density, n_o, is incorrect or (ii) the coarse graining procedure, of any method, is not being applied correctly. As written, our current XPFC amplitude model is immune to this instability. We qualify this statement by showing the explicit steps required to coarse-grain the average density term in Eq. (7.13).

We start our discussion with the form of the correlation contribution of the average density term prior to introducing the volume-averaging kernel of Eq. (7.4). From Eq. (7.13), we have

$$
\mathcal{H} = -\frac{1}{2} \int d\mathbf{r}' \, n_o(\mathbf{r}') \left[\hat{C}_2(|\mathbf{k}|)\hat{n}_o(\mathbf{k}) \right]_{\mathbf{r}'}. \tag{7.23}
$$

After inserting the volume-averaging kernel, in Fourier space, we have

$$
\mathcal{H} = -\frac{1}{2} \int d\mathbf{r}' \int d\mathbf{r} \left[\int d\mathbf{q} \, \hat{\xi}_V(\mathbf{q}) \, e^{\mathbf{i}\mathbf{q}\cdot\mathbf{r}} e^{-\mathbf{i}\mathbf{q}\cdot\mathbf{r}'} \right] n_o(\mathbf{r}') \int d\mathbf{k} \, \hat{C}_2(|\mathbf{k}|) \, \hat{n}_o(\mathbf{k}) e^{\mathbf{i}\mathbf{k}\cdot\mathbf{r}'}. \tag{7.24}
$$

Here, $\hat{\xi}_V$, is the averaging (or convolution) kernel in Fourier space, which restricts the wavenumber $\mathbf{q}$ to small values, i.e., $\mathbf{q} < 1/L$, approximately the same as the first Brillioun zone or similarly the first peak (lattice spacing) of the correlation function. Note that the average density variable, $n_o(\mathbf{r}')$, is slowing varying, while the convolution term, $\hat{C}_2(|\mathbf{k}|)\hat{n}_o(\mathbf{k})$, can develop rapid oscillations due to the periodic instability caused by the correlation kernel. On scales of the rapidly oscillating term, it is reasonable to take an expansion of $n_o(\mathbf{r}')$ around $\mathbf{r}' = \mathbf{r}$, which allows us to remove it from the integral over $\mathbf{r}'$. Next, the noninvertible procedure, described above, occurs by switching the order of integration $d\mathbf{r}$ with $d\mathbf{r}'$, after which we integrate the equation with respect to $\mathbf{r}'$ yielding,

$$
\mathcal{H} = -\frac{1}{2} \int d\mathbf{r} \, n_o(\mathbf{r}) \int d\mathbf{q} \, \hat{\xi}_V(\mathbf{q}) \, e^{\mathbf{i}\mathbf{q}\cdot\mathbf{r}} \int d\mathbf{k} \, \hat{C}_2(|\mathbf{k}|) \, \hat{n}_o(\mathbf{k}) \, \delta(\mathbf{q} - \mathbf{k}). \tag{7.25}
$$

Integrating over $d\mathbf{k}$, we have

$$
\begin{aligned}
\mathcal{H} &= -\frac{1}{2} \int d\mathbf{r}\, n_o(\mathbf{r}) \int d\mathbf{q}\, \hat{\xi}_V(\mathbf{q}) \hat{C}_2(|\mathbf{q}|) \hat{n}_o(\mathbf{q}) e^{i\mathbf{q}\cdot\mathbf{r}} \\
&= -\frac{1}{2} \int d\mathbf{r}\, n_o(\mathbf{r}) \left[\hat{\xi}_V(\mathbf{k}) \hat{C}_2(|\mathbf{k}|) \hat{n}_o(\mathbf{k}) \right]_{\mathbf{r}},
\end{aligned}
\tag{7.26}
$$

where $[\,]_{\mathbf{r}}$ denotes the inverse Fourier transform and in the second line we have changed the wavenumber variable for convenience. Equation (7.26), clearly demonstrates that all the small wavelength modes associated with the periodic instability of the original correlation are suppressed by convolving with the volume-averaging kernel. In other words, considering the volume-averaging kernel as a filter, in this case a low-pass filter, it smooths/eliminates all the high-mode, i.e., small wavelength, peaks resulting from the correlation function. This effectively allows the system to only sample the long wavelength, i.e., small mode, information of the correlation function around $\mathbf{k} = 0$.

Equivalently, this can also be motivated from the multiple scale method of coarse-graining. In that method, a small parameter, ϵ [107, 67], is introduced in a perturbation type expansion which results in the wavenumber being described by $\mathbf{k} \rightarrow \mathbf{k} + \epsilon\mathbf{K}$, where $\mathbf{K}$ represents the large wavelength modes. Considering the long wavelength behavior of the average density, this results in the correlation function being evaluated at $\epsilon\mathbf{K}$, i.e., $\hat{C}_2(|\epsilon\mathbf{K}|)$, effectively shifting the modes sampled by the correlation to only those around $\mathbf{k} = 0$. It is worth noting that if one simply applies the so-called "quick and dirty" approach, of any of the coarse-graining methods when considering a density jump, the average density term will not be properly coarse-grained, resulting in a term which still possesses the instability of the original free energy.

7.4 Dynamics

Dynamics of the complex order-parameters comprising the coarse-grained free energy follow the usual principle of traditional phase-field models. Particularly, the average density, n_o, obeys conserved dissipative dynamics, while the amplitudes $\{A_j\}$ and $\{B_m\}$ follow nonconserved dissipative dynamics[†]. Specifically we have

$$
\frac{\partial n_o}{\partial t} = \nabla \cdot \left(M_{n_o} \nabla \left\{ n_o - \eta \frac{n_o^2}{2} + \chi \frac{n_o^3}{3} - \left[\hat{\xi}_V(\mathbf{k}) \hat{C}_2(\mathbf{k}) \hat{n}_o(\mathbf{k}) \right]_{\mathbf{r}} + (2\chi n_o - \eta) \left(\sum_j^4 |A_j|^2 + \sum_m^2 |B_m|^2 \right) \right. \right.
$$
$$
\left. \left. + 2\chi \left[A_1 A_2 A_3 + A_1^* A_4^* B_1 + A_1 A_4^* B_2^* + c.c. \right] \right\} \right).
\tag{7.27}
$$

Equations for the first mode of the amplitudes read,

$$
\frac{\partial A_1}{\partial t} = -M_{A_1} \left\{ \left(1 - \eta n_o + \chi n_o^2 \right) A_1 - (\eta - 2\chi n_o) \left[A_2^* A_3^* + A_4 B_2 + A_4^* B_1 \right] + 2\chi 2 A_1^* B_1 B_2 \right.
$$
$$
\left. + \chi A_1 \left(|A_1| + 2 \left[\sum_{j \neq 1}^4 |A_j| + \sum_m^2 |B_m| \right] \right) - \left[\hat{C}_2(|\mathbf{k} + \mathbf{k}_1|) \hat{A}_1(\mathbf{k}) \right]_{\mathbf{r}} \right\},
\tag{7.28}
$$

[†]While in this derivation the dynamics of n_o follow conserved and diffusive dynamics, in a more complete treatment, the dynamics of n_o can also be treated as a slow spatial but rapidly changing variable through the application of inertial dynamics [120] to the n_o equation.

$$\frac{\partial A_2}{\partial t} = -M_{A_2}\Bigg\{ \left(1 - \eta\, n_o + \chi\, n_o^2\right) A_2 - (\eta - 2\chi n_o) A_1^* A_3^* + 2\chi A_3^* \left[A_4 B_1^* + A_4^* B_2^*\right]$$
$$+ \chi A_2 \left(|A_2| + 2\left[\sum_{j\neq 2}^{4} |A_j| + \sum_{m}^{2} |B_m|\right]\right) - \left[\hat{C}_2(|\mathbf{k} + \mathbf{k}_2|)\hat{A}_2(\mathbf{k})\right]_{\mathbf{r}} \Bigg\}, \qquad (7.29)$$

$$\frac{\partial A_3}{\partial t} = -M_{A_3}\Bigg\{ \left(1 - \eta\, n_o + \chi\, n_o^2\right) A_3 - (\eta - 2\chi n_o) A_1^* A_2^* + 2\chi A_2^* \left[A_4 B_1^* + A_4^* B_2^*\right]$$
$$+ \chi A_3 \left(|A_3| + 2\left[\sum_{j\neq 3}^{4} |A_j| + \sum_{m}^{2} |B_m|\right]\right) - \left[\hat{C}_2(|\mathbf{k} + \mathbf{k}_3|)\hat{A}_3(\mathbf{k})\right]_{\mathbf{r}} \Bigg\}, \qquad (7.30)$$

$$\frac{\partial A_4}{\partial t} = -M_{A_4}\Bigg\{ \left(1 - \eta\, n_o + \chi\, n_o^2\right) A_4 - (\eta - 2\chi n_o) \left[A_1^* B_1 + A_1 B_2^*\right]$$
$$+ \chi \left[2A_2 A_3 B_1 + 2A_4^* B_1 B_2^* + 2A_2^* A_3^* B_2^*\right]$$
$$+ \chi A_4 \left(|A_4| + 2\left[\sum_{j\neq 4}^{4} |A_j| + \sum_{m}^{2} |B_m|\right]\right) - \left[\hat{C}_2(|\mathbf{k} + \mathbf{k}_4|)\hat{A}_4(\mathbf{k})\right]_{\mathbf{r}} \Bigg\}. \qquad (7.31)$$

Finally, for the second set of amplitudes, corresponding to the second reciprocal space peak, we have

$$\frac{\partial B_1}{\partial t} = -M_{B_1}\Bigg\{ \left(1 - \eta\, n_o + \chi\, n_o^2\right) B_1 - (\eta - 2\chi n_o) A_1 A_4 + \chi \left[2A_4 A_2^* A_3^* + A_4^2 B_2 + A_1^2 B_2^*\right]$$
$$+ \chi B_1 \left(|B_1| + 2\left[\sum_{j}^{4} |A_j| + |B_2|\right]\right) - \left[\hat{C}_2(|\mathbf{k} + \mathbf{q}_1|)\hat{B}_1(\mathbf{k})\right]_{\mathbf{r}} \Bigg\}, \qquad (7.32)$$

$$\frac{\partial B_2}{\partial t} = -M_{B_2}\Bigg\{ \left(1 - \eta\, n_o + \chi\, n_o^2\right) B_2 - (\eta - 2\chi n_o) A_1 A_4^* + \chi \left[2A_2^* A_3^* A_4^* + (A_4^*)^2 B_1 + A_1^2 B_1^*\right]$$
$$+ \chi B_2 \left(|B_2| + 2\left[\sum_{j}^{4} |A_j| + |B_1|\right]\right) - \left[\hat{C}_2(|\mathbf{k} + \mathbf{q}_2|)\hat{B}_2(\mathbf{k})\right]_{\mathbf{r}} \Bigg\}. \qquad (7.33)$$

The coefficients M_{n_o}, M_{A_j} and M_{B_m} denote the mobility parameters of the average density and each corresponding amplitude, respectively, and strictly speaking can be functions of the various fields in the free energy functional. We have appended to these equations of motion, the stochastic variables ζ_{n_o}, ζ_{A_j} and ζ_{B_m}, which model coarse-grained thermal fluctuations acting on the average density and amplitudes, respectively. Formally, they satisfy the fluctuation-dissipation relation, i.e., $\langle \zeta_\nu(\mathbf{r}, t)\rangle = 0$ and $\langle \zeta_\nu(\mathbf{r}, t)\zeta_\nu(\mathbf{r}', t')\rangle = \Gamma_\nu \delta(\mathbf{r} - \mathbf{r}')\delta(t - t')$, where ν denotes the average density or one of the amplitude fields, with $\Gamma_\nu \propto M_\nu k_B T$. Huang *et al.* [67] have formally shown how these coarse-grained stochastic variables are derived, in an amplitude equation formalism from dynamic density functional theory through multiple scale analysis. Next we showcase the dynamic properties of the derived amplitude model by performing numerical simulations.
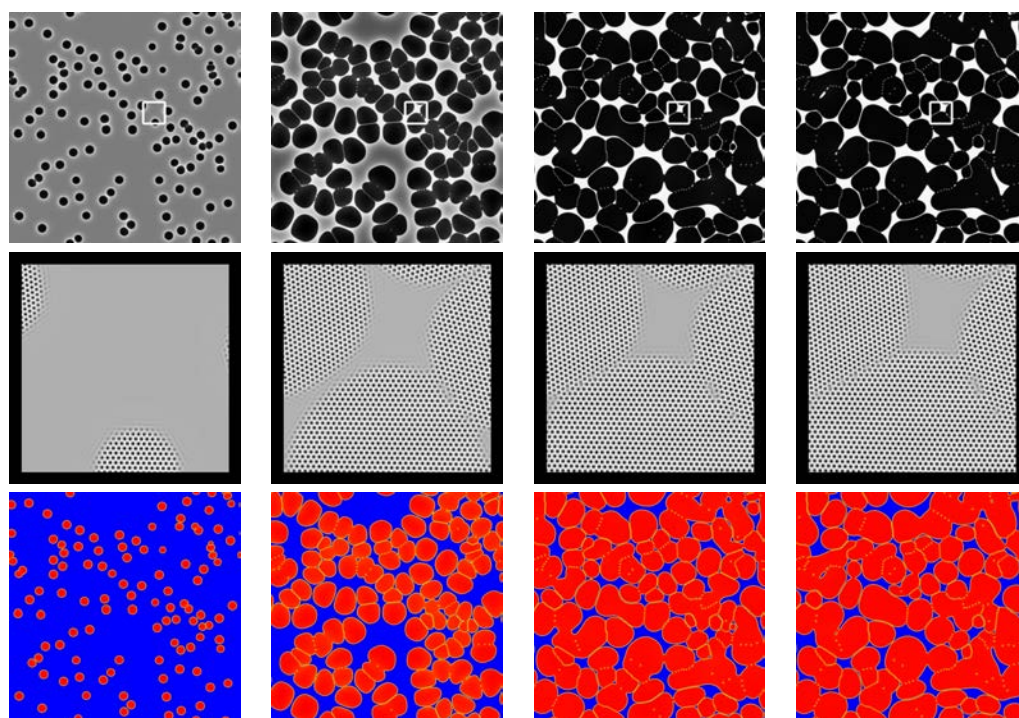
Figure 7.3: Solidification and coarsening images from a simulation run. The evolution of the system progresses in time from left to right, i.e., $t = 1,000, t = 5,000, t = 30,000$ and $t = 100,000$. Top row corresponds to the average density of the grains. Large density values are black, and lower values in white. Second row represents the reconstructed atomic density of those areas marked in the top row. Probable atomic regions are darker than less probable regions and uniform values represent liquid. Third row plots the magnitude of amplitude, A_1, where red regions denote large magnitudes and blue low magnitudes.

7.5 Amplitude Model Applications

It is well known that most engineering materials contain multiple phases and components. While the latter is not explored in this derivation, we can explore a system possessing multiple phases with the currently derived amplitude formalism. In this section, we demonstrate the complex amplitude model, capable of describing two different crystal symmetries by exploring solidification, coarsening and peritectic growth. We then look at the emergence of a second phase, during grain growth, from the boundaries of a single phase polycrystalline system.

In the sections to follow, simulations were performed using Eqs. (7.27)-(7.33). A semi-implicit Fourier technique was used to solve the system of equations. Unless stated otherwise, numerical grid spacing of $\Delta x = 0.5$ and time step of $\Delta t = 1$ have been used[‡]. Furthermore, for all stochastic variables, amplitudes have been set to zero, unless indicated otherwise. Following the original XPFC derivation of Greenwood *et al.*, here we take $\hat{C}_2(|\mathbf{k} = 0|) = 0$. For simplicity, we also take all mobility coefficients to be equal to unity, i.e., $M_\nu = 1$, were ν is one of the corresponding fields (n_o, $\{A_j\}$, or $\{B_m\}$) in the free energy functional of Eq. (7.16). Finally, all simulations were conducted in the phase space mapped out by the equilibrium phase diagram in Fig. 2.4(a) of Section 2.2.5. The reader is referred to the figure caption for other parameter details.

7.5.1 Single Phase Solidification and Coarsening

As a first illustration of our amplitude model, we simulate the solidification of a polycrystalline network of grains having triangular symmetry. Our simulation domain was set to 4096×4096 grid spacings, which is equivalent to approximately 512×512 lattice spacings. Initially, the system was seeded with ~ 100 triangular crystallites randomly distributed in a uniform liquid. Each crystallite had a radius of 30 grid spacings (~ 4 lattice spacings) and a randomly chosen orientation. The average density was chosen to be $n_o = 0.115$, which at a temperature of $\sigma = 0.16$ in equilibrium would give a final solid fraction of approximately 0.87 according to the lever rule. The amplitudes of the initial triangular nuclei were chosen to satisfy $A_j^\theta = A_j e^{i\delta\mathbf{k}_j(\theta)\cdot\mathbf{r}}$ ($j = 1, 2, 3$), where A_j is the corresponding amplitudes of the original reference basis, $\delta\mathbf{k}_j(\theta) = \mathbf{K}_j(\theta) - \mathbf{k}_j$, with θ being the randomly chosen orientation between the interval $[-\pi/6, \pi/6]$ and $\mathbf{K}_j(\theta)$ the rotated triangular reciprocal lattice vectors.

In Fig. 7.3, we show some snapshots of the solidification and coarsening process. In descending order of rows from top to bottom, Fig. 7.3 displays the average density field, the reconstructed atomic density (from a portion of the simulation domain) and the magnitude of A_1, respectively, with simulation times $t = 1,000, t = 5,000, t = 30,000$ and $t = 100,000$, increasing from left to right. As shown in the images of the average density, i.e., top row, where darker areas denote regions of high density and white regions of low, initial crystallites once nucleated, grow and partly coalesce leading to grain boundaries ($t = 5,000$), defined by the dislocations between boundaries. After the soft impingement of the grains, once the system has approximately reached the equilibrium solid fraction, we observe subsequent coarsening in frames $t = 30,000$ and $t = 100,000$, which occurs to minimize the total interfacial energy of the system via curvature reduction. This manifests itself in the standard process of coarsening with larger grains growing at the expense of smaller ones.

7.5.2 Peritectic Growth

Our second demonstration of the above amplitude model exploits the multi-phase nature of the XPFC modeling formalism. Here we illustrate peritectic growth, where the two solid structures have different crystalline symmetries. The simulation cell was a rectangular domain of size 768×1024 grid spacings ($\sim 96 \times 128$ lattice spacings), where we initialized the system with alternating square

---

[‡]The numerical grid spacing of 0.5 for this amplitude model is ~ 4 times larger than the full microscopic XPFC model (0.125). While the time step of 1 is ~ 100 times larger.

and triangular structures having length 200, and width 100 grid spacings respectively. The average density was set to $n_o = 0.07$, at the approximate peritectic temperature, $\sigma = 0.1256$. Figure 7.4 shows a snapshot during the growth process at late time. Displayed are a selection of the various fields which make up the peritectic structure. We have in Fig. 7.4, the average density field (top left), the reconstructed atomic density of the area marked on the average density (top right), the magnitude of A_1 (non-zero for both structures, bottom left), and the magnitude of B_1 (non-zero for the square phase, bottom right).
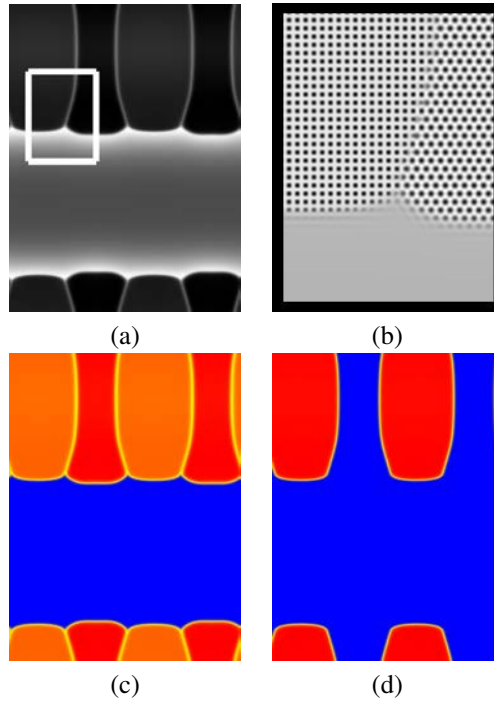
Figure 7.4: Simulation snapshots, at $t = 10,000$, of peritectic solidification. (a) average density, where dark regions represent high density areas, with lighter regions low density. (b) Reconstructed atomic probability density of the marked area in (a). Areas of largest probability are darker compared to areas of lower probability. (c) Magnitude of amplitude A_1, which is nonzero in both solid structures; areas of larger magnitudes are depicted in red and zero magnitudes are blue. (d) Magnitude of amplitude B_1, which is only nonzero in the square phase. Color scheme is the same as in (c).

7.5.3 Grain Growth and Emergence of Second Phase Structures

To further illustrate the robust capability of the amplitude model derived in this work, here we examine the emergence of a secondary phase (square), from the grain boundaries and triple junctions of a polycrystalline network of grains having triangular symmetry. The initial condition was taken from the solidification simulation of our triangular system, in Sec. 7.5.1, at $t = 5,000$. This system was quenched into the single square-phase region at a temperature of $\sigma = 0.1$. The system was left for a thousand time steps to allow complete coalescence and merger of the grains having triangular symmetry. After merger, a nonzero noise amplitude of 0.001 for all stochastic variables was introduced for all dynamic equations, thus activating thermal fluctuations in the system for one thousand time steps. Once nucleation of the square phase was apparent, the noise amplitude was set back to zero.
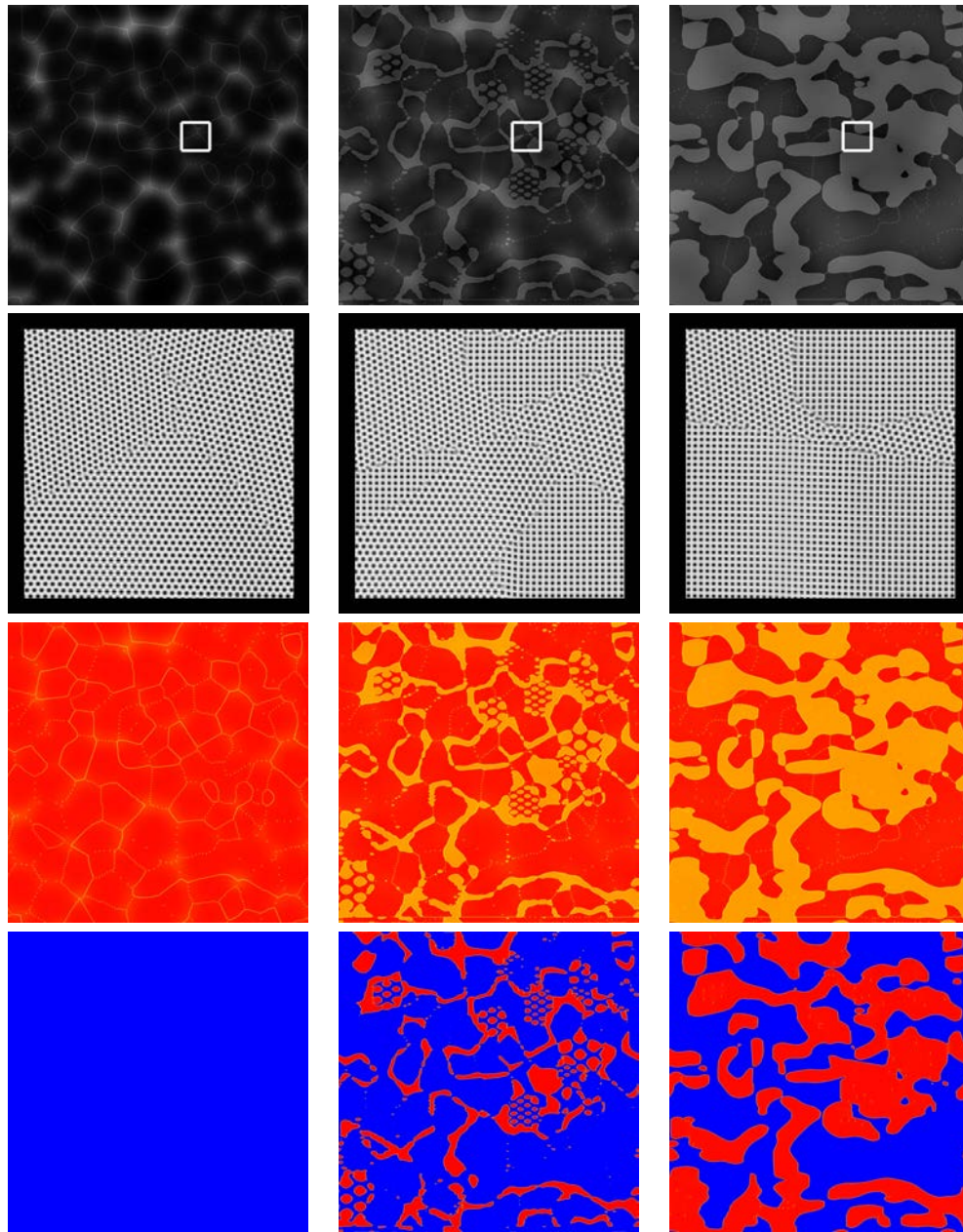
Figure 7.5: Time evolution of grain growth exhibiting emergence of a secondary phase (square) at the boundaries and triple junctions of the primary solidified phase (triangular). System evolution progresses from left to right, i.e., $t = 1,000$, $t = 2,000$ and $t = 9,000$. Top row plots the average density. Large density values are darker shades while low values are light shades. The reconstructed atomic density of the areas marked in the top row are shown in the second row. Third and fourth rows display $|A_1|$ and $|B_1|$, respectively. Red indicates areas of large magnitudes while blue represents a magnitude of zero.

Figure 7.5 shows several snapshots during the system evolution, exhibiting the emergence of the secondary square phase from the boundaries of the triangular polycrystalline network. From top to bottom, the plots display the average density, n_o, the reconstructed density, n, the magnitude of amplitude A_1 and the magnitude of B_1 (which is only nonzero for the square phase). Time increases from left to right in Fig. 7.5. Clearly evident in the progression of the images in Fig. 7.5 is onset and subsequent growth of the secondary phase. This illustrates the further capability of our amplitude model in describing the self-consistent nucleation and growth of phases, a phenomena that cannot be captured currently with phase-field and other mean field type formalisms.

7.6   Summary and Conclusions

In this chapter, we reported on a new Fourier technique for deriving complex amplitude models for PFC and PFC-type free energy functionals. The details of the method were discussed, in context of the structural PFC formalism for pure materials in 2D, wherein it was shown to recover forms of previous approaches, as well as address the periodic instability of the average density. The dynamics of the model were demonstrated on solidification and coarsening, peritectic solidification involving different crystal structures, and grain growth exhibiting nucleation and growth of secondary phases, phenomena of relevance in microstructural evolution, where the latter two cannot be captured with currently available mean-field formalisms such as the phase-field method.

Complex amplitude models were introduced as a way to provide a link between the standard phase-field approach and the phase-field-crystal approach. As the first complex amplitude model, capable of describing multiple crystal structures and elasto-plastic effects, this work has demonstrated the nature of such a bridge between the methodologies by directly incorporating the more fundamental and microscopic correlation function. Operating on larger scales, the model was shown to capture the salient atomistic scale features, currently outside the capability of the standard phase-field approach. As a novel technique, our method can accept as input any derived or experimentally calculated correlation function, which makes it applicable to a myriad of systems. To further demonstrate the validity and feasibility of our method, we also report derivation of a complex amplitude model for a symmetric triangle-triangle binary alloy in Appendix C.4. It is expected such a method, when combined with novel mesh algorithms, can truly represent a multi-scale modelling paradigm for investigating microstructural processes governed by elasticity and defects operating on diffusional time and length scales.

Chapter 8

Conclusions and Future Outlook

8.1 Conclusions

Starting with the standard PFC model, we developed a model for studying the stability of nanocrystalline systems under forced ballistic conditions in Chapter 3. Particularly, where nanocrystalline materials are being considered as practical replacements for traditional polycrystalline systems, our results suggest that the benefits afforded by nanocrystalline materials are not long lasting as they are prone to enhanced grain growth. The model however is not limited to external driving only of a ballistic nature but can also be augmented to study such external driving caused by electromagnetic effects. Our primary work with the PFC approach did well in demonstrating the robustness and capability of the method, but also to highlight where improvements have been made and where improvements can be made further still.

A major improvement recently made to the standard PFC approach was that by Greenwood *et. al* [19, 20], who for the first time allowed the description of multiple crystal structures in coexistence with themselves and the liquid phase. Improving still on their work, in this dissertation, we successfully extended the so-called XPFC method to multi-component systems, Chapter 4, to address the complex interactions and nature inherent in experimentally relevant alloy systems. The first of its kind in the variants of PFC approaches, our N-component XPFC method couples multiple concentrations species with a single density capable of describing multiple crystalline phases through an effective correlation kernel modulated via concentration interpolation functions. The capability and validity of the model was demonstrated by reducing the model to binary and ternary alloy systems, in Chapter 5 and Chapter 6, respectively. We investigated the equilibrium properties of both alloy systems by examining phase diagrams of generic alloy systems, and several motivated from industrially relevant systems, i.e., high temperature Fe-Ni, Cu-Ni, Section 5.5 and simplified ternary Al-Cu-Mg, Section 6.5. Dynamic demonstrations of the models were conducted to test the kinetic behaviour of the models as well. The models were shown to be well suited in describing eutectic solidification in binary and ternary alloys, in Sections 5.6 and 6.6, respectively; dendritic solidification in ternary alloys, in Section 6.6, as well as solute segregation to defects, in Section 5.6. These are phenomena that represent paradigms of microstructure evolution and require atomistic scale description of phases, and surface and elastic energy and their anisotropy.

We also applied the models to the study of early stage clustering leading to precipitate nucleation, in Sections 5.7 and 6.7, the initial stages of a heat treatment process known as quenching/ageing. This particular heat treatment is conducted to induce phase transformations causing precipitation to help strengthen alloys, a process also referred to as precipitation hardening. There has long being a conjecture in the clustering literature as to the exact fundamental mechanism leading to early stage clustering. The ability of the XPFC binary and ternary alloy models to describe a wealth of complexity of interactions, such as solute-solute, defect-solute, and defect-defect, allowed for the

first time, an atomistic model description of clustering. Through careful simulations and quantitative analysis of system thermodynamics, our data suggests a dislocation-mediated mechanism for early stage clustering in Al binary and ternary alloys. Specifically in the case of ternary alloys, we find that the addition of trace amounts of Mg to binary Al-1.1Cu, not only promotes clustering but also results in a refinement of the final microstructure as well, in good agreement with current experimental results.

The dissertation ended by switching focus to specialized PF models that employ complex order-parameters. These amplitude/complex order-parameter models are derived from PFC models and maintain many of the salient features from the more microscopic theory. In Chapter 7, a novel method for coarse-graining PFC and CDFT type models, applied specifically to the XPFC pure material in 2D, was presented. Our Fourier method was demonstrated to be unique yet general in recovering the form of amplitude expansions, namely the covariant operator, of the standard PFC method as well as in applying it to the other variants of PFC methods, with an extension to 3D structures and alloys readily available. The model, through dynamic demonstrations, was shown to reproduce all the atomistic scale features, crystalline phases, elasto-plasticity, etc., all on larger scales than that of the original XPFC. The capability of the model, given the length scales (and time scales) on which it operates opens a myriad of possible application for studying experimentally relevant microstructural phenomena on appropriate scales.

8.2   Future Outlook

The work in this thesis is far from complete. For each aspect we reported on, there are a wide range of avenues from which one can proceed to improve the work, or further develop what has been included. The following are only select choices of issues we feel would be most beneficial in addressing microstructural evolution.

Nucleation of phases in the PFC formalism requires a proper description of thermal fluctuations. A process whose accurate and quantitative description is presently lacking in the PFC formalism. A method which can be used to quantify fluctuations already exists in literature from the work of Hoyt *et. al* [121, 122]. In their work, using capillary fluctuation theory applied to MD simulations, they were able to calculate the anisotropy of the stiffness, a parameter which is of importance as input into PF models for simulating dendrites, to very high numerical accuracy. Applied to the PFC formalism, we speculate, not only will such a method yield the energy scale of fluctuations in the PFC, but since such a scale is related to temperature and determines the mobility, through fluctuation dissipation, they can also be used to ascertain the temperature scale relation to PFC parameters as well as the time scale relation of PFC models. An investigation into this, using the standard PFC and XPFC pure material work Elder *et. al* [16, 17] and Greenwood *et. al* [19, 20], has already been initiated in this regard.

The amplitude expansion we presented was the first to consider multiple crystalline structures, as well as incorporating the unique Fourier space correlation kernel of Greenwood *et. al* [19, 20]. Amplitudes in general are currently plagued by two outstanding issues. The first consists of the formation of a boundary when two grains of the same orientation coalesce or merge due to phase variances. The second is the lack of barriers, such as a Peierls barrier, since all amplitude expansions only include the lowest order terms. The first of these has yet to be addressed, while for the latter of these, a recent publication by Huang [123], is under active investigation, however numerics are found to be problematic. Work on dislocation behaviour in BCC systems by Lakshmi *et. al* [114], hinted to the fact that a non-local approximation and a multi-peak description of the correlation kernel could circumvent the lack of energetic barriers. With the current amplitude model we have presented, the full correlation is included and thus is the hope that such features will naturally fall out. Initial results however are contrary to the statement of Lakshmi *et. al*. A more exhaustive and detailed investigation needs to be conducted as this outstanding issue is what precludes the amplitude

formalism from truly describing relevant materials phenomena, such as recrystallization where dislocation behaviour is important. Once these issues haven been resolved, such amplitude expansions capable of describing multiple phases, multiple components, elasto-plasticity, grain boundaries and defects across atomistic and mesoscopic length scales, would represent a true multi-scale platform for studying microstructure evolution.

Appendix A

Semi-Implicit Spectral Method

In this appendix, we describe the main numerical scheme used throughout this dissertation. Namely, we examine the *semi-implicit spectral method* that has been used extensively in numerical implementations of the PFC methodology. The equation of motion for any PFC model, for single components for simplicity, can generally be written in Fourier space as,

$$\frac{\partial \hat{n}(\mathbf{k})}{\partial t} = \mathcal{L}(\mathbf{k})\hat{n}(\mathbf{k}) + \mathcal{N}\left[\hat{n}(\mathbf{k})\right], \tag{A.1}$$

where $\mathcal{L}$ is an operator containing all the linear parts of the equation and $\mathcal{N}$ is an operator which contains the remaining, nonlinear, parts of the equation. The application of the method to a particular PFC model would only alter the form of the linear and nonlinear operators. For the standard PFC model, the operators take the form

$$\mathcal{L}(\mathbf{k}) = -M\mathbf{k}^2(\Delta B_0 + B^x\left(-2\mathbf{k}^2 + \mathbf{k}^4\right)) \tag{A.2}$$

and,

$$\mathcal{N}\left[\hat{n}(\mathbf{k})\right] = -M\mathbf{k}^2\left[\left([\hat{n}(\mathbf{k})]_\mathbf{r}\right)^3\right]_\mathbf{k} \tag{A.3}$$

where $[\,]_\mathbf{k}$ and $[\,]_\mathbf{r}$ are forward and inverse transforms, respectively. The operators for the standard XPFC model are defined as

$$\mathcal{L}(\mathbf{k}) = -M\mathbf{k}^2(1 - \hat{C}_2(\mathbf{k})) \tag{A.4}$$

and,

$$\mathcal{N}\left[\hat{n}(\mathbf{k})\right] = -M\mathbf{k}^2\left\{\left[-\frac{\eta}{2}\left([\hat{n}(\mathbf{k})]_\mathbf{r}\right)^2 + \frac{\chi}{3}\left([\hat{n}(\mathbf{k})]_\mathbf{r}\right)^3\right]_\mathbf{k}\right\} \tag{A.5}$$

Discretizing the equation of motion yields,

$$\frac{\hat{n}_\mathbf{k}^{t+\Delta t} - \hat{n}_\mathbf{k}^t}{\Delta t} = \mathcal{L}(\mathbf{k})\hat{n}_\mathbf{k}^{t+\Delta t} + \mathcal{N}\left[\hat{n}_\mathbf{k}^t\right], \tag{A.6}$$

where we have gone from the continuous description to discrete description of the Fourier transform. Δt is the numerical time step, while $\mathcal{L}$ and $\mathcal{N}$ are the discrete versions of the operators. Note that we have evaluated all linear terms implicitly at $t + \Delta t$, while the nonlinear terms have been explicitly evaluated at t, thus the name semi-implicit. Rearranging, the updating equation for the next time step is written as,

$$\hat{n}_\mathbf{k}^{t+\Delta t} = \frac{\hat{n}_\mathbf{k}^t + \Delta t \mathcal{N}\left[\hat{n}_\mathbf{k}^t\right]}{1 - \Delta t \mathcal{L}(\mathbf{k})}. \tag{A.7}$$

Appendix B

Phase Diagrams

To perform efficient numerical simulations, one requires knowledge of the equilibrium phase space which the system of interest occupies, i.e., phase diagrams. The PFC methodology, through standard minimization schemes is capable, within certain approximations, of calculating analytically/numerically the equilibrium phase space of interest for a chosen system. Here, in this appendix, we present the procedure of phase diagram calculation in the context of the PFC alloy models in this thesis.

B.1 Free Energy Integration and Amplitude Minimization - PFC

For the standard PFC model, in 2D, from Eq. (2.20) we recognize that the density approximation contains only a single amplitude. With the density approximation in hand, the binary alloy free energy of Elder and co-workers, Eq. (2.32), is integrated over a single unit cell. The free energy is of the form

$$\frac{\mathcal{F}_{pfc}^{\text{bin}}}{V} = \frac{1}{a^3} \int_{cell} dV \left\{ \frac{n}{2} \left[B^\ell + B^x \left(2\nabla^2 + \nabla^4 \right) \right] n - \frac{t}{3} n^3 + \frac{\nu}{4} n^4 + \frac{\omega}{2} \psi^2 + \frac{u}{4} \psi^4 + \frac{K}{2} |\nabla \psi|^2 \right\} \tag{B.1}$$

Note that when performing the integral over the unit cell (after substituting in the periodic density expansion), all concentration, i.e., ψ, contributions are assumed to be left unaffected as they are smooth on the scales of the periodicity of the density. Performing the integral over the unit cell of a triangular unit cell yields

$$\frac{\mathcal{F}_{pfc}^{\text{bin}}}{V} = -\frac{1}{2} \varphi^2 q^2 B^{x\,2} + \frac{1}{3} \varphi^2 q^4 B^x + \frac{3}{16} \varphi^2 B^\ell + \frac{45}{512} \varphi^4 \nu - \frac{1}{16} \varphi^3 t + \frac{w}{2} \psi^2 + \frac{u}{4} \psi^4 \tag{B.2}$$

where φ is the amplitude of the periodic oscillation. We now minimize for the amplitude, φ, and the wavenumber, q, the two unconserved quantities. We find that the minimized values correspond to

$$q_{\text{eq}} = \frac{\sqrt{3}}{2} \tag{B.3}$$

and

$$\varphi_{\text{eq}} = \frac{4}{45} \frac{3\,t + \sqrt{9\,t^2 + 360\,\nu\,B^x q^2 - 240\,\nu\,B^x q^4 - 135\,\nu\,B^\ell}}{\nu}. \tag{B.4}$$

Substituting these minimized values back into the integrated energy, along with the trivial solution for the liquid energy, yields the following free energies for the respective phases,

$$F_{liq} = \frac{w}{2}\psi^2 + \frac{u}{4}\psi^4 \tag{B.5}$$

$$F_{sol} = F_{liq} - \frac{B^x}{75\,\nu}\varphi_{\text{eq}}^2 + \frac{B^\ell}{75\,\nu}\varphi_{\text{eq}}^2 + \frac{1}{2250\,\nu^2}\varphi_{\text{eq}}^4 - \frac{4t}{3375\,\nu^2}\varphi_{\text{eq}}^3 \tag{B.6}$$

These energies for the different phases are used to construct the phase diagrams by solving the equations for the common tangent, i.e., Eq. (5.7).

B.2　Free Energy Integration and Amplitude Minimization - XPFC

The construction of the energy curves is performed by making certain approximations to the density field which allow the mathematics to be more tractable. From one of Eq. (5.9) or Eq. (6.8), it can be seen that the FCC density approximation is constructed via two amplitudes. The binary free energy in Eq. (5.1) is integrated over a single unit cell using the following density approximation for each phase: constant, triangle and square for 2D and constant, BCC and FCC for 3D phase diagrams. The free energy functional, for a binary alloy, is reproduced here:

$$\frac{\mathcal{F}_{xpfc}^{\text{bin}}}{V} = \frac{1}{a^3}\int_{cell} dV \left\{ \frac{n^2}{2} - \eta\frac{n^3}{6} + \chi\frac{n^4}{12} + \kappa|\nabla c|^2 + (n+1)\omega F_{\text{mix}}^{\text{bin}}(c) - \frac{1}{2}n\int C_{\text{eff}}(|\mathbf{r}-\mathbf{r}'|)n' \right\} \tag{B.7}$$

Under the multi-mode approximation, the composition field is assumed to be constant in the bulk lattice and correspondingly the gradient term in composition in this equation is zero. Likewise, the pre-multiplying component n to the $F_{\text{mix}}^{\text{bin}}$ term integrates to zero over the unit cell since the integration is completed around the reference density $n_o = 0$. These considerations leave the following integral to be calculated.

$$\frac{\mathcal{F}^{\text{bin}}}{V} = \frac{1}{a^3}\int_{cell} dV \left\{ \frac{n^2}{2} - \eta\frac{n^3}{6} + \chi\frac{n^4}{12} + \omega F_{\text{mix}}^{\text{bin}}(c) - \frac{1}{2}n\int C_{\text{eff}}^{\text{bin}}(|\mathbf{r}-\mathbf{r}'|)n' \right\}. \tag{B.8}$$

The $F_{\text{mix}}^{\text{bin}}(c)$ term is pulled from the integral entirely since it only depends on the smooth field c, and is thus trivial to compute. The ideal component to the energy is also easy to integrate in terms of the density mode approximation above, yielding a function in terms of the density amplitudes, φ_1 and φ_2 and the parameters η and χ. For example inputting a two-mode general expression for a square density field yields $F_{id}/V = 2(\varphi_1^2+\varphi_2^2) - 4\eta\varphi_2\varphi_1^2 + 12\chi\varphi_1^2\varphi_2^2 + 3\chi(\varphi_1^4+\varphi_2^4)$. The trivial minimum of this energy is $\varphi_1 = \varphi_2 = 0$, in the limit of the ideal energy expansion. The particular choice of η and χ can lead to different minimizations of ΔF_{id} with non-zero amplitudes [20], however we restrict η and χ in ranges that have a zero amplitude minimization for the ideal energy.

The unit cell spacing, a, non-trivially depends on composition as it is linked to the form for the resultant correlation function based on bulk composition, $C_{\text{eff}}^{\text{bin}}$. We consider two cases in this thesis. The first is the case where the lattice spacings for the elements are similar, in this case the correlation peaks closely align and we treat the resultant peak positions to correspond to lattice spacings interpolated by the compositional interpolation functions, ie. the lattice spacing for fcc in the peritectic phase diagram $a_{fcc} = X_1 a_{fcc}^A + X_2 a_{fcc}^B$. The second is the case where the peaks in the correlation function do not align at all, as is the case for the square-triangle phase diagram of Fig. 5.2. Here we assume the lattice spacing does not vary greatly from the dominant structure, which can be seen by the very small shift in the peak positions in $C_{\text{eff}}^{\text{bin}}$.

With this approximation, the convolution can be integrated mode by mode in the density ex-

pansion of Eq. (5.9). In Fourier space the convolution integral becomes trivial, with the periodic density expansion yielding a Dirac delta function so that the convolution returns the mode that was input, modulated by the correlation peak height at that mode frequency, i.e., $\int C_{\text{eff}}^{\text{bin}}(|\mathbf{r} - \mathbf{r}'|)n = \sum_m \int C_{\text{eff}}^{\text{bin}}(|\mathbf{r} - \mathbf{r}'|)n_m = \sum_m \hat{C}_{\text{eff}}^{\text{bin}}(k_j)n_m$, where m denotes the individual modes in the density approximation. Summing over all the reciprocal space modes for a given density expansion and integrating over the unit cell gives an excess energy

$$\frac{F_{ex}}{V} = -M_1\varphi_1^2 \hat{C}_{\text{eff}}^{\text{bin}}(k_1) - M_2\varphi_2^2 \hat{C}_{\text{eff}}^{\text{bin}}(k_2), \tag{B.9}$$

where for the different symmetries M_1 and M_2 take values of half of the number of modes used to construct the phase. A triangular phase, for instance, uses 6 modes in reciprocal space corresponding to k_1 and zero modes for k_2, so that $M_1 = 3$ and $M_2 = 0$. Correspondingly we use for square symmetry: $M_1 = 2$ and $M_2 = 2$, BCC: $M_1 = 6$ and $M_2 = 0$ and FCC: $M_1 = 4$ and $M_2 = 3$. The function $\hat{C}_{\text{eff}}^{\text{bin}}(k_j)$ is simply the value of the correlation kernel at the frequency of the mode in question. k_1 and k_2 are the resultant peak positions corresponding to the lattice position modified by the composition, i.e., $a_{fcc} = X_A a_{fcc}^A + X_B a_{fcc}^B$ for example.

The total free energy per unit cell is therefore a 4th order polynomial function in φ_1 and φ_2 and also a function of c and σ. Before constructing the phase diagram this polynomial must be minimized with respect to the amplitudes φ_1 and φ_2. To make this calculation tractable, we make a further assumption that the second amplitude of two mode density fields is a function of the first amplitude $\varphi_2 = f\varphi_1$*. For the purpose of calculating the phase diagram we assume that f varies very little over the range of σ values we are interested in. We compute f explicitly for the case of $\sigma = 0$. For the square phase $f = 0.605$ and for the fcc phase $f = 0.568$. The resulting single amplitude is then easily minimized as a function of both c and σ. For the square-square phase diagram in Fig. 5.1 for example, the minimized amplitude is

$$\varphi_1 = \frac{(\eta f + \frac{1}{3})}{2\chi(f^4 + 4f^2 + 1)}\left[9\eta^2 f^2 - 12\chi f^2 \left(5 + 5\chi f^2 + f^4\right) - 12\chi\left(1 - \hat{C}_{\text{eff}}^{\text{bin}}(k_2)\right)\right.$$
$$\left. + 12\chi f^2 \left(\hat{C}_{\text{eff}}^{\text{bin}}(k_1) + 4f^2\hat{C}_{\text{eff}}^{\text{bin}}(k_1) + f^4\hat{C}_{\text{eff}}^{\text{bin}}(k_1)\right) + 12\chi f^2 \left(4\hat{C}_{\text{eff}}^{\text{bin}}(k_2) + f^2\hat{C}_{\text{eff}}^{\text{bin}}(k_2)\right)\right]^{\frac{1}{2}}. \tag{B.10}$$

The minimized amplitude is then substituted back into the free energy giving an energy as a function of c and σ only. These energies for the different structures are used to construct the phase diagrams by solving Eq. (5.7).

Figure (B.1) shows a comparison between the phase diagram using our minimization technique that uses two amplitudes and another which uses a single value for all amplitudes in the density expansion, i.e., where $\varphi_2 = \varphi_1$ [89]. As mentioned previously, the qualitative features are not altered. However, the phase diagram undergoes a quantitative shift as a function of temperature.

B.3   A Note on Ternary Alloy Phase Diagram Calculation

Regardless of the number of components, the above mentioned procedure for amplitude minimization and free integration remains valid. For a ternary alloy, Eq. (6.9) provides a system of equations that are exact when one needs to determine the equilibrium properties of a given system. For a binary system, where the number of equations in Eq. (6.9) is reduced by one, at a specified temperature and pressure they are sufficient to specify exactly the unique phase concentrations corresponding to the tie line between two phases. However for multi-component systems, for the specific case of a ternary

---

*This can be shown via structure factor calculations in solid-state physics.
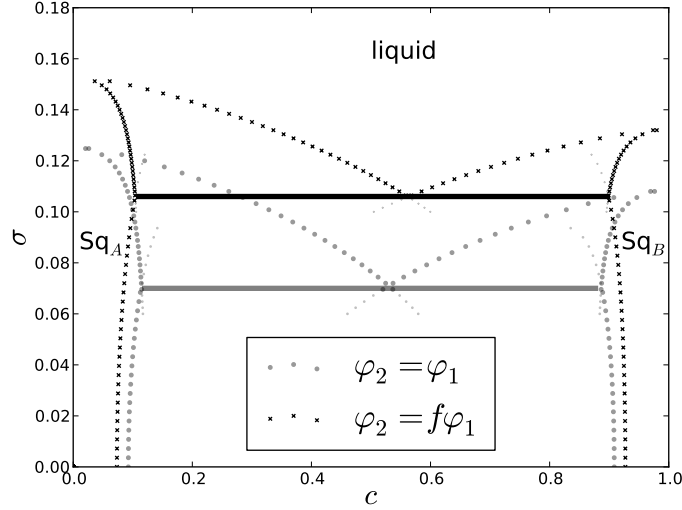
Figure B.1: Square-square phase diagrams showing both the two and single amplitude approximations. Parameters used for the calculation are given in the Section 5.5 of the text.

alloy studied in Chapter 6 (represented by solute compositions A and B), the set of conditions in Eq. (6.9) are under-determined and cannot uniquely define all phase concentrations. This is because, for a ternary system at a specified temperature and pressure, there is not generally a single tie line which specifies phase boundaries between coexisting phases but rather multiple tie lines defining the boundary between any two phases.

The under-determined set of conditions in Eq. (6.9) contain variables c_A^I, c_A^J, c_B^I and c_B^J in phases I and J respectively. To close this system, an additional condition is necessary to provide a fourth equation relating the concentrations. A convenient fourth condition is the *lever rule*, which relates weight fractions of phases to the average concentration. For clarity, we specify it here for ternary solid (α) and liquid (L) phases,

$$c_{o,A} = c_A^L x_L + c_A^\alpha x_\alpha \tag{B.11}$$

and

$$c_{o,B} = c_B^L x_L + c_B^\alpha x_\alpha, \tag{B.12}$$

where $c_{o,A}$ and $c_{o,B}$ are the average alloy compositions for components A and B respectively and x_L and x_α represent the equilibrium volume fractions of liquid and α respectively, and satisfy $x_L + x_\alpha \equiv 1$. Combining this last relation between the volume fractions and Eqs. (B.11) and (B.12) gives, the last equilibrium condition,

$$\frac{c_{o,A} - c_A^\alpha}{c_A^L - c_A^\alpha} = \frac{c_{o,B} - c_B^\alpha}{c_B^L - c_B^\alpha}. \tag{B.13}$$

Equation (6.9) together with Eq. (B.13) comprises a complete set of equations which can admit unique tie line solutions, i.e., solutions for c_A^L, c_A^α, c_B^L and c_B^α in the solid-liquid example just considered.

With the free energy functions generally being highly nonlinear, it is not possible to find analytical solutions to Eqs. (6.9) and (B.13), and they must be solved numerically. One approach is to specify the temperature and then raster through the phase space of average concentrations $c_{o,A}$ and $c_{o,B}$, where the rastering is done by taking discrete steps in steps of Δc_A and Δc_B, respectively (for practical purposes its convenient to set $\Delta c_A = \Delta c_B = \Delta c$). For each pair of $c_{o,A}$ and $c_{o,B}$,

Eqs. (6.9) and (B.13) can be solved numerically. The solutions yield c_A^L, c_A^α, c_B^L and c_B^α. A unique solution for each pair of $c_{o,A}$ and $c_{o,B}$ defines one tie line. The collection of all such tie lines maps out the coexistence phase boundaries between any two phases, in the case considered here, L and α. Where no solutions are admitted correspond to single phase regions where no tie lines exist. It is expected that the smoothness of the phase boundaries, when plotted for graphical purposes, will depend on the step size, Δc, chosen to discretize the average concentration values.

The above mentioned recipe can still require intensive computation, requiring a solution of four equations in four unknowns for M^2 combinations of average concentration pairs (where M is the discretized number of average concentration values for a given component). We adopted a simpler approach to compute the ternary phase diagrams in Section 6.5. In particular, given a temperature, σ, we fixed one of the equilibrium concentrations in Eq. (6.9), assuming it is a valid solution at that temperature. We then solved for the remaining three unknown concentrations using Eq. (6.9), repeating this M times, once for each discrete value of the selected equilibrium concentration. Fixed concentrations were rastered in steps of Δc. Once again, a unique solution defines a tie line between coexisting phases, say L and α. If no solutions exist, we are in single phase regions where no tie lines exist.

Appendix C

Coarse-Graining

This appendix discusses the coarse-graining methods we have applied throughout this thesis. We begin with the approximation made when developing our multi-component XPFC energy and end with a presentation of the 12-amplitude coarse-grained free energy from Chapter 7.

C.1 Long Wavelength Limit

In Section 4.3, we reduced the free energy in Eq. (4.7) into a simplified multi-component XPFC energy functional. In the process of doing this, we simplified terms by considering the long wavelength limit where the concentration varies much more slowly than the density field. This section details the steps of how some terms of Eq. (4.7) can be simplified to derive the simplified free energy functional in Eq. (4.9).

C.1.1 Terms Coupling Product of c_i and c_j with C_2^{ij}

We begin first with terms involving a coupling of two concentration fields with a correlation function. As a concrete example, consider the term

$$\mathcal{G} = -\frac{1}{2} \sum_{i,j}^{N} \int d\mathbf{r}\, c_i(\mathbf{r}) \int d\mathbf{r}'\, C_2^{ij}(|\mathbf{r} - \mathbf{r}'|) c_j(\mathbf{r}'), \tag{C.1}$$

in Eq. (4.7), where we have used the more explicit notation for clarity. (The other terms follow analogously.) To proceed, we rewrite the correlation function in a Fourier series of the form,

$$C_2^{ij}(|\mathbf{r} - \mathbf{r}'|) = \int d\mathbf{k}\, \hat{C}_2^{ij}(|\mathbf{k}|) e^{i\mathbf{k}\cdot\mathbf{r}} e^{-i\mathbf{k}\cdot\mathbf{r}'}. \tag{C.2}$$

Substituting Eq. (C.2) into Eq. (C.1) yields,

$$\tilde{\mathcal{G}} = -\frac{1}{2} \sum_{i,j}^{N} \int d\mathbf{r}\, c_i(\mathbf{r}) \int d\mathbf{k}\, \hat{C}_2^{ij}(|\mathbf{k}|) \hat{c}_j(\mathbf{k}) e^{i\mathbf{k}\cdot\mathbf{r}}, \tag{C.3}$$

where we define

$$\hat{c}_j(\mathbf{k}) \equiv \int d\mathbf{r}'\, c_j(\mathbf{r}') e^{-i\mathbf{k}\cdot\mathbf{r}'}. \tag{C.4}$$

Considering, without loss of generality, the long wavelength limit, we take a Taylor series expansion of the correlation function in powers of $\mathbf{k}^2$ around $\mathbf{k} = 0^*$. This results in,

$$\tilde{\mathcal{G}} = -\frac{1}{2} \sum_{i,j}^{N} \int d\mathbf{r}\, c_i(\mathbf{r}) \int d\mathbf{k} \sum_{l=0}^{\infty} \frac{1}{l!} (\mathbf{k}^2)^l \left. \frac{\partial^l \hat{C}_2^{ij}}{\partial (\mathbf{k}^2)^l} \right|_{\mathbf{k}=0} \hat{c}_j(\mathbf{k}) e^{i\mathbf{k}\cdot\mathbf{r}}. \tag{C.5}$$

We note that to invoke the long wavelength limit, we could have also Taylor expanded the concentration, $c_j(\mathbf{r}')$, at $\mathbf{r}' = \mathbf{r}$ as is done in Refs. [60, 61, 62] or employed the multi-scale expansion used in Refs. [89, 67]. All these methods, though different and require different mathematical treatments, are found to be equivalent. Retaining, to lowest order, terms up to order $l = 1$, we have

$$\tilde{\mathcal{G}} = -\frac{1}{2} \sum_{i,j}^{N} \int d\mathbf{r}\, c_i(\mathbf{r}) \int d\mathbf{k}\, \hat{C}_2^{ij}(|\mathbf{k}|) \Big|_{\mathbf{k}=0} \hat{c}_j(\mathbf{k}) e^{i\mathbf{k}\cdot\mathbf{r}}$$

$$-\frac{1}{2} \sum_{i,j}^{N} \int d\mathbf{r}\, c_i(\mathbf{r}) \int d\mathbf{k}\, \mathbf{k}^2 \left. \frac{\partial \hat{C}_2^{ij}}{\partial (\mathbf{k}^2)} \right|_{\mathbf{k}=0} \hat{c}_j(\mathbf{k}) e^{i\mathbf{k}\cdot\mathbf{r}}. \tag{C.6}$$

Using the definition of the inverse Fourier transform, we recast Eq. (C.6) as

$$\tilde{\mathcal{G}} = -\frac{1}{2} \sum_{ij}^{N} \gamma_{ij} \int d\mathbf{r}\, c_i(\mathbf{r})\, c_j(\mathbf{r}) - \frac{1}{2} \sum_{i,j}^{N} \kappa_{ij} \int d\mathbf{r}\, c_i(\mathbf{r}) \left(-\nabla^2\right) c_j(\mathbf{r}), \tag{C.7}$$

where we have used the following definitions,

$$\gamma_{ij} \equiv \hat{C}_2^{ij}(|\mathbf{k}|) \Big|_{\mathbf{k}=0} \tag{C.8}$$

and

$$\kappa_{ij} \equiv \left. \frac{\partial \hat{C}_2^{ij}}{\partial (\mathbf{k}^2)} \right|_{\mathbf{k}=0}. \tag{C.9}$$

It is thus clear that the first term in Eq. (C.7) will contribute terms that renormalize the coefficient of the c_i^2 terms in the entropy of mixing, if Eq. (4.8) were expanded about $c_i = c_i^\ell$. In this work, the γ_{ij} terms are neglected, and their role is subsumed in an effective manner, for convenience, into the prefactor ω in Eq. (4.9). The second term in Eq. (C.7) can be recast into gradient energy terms, which when the model is reduced to systems described by solute compositions become analogous to those used in Cahn-Hilliard or Ginzburg-Landau theories. To do so, we perform integration by parts, yielding,

$$\tilde{\mathcal{G}} = -\frac{1}{2} \sum_{i,j}^{N} \gamma_{ij} \int d\mathbf{r}\, c_i(\mathbf{r})\, c_j(\mathbf{r}) - \frac{1}{2} \sum_{i,j}^{N} \kappa_{ij} \int d\mathbf{r}\, \nabla c_i(\mathbf{r}) \cdot \nabla c_j(\mathbf{r}). \tag{C.10}$$

In what we presented in this thesis, we neglected cross gradient terms in composition. We note that such cross terms can become important when studying certain phenomena and/or when higher-order alloying interactions are considered. Note the negative sign of the gradient term are produced as expected, since formally $\kappa_{ij} > 0$, when considering a system described generally with all species compositions. When the system is described in terms of solute concentrations, Cahn-Hilliard like gradient terms are recovered. As an example, consider the simplified binary, Chapter 5, and ternary,

---

*This should hold even when $\hat{C}_2$ is not expanded in even powers of $\mathbf{k}^2$

Chapter 6, models described in the text. The binary model is described by compositions c_A and c_B. Defining the solute composition to be $c \equiv c_B$, we then use mass conservation to recast the matrix component A, as $c_A = 1 - c$. The gradient terms then follow,

$$\tilde{\mathcal{G}}_{CH}^{bin} = -\frac{1}{2} \int d\mathbf{r} \left(\kappa_{AA}|\nabla c|^2 - \kappa_{AB}|\nabla c|^2 - \kappa_{BA}|\nabla c|^2 + \kappa_{BB}|\nabla c|^2 \right)$$
$$= \frac{1}{2} \int d\mathbf{r}\, \kappa |\nabla c|^2 \tag{C.11}$$

where

$$\kappa = -\kappa_{AA} - \kappa_{BB} + \kappa_{AB} + \kappa_{BA}. \tag{C.12}$$

We see that the Cahn-Hilliard gradient term is recovered for the binary system, with $\kappa > 0$.

The ternary system is defined by compositions c_A, c_B and c_C. Defining the solute compositions to be c_A and c_B, mass conservation permits us to write the composition of the solvent species as $c_C = 1 - c_A - c_B$. Introducing these into the gradient terms for a ternary system, while ignoring cross gradients, we have,

$$\tilde{\mathcal{G}}_{CH}^{tern} = -\frac{1}{2} \int d\mathbf{r} \left(\kappa_{AA}|\nabla c_A|^2 - \kappa_{AC}|\nabla c_A|^2 - \kappa_{CA}|\nabla c_A|^2 \right)$$
$$- \frac{1}{2} \int d\mathbf{r} \left(\kappa_{BB}|\nabla c_B|^2 - \kappa_{BC}|\nabla c_B|^2 - \kappa_{CB}|\nabla c_B|^2 \right)$$
$$= \frac{1}{2} \int d\mathbf{r} \left(\kappa_A |\nabla c_A|^2 + \kappa_B |\nabla c_B|^2 \right) \tag{C.13}$$

where

$$\kappa_A = -\kappa_{AA} + \kappa_{AC} + \kappa_{CA}$$
$$\kappa_B = -\kappa_{BB} + \kappa_{BC} + \kappa_{CB}. \tag{C.14}$$

Equation (C.13) yields Cahn-Hilliard like gradients for ternary alloys with $\kappa_A > 0$ and $\kappa_B > 0$.

C.1.2   Correlation Kernels Containing Linear Terms in n

To demonstrate the long wavelength limit of terms linear in density in Eq. (4.7), we consider, as an example, the term

$$\mathcal{H} = -\frac{1}{2} \sum_{i,j}^{N} \int d\mathbf{r}\, c_i^\ell c_j(\mathbf{r}) \int d\mathbf{r}'\, C_2^{ij}(|\mathbf{r} - \mathbf{r}'|) n(\mathbf{r}'). \tag{C.15}$$

Substituting the Fourier series expansion of the correlation function, Taylor expanding the correlation as in Eq. (C.5) (retaining the lowest order term), and taking the inverse Fourier transform yields,

$$\tilde{\mathcal{H}} = -\frac{1}{2} \sum_{i,j}^{N} \gamma_{ij} \int d\mathbf{r}\, c_i^\ell c_j(\mathbf{r}) n(\mathbf{r}) - \frac{1}{2} \sum_{i,j}^{N} \kappa_{ij} \int d\mathbf{r}\, c_i^\ell c_j(\mathbf{r}) \left(-\nabla^2\right) n(\mathbf{r}), \tag{C.16}$$

where γ_{ij} and κ_{ij} are defined by Eqs. (C.8) and (C.9), respectively.

The density, $n(\mathbf{r})$, in Eq. (C.16) is rapidly varying. Its leading order representation is defined by

a single-mode approximation of the form

$$n(\mathbf{r}) = \sum_m A_m(\mathbf{r}) \, e^{i\mathbf{q}_m \cdot \mathbf{r}}, \tag{C.17}$$

where $\mathbf{q}_m$ are the reciprocal lattice vectors and $A_m(\mathbf{r})$ are slowly varying amplitudes corresponding to each reciprocal lattice vector, m. Substituting Eq. (C.17) into Eq. (C.16) gives

$$\tilde{\mathcal{H}} = -\frac{1}{2} \sum_{i,j}^N \gamma_{i,j} \sum_m \int d\mathbf{r} \, c_i^\ell \, c_j(\mathbf{r}) A_m(\mathbf{r}) \, e^{i\mathbf{q}_m \cdot \mathbf{r}}$$
$$+ \frac{1}{2} \sum_{i,j}^N \kappa_{i,j} \sum_m \int d\mathbf{r} \, c_i^\ell c_j(\mathbf{r}) \nabla^2 \left(A_m(\mathbf{r}) \, e^{i\mathbf{q}_m \cdot \mathbf{r}} \right). \tag{C.18}$$

Expanding the Laplacian in Eq. (C.18) gives,

$$\tilde{\mathcal{H}} = -\frac{1}{2} \sum_{i,j}^N \gamma_{i,j} \sum_m \int d\mathbf{r} \, c_i^\ell \, c_j(\mathbf{r}) A_m(\mathbf{r}) \, e^{i\mathbf{q}_m \cdot \mathbf{r}}$$
$$+ \frac{1}{2} \sum_{i,j}^N \kappa_{i,j} \sum_m \int d\mathbf{r} \, c_i^\ell c_j(\mathbf{r}) \, e^{i\mathbf{q}_m \cdot \mathbf{r}} \mathcal{L}_m A_m(\mathbf{r}), \tag{C.19}$$

where $\mathcal{L}_m \equiv \nabla^2 + 2i\mathbf{q}_m \cdot \nabla - \mathbf{q}_m^2$ is a covariant operator that assures rotational invariance of the free energy in the long wavelength limit. It is noted that each term in Eq. (C.19) only contains one rapidly oscillating variable, i.e., $e^{i\mathbf{q}_m \cdot \mathbf{r}}$. If we apply the so-called "quick and dirty" [111] analogue of the volume averaging method employed in Refs. [61, 62] (which amounts to decoupling slowly varying fields inside integrals from rapidly varying phase factors, thus making the integrals effectively vanish when integrated over one unit), we obtain $\tilde{\mathcal{H}} \approx 0$.

It is straightforward to show that all other terms in Eq. (4.7) that are linear in n, such as,

$$\mathcal{H} = -\frac{1}{2} \sum_{i,j}^N \int d\mathbf{r} \, n(\mathbf{r}) c_i(\mathbf{r}) \int d\mathbf{r}' \, C_2^{ij}(|\mathbf{r} - \mathbf{r}'|) c_j(\mathbf{r}'), \tag{C.20}$$

similarly vanish upon coarse graining. It should also be evident from the above considerations that if Eq. (C.15) contained an $n(\mathbf{r}) \cdots n(\mathbf{r}')$ combination, then Eq. (C.19) would contain terms with phase factors of different combinations of sums of two reciprocal lattice vectors. Some of these two-vector combinations would add up to zero causing their corresponding terms to survive upon integration.

C.2   Volume-Averaging

Equation (C.19) and similar equations, can more formally be analyzed using a volume averaging convolution operator [61], defined by

$$\langle f(\mathbf{r}) \rangle_V \equiv \int_{-\infty}^{\infty} d\mathbf{r}' f(\mathbf{r}') \xi_V(\mathbf{r} - \mathbf{r}'), \tag{C.21}$$

where $f(\mathbf{r}')$ is the function being course grained and V is the coarse graining volume. The function ξ_V in the integrand of Eq. (C.21) is a smoothing function that is normalized to unity, i.e.,

$$\int_{-\infty}^{\infty} d\mathbf{r}\, \xi_V(\mathbf{r} - \mathbf{r}') \equiv 1. \tag{C.22}$$

A convenient form of ξ_V is given by

$$\xi_V(\mathbf{r} - \mathbf{r}') = \frac{1}{\sqrt{\pi}V}\, e^{\frac{(\mathbf{r} - \mathbf{r}')^2}{V^2}}. \tag{C.23}$$

In the long wavelength limit, $L_{slow} \gg L \gg a$ where $L \sim V^{1/d}$, in d-dimensions, while L_{slow} is the length scale of variation of slowly varying fields, such as the concentration field. This condition implies that the function $\xi_V(\mathbf{r})$ varies on dimensions much larger than the lattice constant $a = 2\pi/|\mathbf{q}_m|$ but much less then the length scale of variation of the concentration, $c_i(\mathbf{r})$. Equation (C.21) defines a noninvertible limiting procedure that can be used to average a function over some volume.

It is instructive to apply the volume averaging procedure to the first term in Eq. (C.19). For convenience we define $\phi(\mathbf{r}) \equiv c_i^\ell c_j(\mathbf{r}) A_m(\mathbf{r})$. It is noted that $\phi(\mathbf{r})$ varies on scales much larger than the lattice constant since it is comprised of slowly varying functions. Using the definition of $\phi(\mathbf{r})$, the first integral of Eq. (C.19) can be written as

$$\tilde{\mathcal{H}}_V = -\frac{1}{2}\sum_{i,j}^{N} \gamma_{i,j} \sum_m \int d\mathbf{r}' \left(\int d\mathbf{r}\, \xi_V(\mathbf{r} - \mathbf{r}') \right) \phi(\mathbf{r}') e^{\mathbf{i}\mathbf{q}_m \cdot \mathbf{r}'}$$

$$= -\frac{1}{2}\sum_{i,j}^{N} \gamma_{i,j} \sum_m \int d\mathbf{r} \left(\int d\mathbf{r}'\, \xi_V(\mathbf{r} - \mathbf{r}') \phi(\mathbf{r}')\, e^{\mathbf{i}\mathbf{q}_m \cdot \mathbf{r}'} \right), \tag{C.24}$$

Since $\phi(\mathbf{r}')$ varies more slowly than the scale of variation of ξ_V and the phase factor $e^{\mathbf{i}\mathbf{q}_m \cdot \mathbf{r}'}$, it is reasonable to expand it in a Taylor series about $\mathbf{r}' = \mathbf{r}$. Substituting $\phi(\mathbf{r}') = \phi(\mathbf{r}) + \nabla\phi(\mathbf{r}) \cdot (\mathbf{r} - \mathbf{r}')$ into the above expression leads to

$$\tilde{\mathcal{H}}_V = -\frac{1}{2}\sum_{i,j}^{N} \gamma_{i,j} \sum_m \int d\mathbf{r} \left(\phi(\mathbf{r}) \int d\mathbf{r}'\, \xi_V(\mathbf{r} - \mathbf{r}')\, e^{\mathbf{i}\mathbf{q}_m \cdot \mathbf{r}'} \right.$$

$$\left. + \nabla\phi(\mathbf{r}) \int d\mathbf{r}'\, \xi_V(\mathbf{r} - \mathbf{r}') \cdot (\mathbf{r} - \mathbf{r}') e^{\mathbf{i}\mathbf{q}_m \cdot \mathbf{r}'} + \cdots \right). \tag{C.25}$$

The noninvertible procedure was introduced in the second line of Eq. (C.24). In the long wavelength limit, when $|\mathbf{q}_m| L \to \infty$, both integrals in Eq. (C.25) vanish as $\sim (|\mathbf{q}_m L|)^{-1}$, making $\tilde{\mathcal{H}}_V$ similarly vanish. To demonstrate this, we take the first term of Eq. (C.25) and solve it in Fourier space. We have

$$\tilde{\mathcal{H}}_V^1 = \phi(\mathbf{r}) \int d\mathbf{r}' \left[\int d\mathbf{k}\, \hat{\xi}_V(\mathbf{k})\, e^{\mathbf{i}\mathbf{k} \cdot \mathbf{r}} e^{-\mathbf{i}\mathbf{k} \cdot \mathbf{r}'} \right] e^{\mathbf{i}\mathbf{q}_m \cdot \mathbf{r}'}$$

$$= \phi(\mathbf{r}) \int d\mathbf{k}\, \hat{\xi}_V(\mathbf{k})\, e^{\mathbf{i}\mathbf{k} \cdot \mathbf{r}} \delta(\mathbf{k} - \mathbf{q}_m)$$

$$= \phi(\mathbf{r}) \hat{\xi}_V(\mathbf{q}_m)$$

$$\approx 0 \tag{C.26}$$

where δ is the delta function, $\hat{\xi}_V$ is the volume averaging function in Fourier space, which is a Gaussian kernel peaked at $\mathbf{k} = 0$ and rapidly decaying away from $\mathbf{k} = 0$.

C.3   Amplitude Equations for 12 Vector Density Expansion

In section 7.2.1, where we considered a density mode expansion for our coarse-graining procedure, we arrived at two expansions. While in the text, we opted to go with the simpler of the expansions, it was not rigorously motivated from any physical arguments or considerations, rather for convenience. In this appendix, we present, for completeness, the coarse-grained free energy functional associated with the density mode expansion containing 12 complex amplitudes. Before proceeding, we recall the density expansion, which takes the form,

$$n(\mathbf{r}) = n_o(\mathbf{r}) + \sum_j^6 A_j(\mathbf{r})e^{i\mathbf{k}_j \cdot \mathbf{r}} + \sum_m^6 B_m(\mathbf{r})e^{i\mathbf{q}_m \cdot \mathbf{r}} + c.c., \tag{C.27}$$

with the reciprocal lattice vectors defined in the text. The derivation is motivated and follows from the same arguments and approximations that lead us to the free energy functional of the simpler 6 complex amplitude energy of Eq. (7.16). The free energy functional of the 12 complex amplitude expansion reads,

$$\begin{aligned}
F_{12}^{cg} = \int d\mathbf{r} \Bigg\{ &\frac{n_o^2}{2} - \eta \frac{n_o^3}{6} + \chi \frac{n_o^4}{12} + \left(1 - \eta\, n_o + \chi\, n_o^2\right) \left(\sum_j^6 |A_j|^2 + \sum_m^6 |B_m|^2 \right) \\
&- (\eta - 2\chi n_o)\Big[A_1 A_2 A_3 + A_4 A_5 A_6 + B_1 B_2 B_3 + A_2 A_5^* B_5 + A_4 A_1^* B_4 \\
&+ A_3 A_6 B_3^* + A_3 A_6^* B_6 + A_2 A_5 B_2^* + A_1 A_4 B_1^* + B_5 B_6 B_4^* + c.c.\Big] \\
&+ \frac{\chi}{2}\left[\sum_j^6 A_j^2 (A_j^*)^2 + \sum_m^6 B_m^2 (B_m^*)^2 \right] \\
&+ 2\chi \left[\sum_j^6 \sum_{m>j}^6 |A_j|^2 |A_m|^2 + \sum_j^6 \sum_m^6 |A_j|^2 |B_m|^2 + \sum_j^6 \sum_{m>j}^6 |B_j|^2 |B_m|^2 \right] \\
&+ \chi\Big[A_1^2 B_1^* B_4^* + A_2^2 B_5 B_2^* + A_3^2 B_6 B_3^* + A_4^2 B_4 B_1^* + A_5^2 B_2^* B_5^* + A_6^2 B_3^* B_6^* + c.c.\Big] \\
&+ 2\chi\Big[A_2 A_3 A_4 B_4 + A_2 A_4 A_6 B_5 + A_3 A_4 A_5 B_6 + A_1 A_2 A_6 B_6^* + A_1 A_3 A_5 B_5^* + A_1 A_5 A_6 B_4^* \\
&+ A_1 A_3 A_5^* B_2 + A_1 A_2 A_6^* B_3 + A_2 A_3 A_4^* B_1 + A_4 A_5 A_3^* B_3 + A_4 A_6 A_2^* B_2 + A_5 A_6 A_1^* B_1 \\
&+ A_1 A_4 B_2 B_3 + A_2 A_5 B_1 B_3 + A_3 A_6 B_1 B_2 + A_4 A_1^* B_5 B_6 + A_3 A_6^* B_4 B_5^* + A_5 A_2^* B_6 B_4^* + c.c.\Big] \\
&- \frac{n_o}{2}\left[\hat{\xi}_V(\mathbf{k}) \hat{C}_2(|\mathbf{k}|) \hat{n}_o(\mathbf{k}) \right]_{\mathbf{r}} - \frac{1}{2}\sum_j^6 A_j^* \left[\hat{C}_2(|\mathbf{k}+\mathbf{k}_j|) \hat{A}_j(\mathbf{k}) \right]_{\mathbf{r}} - \frac{1}{2}\sum_j^6 A_j \left[\hat{C}_2(|\mathbf{k}-\mathbf{k}_j|) \hat{A}_j(-\mathbf{k}) \right]_{\mathbf{r}} \\
&- \frac{1}{2}\sum_m^6 B_m^* \left[\hat{C}_2(|\mathbf{k}+\mathbf{q}_m|) \hat{B}_m(\mathbf{k}) \right]_{\mathbf{r}} - \frac{1}{2}\sum_m^6 B_m \left[\hat{C}_2(|\mathbf{k}-\mathbf{q}_m|) \hat{B}_m(-\mathbf{k}) \right]_{\mathbf{r}} \Bigg\}. \tag{C.28}
\end{aligned}$$

C.4   Amplitude Equations for a Binary Alloy

The Fourier method we applied to generate the amplitude model above and in Chapter 7 can be readily extended to alloys as well. In this subsection, we present such an extension to a completely symmetric binary alloy, similar to that of the standard alloy model of Elder *et. al*, exhibiting triangle-triangle crystal structures for each component. For a binary alloy, we refer to the simplified XPFC binary free energy functional of Section 5.2, where each component has as input its own respective

correlation function, i.e., $\hat{C}_2^{AA}$ and $\hat{C}_2^{BB}$, respectively, in the effective correlation function. The free energy reads,

$$\mathcal{F}^{\text{bin}} = \int d\mathbf{r} \left\{ \frac{n^2}{2} - \eta\frac{n^3}{6} + \chi\frac{n^4}{12} + (n+1)\omega F_{\text{mix}}^{\text{bin}}(c) - \frac{1}{2}n \int d\mathbf{r}' C_{\text{eff}}^{\text{bin}}(|\mathbf{r} - \mathbf{r}'|)n' + \kappa|\nabla c|^2 \right\}$$

(C.29)

where,

$$C_{\text{eff}}^{\text{bin}}(|\mathbf{r} - \mathbf{r}'|) = X_A(c)C_2^{AA}(|\mathbf{r} - \mathbf{r}'|) + X_B(c)C_2^{BB}(|\mathbf{r} - \mathbf{r}'|).$$

(C.30)

The density expansion, given the symmetric nature of the binary alloy, can be written simply as

$$n(\mathbf{r}) = n_o(\mathbf{r}) + \sum_{j}^{3} A_j(\mathbf{r})e^{i\mathbf{k}_j \cdot \mathbf{r}} + c.c.,$$

(C.31)

where the reciprocal lattice vectors for a triangular lattice is schematically represented in Fig. C.1. Following the derivation and approximations that lead to the above amplitude free energy and the
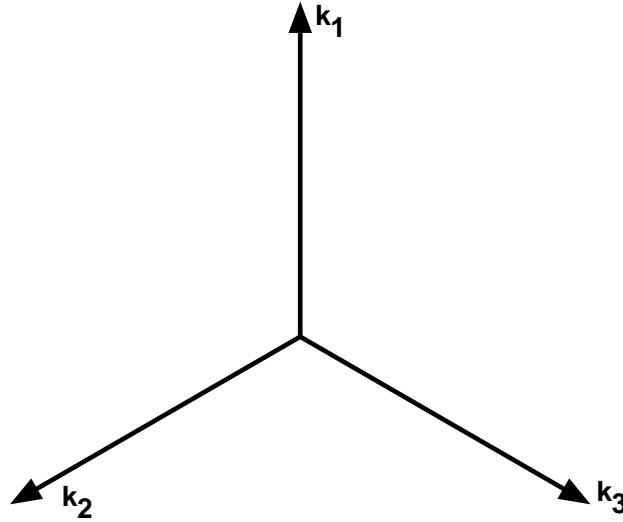

Figure C.1: Schematic representation of the reciprocal set of basis vectors for a triangular lattice. The vectors, $\mathbf{k}_1, \mathbf{k}_2, \mathbf{k}_3$, form a resonant set.

coarse-grained free energy in the text, Eq. (7.16), an amplitude model for a symmetric binary model exhibiting triangle-triangle symmetry has the following free energy functional,

$$F_{\text{bin}}^{cg} = \int d\mathbf{r} \left\{ \frac{n_o^2}{2} - \eta\frac{n_o^3}{3} + \chi\frac{n_o^4}{12} + \left(1 - \eta\, n_o + \chi\, n_o^2\right) \sum_{j}^{3} |A_j|^2 \right.$$

(C.32)

$$- (\eta - 2\chi n_o)\left[A_1 A_2 A_3 + c.c. \right] + \frac{\chi}{2}\sum_{j}^{3} A_j^2 (A_j^*)^2 + 2\chi \sum_{j}^{3} \sum_{m>j}^{3} |A_j|^2 |A_m|^2$$

$$\left. + \omega F_{\text{mix}}^{\text{bin}}(c) + \kappa|\nabla c|^2 - \frac{n_o}{2}\left(X_A(c)\left[\hat{\xi}_V(\mathbf{k})\hat{C}_2^{AA}(|\mathbf{k}|)\hat{n}_o(\mathbf{k}) \right]_{\mathbf{r}} + X_B(c)\left[\hat{\xi}_V(\mathbf{k})\hat{C}_2^{BB}(|\mathbf{k}|)\hat{n}_o(\mathbf{k}) \right]_{\mathbf{r}} \right) \right.$$

$$- \frac{1}{2} \sum_j^3 A_j^* \left(X_A(c) \left[\hat{C}_2^{AA}(|\mathbf{k} + \mathbf{k}_j|) \hat{A}_j(\mathbf{k}) \right]_\mathbf{r} + X_B(c) \left[\hat{C}_2^{BB}(|\mathbf{k} + \mathbf{k}_j|) \hat{A}_j(\mathbf{k}) \right]_\mathbf{r} \right)$$

$$- \frac{1}{2} \sum_j^3 A_j \left(X_A(c) \left[\hat{C}_2^{AA}(|\mathbf{k} - \mathbf{k}_j|) \hat{A}_j(-\mathbf{k}) \right]_\mathbf{r} + X_B(c) \left[\hat{C}_2^{BB}(|\mathbf{k} - \mathbf{k}_j|) \hat{A}_j(-\mathbf{k}) \right]_\mathbf{r} \right) \Bigg\}.$$

Bibliography

[1] R. A. Enrique and P. Bellon. *Phys. Rev. Lett.*, 84:2885, 2000.

[2] Nikolas Provatas and Ken Elder. *Phase-Field Methods in Materials Science and Engineering*. Wiley-VCH Verlag GmbH & Co. KGaA, 2010.

[3] V.L. Ginzburg and L.D. Landau. *Zh. Eksp. Teor. Fiz.*, 20:1064, 1950.

[4] J. W. Cahn and J. E. Hilliard. *J. Chem. Phys.*, 28:258, 1958.

[5] J. W. Cahn and J. E. Hilliard. *J. Chem. Phys.*, 31:688, 1959.

[6] J. A. Warren, R. Kobayashi, and W. C. Carter. *J. Cryst. Growth*, 211:18, 2000.

[7] J. A. Warren, R. Kobayashi, A. E. Lobkovsky, and W. C. Carter. *Acta Materialia*, 51:6035, 2003.

[8] L. Gránásy, T. Pusztai, T. Börzsönyi, J. A. Warren, B. Kvamme, and P. F. James. *Phys. Chem. Glasses*, 45:107, 2004.

[9] B. Bottger and I. Steinbach. *Acta Materialia*, 54:2697, 2006.

[10] I. Steinbach. *Modelling Simul. Mater. Sci. Eng.*, 17:073001, 2009.

[11] A. Choudhury and B. Nestler. *Phys. Rev. E*, 85:021602, 2012.

[12] M.Haataja and F. Léonard. *Phys. Rev. B*, 69:081201, 2004.

[13] J. Z. Zhu, T. Wang, A. J. Ardell, S. H. Zhou, Z. K. Lui, and L. Q. Chen. *Acta Materialia*, 52:2837, 2004.

[14] D. Fan and L.-Q. Chen. *Acta Metallurgica*, 45:611, 1996.

[15] Y.U. Wang, Y.M. Jin, A.M. Cuitiño, and A.G. Khachaturyan. Nanoscale phase field microelasticity theory of dislocations: model and 3d simulations. *Acta Materialia*, 49(10):1847 – 1857, 2001.

[16] K. R. Elder, M. Katakowski, M. Haataja, and M. Grant. *Phys. Rev. Lett.*, 88:245701, 2002.

[17] K. R. Elder and Martin Grant. Modeling elastic and plastic deformations in nonequilibrium processing using phase field crystals. *Phys. Rev. E*, 70:051605, Nov 2004.

[18] K. R. Elder, N. Provatas, J. Berry, P. Stefanovic, and M. Grant. *Phys. Rev. B.*, 75:064107, 2007.

[19] M. Greenwood, N. Provatas, and J. Rottler. *Phys. Rev. Lett.*, 105(4):045702, 2010.

[20] Michael Greenwood, Jörg Rottler, and Nikolas Provatas. Phase-field-crystal methodology for modeling of structural transformations. *Phys. Rev. E*, 83:031601, Mar 2011.

[21] Yongmei M. Jin and Armen G. Khachaturyan. Atomic density function theory and modeling of microstructure evolution at the atomic scale. *Journal of Applied Physics*, 100(1):013519, 2006.

[22] T. V. Ramakrishnan and M. Yussouff. First-principles order-parameter theory of freezing. *Phys. Rev. B*, 19:2775–2794, Mar 1979.

[23] A. D. J. Haymet and David W. Oxtoby. A molecular theory for the solid–liquid interface. *The Journal of Chemical Physics*, 74(4):2559–2565, 1981.

[24] David W. Oxtoby and A. D. J. Haymet. A molecular theory of the solid–liquid interface. ii. study of bcc crystal–melt interfaces. *The Journal of Chemical Physics*, 76(12):6262–6272, 1982.

[25] A. Karma. *Phys. Rev. Lett*, 87:115701, 2001.

[26] B. Echebarria, R. Folch, A. Karma, and M. Plapp. *Phys. Rev. E.*, 70:061604–1, 2004.

[27] C. Tong, M. Greenwood, and N. Provatas. *Phys. Rev. E*, 77:1, 2008.

[28] J Swift and P C Hohenberg. Hydrodynamic fluctuations at the convective instability. *Phys. Rev. A*, 15:319–328, 1977.

[29] Nana Ofori-Opoku, Jeffrey J. Hoyt, and Nikolas Provatas. Phase-field-crystal model of phase and microstructural stability in driven nanocrystalline systems. *Phys. Rev. E*, 86:066706, Dec 2012.

[30] Michael Greenwood, Nana Ofori-Opoku, Jörg Rottler, and Nikolas Provatas. Modeling structural transformations in binary alloys with phase field crystals. *Phys. Rev. B*, 84:064104, 2011.

[31] Nana Ofori-Opoku, Vahid Fallah, Michael Greenwood, Shahrzad Esmaeili, and Nikolas Provatas. Multicomponent phase-field crystal model for structural transformations in metal alloys. *Phys. Rev. B*, 87:134105, 2013.

[32] V. Fallah, Jonathan Stolle, N. Ofori-Opoku, S. Esmaeili, and N. Provatas. Phase-field crystal modeling of early stage clustering and precipitation in metal alloys. *Phy. Rev. B*, 86:134112, 2012.

[33] Vahid Fallah, Nana Ofori-Opoku, Jonathan Stolle, Nikolas Provatas, and Shahrzad Esmaeili. Simulation of early-stage clustering in ternary metal alloys using the phase-field crystal method. *Acta Materialia*, 61(10):3653 – 3666, 2013.

[34] A. Karma and W.-J. Rappel. *Phys. Rev. E*, 53:R3017, 1996.

[35] Nana Ofori-Opoku and Nikolas Provatas. A quantitative multi-phase field model of polycrystalline alloy solidification. *Acta Materialia*, 58(6):2155 – 2164, 2010.

[36] A. Karma and W.-J. Rappel. *Phys. Rev. E*, 57:4323, 1998.

[37] A. Karma and W.-J. Rappel. *Phys. Rev. Lett.*, 77(19):4050–4053, 1996.

[38] A. Karma and W.-J. Rappel. *Phys. Rev. E*, 60:3614, 1999.

[39] S. M. Allen and J. W. Cahn. *Acta Metall.*, 23, 1975.

[40] S. M. Allen and J. W. Cahn. *Acta Metall.*, 24:425, 1976.

[41] S. M. Allen and J. W. Cahn. *Acta Metall.*, 27:1085, 1979.

[42] P. C. Hohenberg and B. I. Halperin. *Rev. Mod. Phys.*, 49:435, 1977.

[43] G. Caginalp. *Arch. Rat. Mech. Anal.*, 92:205, 1986.

[44] G. Caginalp and P. C. Fife. *Phys. Rev. B*, 11:7792, 1986.

[45] J. C. Ramirez, C. Beckermann, A. Karma, and H. J. Diepers. *Phys. Rev. E*, 69:051607, 2004.

[46] K. Wu and Y. Wang Y. A. Chang and. *Scripta Mater.*, 50:1145–1150, 2004.

[47] K. Sakai. *J. Crsyt. growth*, 237–239:144–148, 2002.

[48] S. G. Kim, W. T. Kim, T. Suzuki, and M. Ode. *Annu. Rev. Mater. Res.*, 261:135–159, 2004.

[49] B. Nestler, H. Garcke, and B. Stinner. *Phys. Rev. E*, 71:041609–1, 2005.

[50] S. G. Kim. *Acta Mater.*, 55:4391–4399, 2007.

[51] M. Greenwood, M. Haataja, and N. Provatas. *Phys. Rev. Lett.*, 93:246101, 2004.

[52] N. Provatas, M., B. Athreya, N. Goldenfeld, and J. Dantzig. *International Journal of Modern Physics B*, 19:4525, 2005.

[53] R. Folch and M. Plapp. *Phys. Rev. E.*, 72:011602, 2005.

[54] A Jaatinen and T Ala-Nissila. Extended phase diagram of the three-dimensional phase field crystal model. *Journal of Physics: Condensed Matter*, 22(20):205402, 2010.

[55] D.A. Porter and K.E. Easterling. *Phase Transformations in Metals and Alloys, 2nd Edition*. CRC Press, 1992.

[56] Gyula I. Tóth, György Tegze, Tamás Pusztai, Gergely Tóth, and László Gránásy. Polymorphism, crystal nucleation and growth in the phase-field crystal model in 2d and 3d. *Journal of Physics: Condensed Matter*, 22(36):364101, 2010.

[57] G. Tegze, L. Gránásy, G. I. Tóth, F. Podmaniczky, A. Jaatinen, T. Ala-Nissila, and T. Pusztai. *Phys. Rev. Lett.*, 103(3):035702, 2009.

[58] László Gránásy, György Tegze, Gyula I. Tóth, and Tamás Pusztai. Phase-field crystal modelling of crystal nucleation, heteroepitaxy and patterning. *Philosophical Magazine*, 91(1):123–149, 2011.

[59] A. Jaatinen and T. Ala-Nissila. Eighth-order phase-field-crystal model for two-dimensional crystallization. *Phys. Rev. E*, 82:061602, Dec 2010.

[60] Kuo-An Wu and Alain Karma. Phase-field crystal modeling of equilibrium bcc-liquid interfaces. *Phys. Rev. B*, 76:184107, Nov 2007.

[61] Sami Majaniemi and Nikolas Provatas. Deriving surface-energy anisotropy for phenomenological phase-field models of solidification. *Phys. Rev. E*, 79(1):011607, 2009.

[62] Nikolas Provatas and Sami Majaniemi. Phase-field-crystal calculation of crystal-melt surface tension in binary alloys. *Phys. Rev. E*, 82(4):041601, 2010.

[63] K.R. Elder, K. Thornton, and J.J. Hoyt. The kirkendall effect in the phase field crystal model. *Philosophical Magazine*, 91(1):151–164, 2011.

[64] Jesper Mellenthin, Alain Karma, and Mathis Plapp. Phase-field crystal study of grain-boundary premelting. *Phys. Rev. B*, 78(18):184110, 2008.

[65] Joel Berry, K. R. Elder, and Martin Grant. Melting at dislocations and grain boundaries: A phase field crystal study. *Phys. Rev. B*, 77(22):224114, 2008.

[66] J. Berry, M. Grant, and K. R. Elder. *Phys. Rev. E*, 73:031609, 2006.

[67] Zhi-Feng Huang, K. R. Elder, and Nikolas Provatas. Phase-field-crystal dynamics for binary systems: Derivation from dynamical density functional theory, amplitude equation formalism, and applications to alloy heterostructures. *Phys. Rev. E*, 82:021605, Aug 2010.

[68] Georges Martin and Pascal Bellon. Driven alloys. *Solid State Physics*, 50(6):189 – 331, 1997.

[69] K.C Russell. *Progress in Materials Science*, 28(3-4):229 – 434, 1984.

[70] Gary S. Was. *Progress in Surface Science*, 32(3-4):211 – 332, 1989.

[71] R. Cauvin and G. Martin. Solid solutions under irradiation. i. a model for radiation-induced metastability. *Phys. Rev. B*, 23(7):3322–3332, 1981.

[72] R. Cauvin and G. Martin. Solid solutions under irradiation. ii. radiation-induced precipitation in alzn undersaturated solid solutions. *Phys. Rev. B*, 23(7):3333–3348, 1981.

[73] R. Cauvin and G. Martin. Solid solutions under irradiation. iii. further comments on the computed solubility limit. *Phys. Rev. B*, 25(5):3385–3388, 1982.

[74] F. Soisson, P. Bellon, and G. Martin. Two-phase dynamical equilibria driven by irradiation in ordered alloys. *Phys. Rev. B*, 46(18):11332–11345, 1992.

[75] S. M. Murphy. Spatial instability in dislocation structure under irradiation. *Europhys. Lett.*, 3:1267–1272, 1987.

[76] Y. Limoge and A. Barbu. Amorphization mechanism in metallic crystalline solids under irradiation. *Phys. Rev. B*, 30(4):2212–2215, 1984.

[77] X M.-Bai, A. F. Voter, R. G. Hoagland, M. Nastasi, and B. P. Uberuaga. *Science*, 327:1631, 2010.

[78] M. Rose, G. Gorzawski, G. Miehe, A. G. Balogh, and H. Hahn. Phase stability of nanostructured materials under heavy ion irradiation. *Nanostructured Materials*, 6(5-8):731 – 734, 1995.

[79] M. Rose, A. G. Balogh, and H. Hahn. *Nucl. Instrum. Methods Phys. Res. Sect. B*, 119:127–128, 1997.

[80] Misra A. Hattar K. Hochbauer T. and R. G. Hoagland. Influence of interfaces on the storage of ion-implanted he in multilayered metallic composites. *J. Appl. Phys. Rev.*, 98(12):123516, 2005.

[81] M. J. Demkowicz, R. G. Hoagland, and J. P. Hirth. Interface structure and radiation damage resistance in cu-nb multilayer nanocomposites. *Phys. Rev. Lett.*, 100(13):136102, 2008.

[82] M. Samaras, P. M. Derlet, H. Van Swygenhoven, and M. Victoria. *Phys. Rev. Lett.*, 88:125505, 2002.

[83] M. Samaras, P. M. Derlet, H. Van Swygenhoven, and M. Victoria. *J. Nucl. Mater.*, 47:35, 2006.

[84] R. A. Enrique and P. Bellon. *Phys. Rev. B*, 60:2885, 1999.

[85] G. Martin. Phase stability under irradiation: Ballistic effects. *Phys. Rev. B*, 30(3):1424–1436, 1984.

[86] R. A. Enrique and P. Bellon. *Phys. Rev. B*, 63:134111–1, 2000.

[87] R. A. Enrique and P. Bellon. *Phys. Rev. B*, 70:224106–1, 2004.

[88] J. J. Hoyt and M. Haataja. Continuum model of irradiation-induced spinodal decomposition in the presence of dislocations. *Phys. Rev. B*, 83:174106, May 2011.

[89] K. R. Elder, Zhi-Feng Huang, and Nikolas Provatas. Amplitude expansion of the binary phase-field-crystal model. *Phys. Rev. E*, 81:011602, Jan 2010.

[90] D. Danilov and B. Nestler. Phase-field simulations of solidification in binary and ternary systems using a finite element method. *Journal of Crystal Growth*, 275(1-2):e177 – e182, 2005.

[91] J. J. Hoyt. *Phase Transformations*. McMaster University Bookstore, 2011.

[92] G. Tegze, G. I. Tóth, and L. Gránásy. *Phys. Rev. Lett.*, 106(19):195502, 2011.

[93] Ari Adland, Alain Karma, Robert Spatschek, Dorel Buta, and Mark Asta. Phase-field-crystal study of grain boundary premelting and shearing in bcc iron. *Phys. Rev. B*, 87:024110, Jan 2013.

[94] R.K.W. Marceau, G. Sha, R. Ferragut, A. Dupasquier, and S.P. Ringer. Solute clustering in al–cu–mg alloys during the early stages of elevated temperature ageing. *Acta Materialia*, 58(15):4923 – 4939, 2010.

[95] E Ozawa and H Kimura. Excess vacancies and the nucleation of precipitates in aluminum-silicon alloys. *Acta Metall.*, 18(9):995 – 1004, 1970.

[96] S. Esmaeili, D. Vaumousse, M. W. Zandbergen, W. J. Poole, A. Cerezo, and D. J. Lloyd. A study on the early-stage decomposition in the almgsicu alloy aa6111 by electrical resistivity and three- dimensional atom probe. *Philosophical Magazine*, 87(25):3797–3816, 2007.

[97] A. Somoza, M. P. Petkov, K. G. Lynn, and A. Dupasquier. Stability of vacancies during solute clustering in al-cu-based alloys. *Phys. Rev. B*, 65:094107, Feb 2002.

[98] H Baker and H Okamoto. *Alloy Phase Diagrams*, volume 3. ASM International, Materials Park, Ohio, 1st ed edition, 1993.

[99] John W Cahn. Nucleation on dislocations. *Acta Metallurgica*, 5(3):169 – 172, 1957.

[100] Gyula I. Tóth, Tamás Pusztai, György Tegze, Gergely Tóth, and László Gránásy. Amorphous nucleation precursor in highly nonequilibrium fluids. *Phys. Rev. Lett.*, 107:175702, 2011.

[101] V. Raghavan. Al-cu-mg (aluminum-copper-magnesium). *Journal of Phase Equilibria and Diffusion*, 28(2):174–179, 2007.

[102] Y. Nagai, M. Murayama, Z. Tang, T. Nonaka, K. Hono, and M. Hasegawa. Role of vacancy–solute complex in the initial rapid age hardening in an al–cu–mg alloy. *Acta materialia*, 49(5):913–920, 2001.

[103] S. H. Babu, R. Rajaraman, G. Amarendra, R. Govindaraj, N. P. Lalla, A. Dasgupta, G. Bhalerao, and C. S. Sundar. *Philosophical Magazine*, 92(23):2848, 2012.

[104] N Provatas, N Goldenfeld, and J Dantzig. Efficient computation of dendritic microstructures using adaptive mesh refinement. *Phys. Rev. Lett.*, 80:3308–3311, 1998.

[105] N. Provatas, J. Dantzig, and N. Goldenfeld. *J. Comp. Phys.*, 148:265, 1999.

[106] Badrinarayan P. Athreya, Nigel Goldenfeld, Jonathan A. Dantzig, Michael Greenwood, and Nikolas Provatas. Adaptive mesh computation of polycrystalline pattern formation using a renormalization-group reduction of the phase-field crystal model. *Phys. Rev. E*, 76:056706, Nov 2007.

[107] Zhi-Feng Huang and K. R. Elder. Mesoscopic and microscopic modeling of island formation in strained film epitaxy. *Phys. Rev. Lett.*, 101(15):158701, 2008.

[108] Robert Spatschek and Alain Karma. Amplitude equations for polycrystalline materials with interaction between composition and stress. *Phys. Rev. B*, 81:214201, Jun 2010.

[109] R. Spatschek, A. Adland, and A. Karma. Structural short-range forces between solid-melt interfaces. *Phys. Rev. B*, 87:024109, Jan 2013.

[110] Dong-Hee Yeon, Zhi-Feng Huang, K.R. Elder, and K. Thornton. Density-amplitude formulation of the phase-field crystal model for two-phase coexistence in two and three dimensions. *Philosophical Magazine*, 90(1-4):237–263, 2010.

[111] N. Goldenfeld, B. P. Athreya, and J. A. Dantzig. *Phys. Rev. E.*, 72:020601, 2005.

[112] Nigel Goldenfeld, BadrinarayanP. Athreya, and JonathanA. Dantzig. Renormalization group approach to multiscale modelling in materials science. *Journal of Statistical Physics*, 125:1015–1023, 2006.

[113] Badrinarayan P. Athreya, Nigel Goldenfeld, and Jonathan A. Dantzig. Renormalization-group theory for the phase-field crystal equation. *Phys. Rev. E*, 74:011601, Jul 2006.

[114] M. Raj Lakshmi, H. R. Krishna-Murthy, and T. V. Ramakrishnan. Density-wave theory of dislocations in crystals. *Phys. Rev. B*, 37:1936–1949, Feb 1988.

[115] C. Kubstrup, H. Herrero, and C. Pérez-García. Fronts between hexagons and squares in a generalized swift-hohenberg equation. *Phys. Rev. E*, 54:1560–1569, Aug 1996.

[116] Gemunu H. Gunaratne, Qi Ouyang, and Harry L. Swinney. Pattern formation in the presence of symmetries. *Phys. Rev. E*, 50:2802–2820, Oct 1994.

[117] Nana Ofori-Opoku, Jonathan Stolle, and Nikolas Provatas. unpublished.

[118] W. H. Shih, Z. Q. Wang, X. C. Zeng, and D. Stroud. Ginzburg-landau theory for the solid-liquid interface of bcc elements. *Phys. Rev. A*, 35:2611–2618, Mar 1987.

[119] S. Majaniemi and M. Grant. Dissipative phenomena and acoustic phonons in isothermal crystals: A density-functional theory study. *Phys. Rev. B*, 75:054301, Feb 2007.

[120] Peter Stefanovic, Mikko Haataja, and Nikolas Provatas. Phase-field crystals with elastic interactions. *Phys. Rev. Lett.*, 96(22):225504, 2006.

[121] J.J. Hoyt, M. Asta, and A. Karma. *Phys. Rev. Lett.*, 86:5530, 2001.

[122] J.J. Hoyt, M. Asta, and A. Karma. *Mat. Sci and Eng R*, R41-6:121, 2003.

[123] Zhi-Feng Huang. Scale-coupling and interface-pinning effects in the phase-field-crystal model. *Phys. Rev. E*, 87:012401, Jan 2013.